

# Carnegie Mellon University

CARNEGIE INSTITUTE OF TECHNOLOGY

## THESIS

SUBMITTED IN PARTIAL FULFILLMENT OF THE REQUIREMENTS

FOR THE DEGREE OF Doctor of Philosophy

## TITLE

THERMAL PROPERTIES OF ORGANIC-INORGANIC MATERIALS  
SUPERSTRUCTURED AT THE NANOSCALE

PRESENTED BY **WEE-LIAT ONG**

ACCEPTED BY THE DEPARTMENT OF

**MECHANICAL ENGINEERING**

---

ADVISOR, MAJOR PROFESSOR

---

DATE

---

DEPARTMENT HEAD

---

DATE

APPROVED BY THE COLLEGE COUNCIL

---

DEAN

---

DATE

**THERMAL PROPERTIES OF ORGANIC-INORGANIC MATERIALS  
SUPERSTRUCTURED AT THE NANOSCALE**

Submitted in partial fulfillment of the requirements for  
the degree of  
Doctor of Philosophy  
in Mechanical Engineering

Wee-Liat Ong

B.Eng., Mechanical Engineering, National University of Singapore, 2002

M.Eng., Mechanical Engineering, National University of Singapore, 2004

Carnegie Mellon University  
Pittsburgh, PA

January, 2015

©

Wee-Liat Ong  

---

All Rights Reserved

2015

## **ACKNOWLEDGEMENTS**

I would like to thank the Steinbrenner Institute, ICES, and the Bushnell family for supporting my Ph.D study through the Steinbrenner Fellowship in 2011, the Northrop-Grumman Fellowship in 2012, and the Bushnell Fellowship in 2013. This work is, in addition, supported by research grants from the AFRSO, NSF, and ARMY research offices.

I would also like to extend my gratitude to my committee members, Prof Baowen Li, Prof Jonathan Malen (Co-chair), Prof Alan McGaughey (Co-chair), and Prof Allen Robinson for their valuable time and advices. Prof Jonathan Malen and Prof Alan McGaughey who are my Ph.D advisors have been very instrumental in my professional life with their timely advices and insights. Other than work-related issues, they have also been very approachable to discuss life problems and offering lessons from their past experiences. To them, I have to express my heartfelt thanks for specially picking me to work on their projects.

It has been an eye-opening journey for me during the past four and a half years. The experiences and life lessons encountered during this period of my life will forever be engraved in my memory. I would like to thank my family members especially my sisters who have encouraged me to act on my Ph.D dream though I may have better contributions if I have stayed in Singapore. To my friends both in Singapore and Pittsburgh who have faith in me and encouraged me when I was going through a rough

patch, I would not have completed this without your support. Special mentions for my support group in USA - Ankit Jain, Tat-loon Chng, Mabel Ng, and Rodney Fu's family. I have also been touched by unbelievable number of kind people during these years, friends like Hu Li, Scott and his wife Yuxin, Zoey, Bao-an and his wife Jing, Jason Larkin, Ying-ying, Lili Ehrlich, Francisco and his wife Olga, Gerard Ee, and Chonghan have either helped me in my professional or personal life. Thanks! Of course, my groupmates who are a wonderful bunch like Justin "the man", Shub, Keith, Jillian "the discoverer of the Jillian constant", and others. Thanks for entering my life and teaching me a trick or two!

To end, I would like to flaunt my appalling linguistic ability by attempting to pen an incoherent poem (Yes! Ph.D mechanical engineers can be poetic!):

When you see a beautiful butterfly dancing among the flowers,

Do you remember that it was an ugly hairy caterpillar?

No?

Why then focus on the mistakes, the hurt, and the pain of the past,

When you have evolved and grown?

Just be thankful, acknowledge the past, and let it go.

For without first being a caterpillar,

You can never be a beautiful butterfly!

# ABSTRACT

## THERMAL PROPERTIES OF ORGANIC-INORGANIC MATERIALS SUPERSTRUCTURED AT THE NANOSCALE

by

Wee-Liat Ong

Co-chairs: Jonathan A. Malen and Alan J.H. McGaughey

The thermal properties of nanocrystal arrays and large unit cell molecular crystals are studied using experimental and computational techniques. The major objective is to understand the mechanisms of thermal transport through three-dimensional organic-inorganic superstructured materials that are built from superatoms. The frequency domain thermoreflectance technique is applied to measure thermal conductivity in thin films and nanoliter sized single crystals. Molecular dynamics simulations, lattice dynamics calculations, and density functional theory calculations are employed to interpret the measurements and to explore experimentally-inaccessible nanoscale phenomena.

A superatom is a cluster of atoms that behaves as a stable or metastable unit with emergent properties distinct from its elemental atoms. Superatoms can self-assemble into three-dimensional hierarchical materials with each superatom occupying a lattice site to form a periodic solid (i.e., a superlattice). By varying geometry and composition,

the resulting solid can have tunable electrical and optical properties. This work presents the first investigation of the thermal properties of solids built from two classes of superatoms: (i) monodispersed nanocrystals that form a nanocrystal array (NCA) and (ii) inorganic-organic superatoms of precise stoichiometric composition that form a molecular crystal (LUMC).

The thermal conductivity of NCAs was measured to be between 0.1 to 0.3 W/m-K. Experiments revealed that energy transport is mediated by the density and chemistry of the organic/inorganic interfaces as well as the volume fractions of nanocrystal cores and surface ligands. The NCA thermal conductivity trends upward then plateaus with increasing temperature suggesting elastic scattering events dominate transport at the organic-inorganic interfaces. The onset temperature of the plateau is dependent on the overlap of the vibrational states in the core and ligand.

Atomistic computational analysis of the thermal transport explored experimentally inaccessible trends that provided new insights for controlling heat flow in NCAs. A decreasing interfacial thermal conductance trend for the organic-inorganic interface with increasing nanocrystal diameter was discovered. This trend can be related to the interfacial thermal conductance of a self-assembled monolayer (SAM) interface through a geometrical scaling law. Changing the atomic mass of the nanocrystal core to vary its vibrational states resulted in a non-monotonic trend in both the thermal conductivity and interfacial thermal conductance. Peaks in both properties occur at the same small atomic mass and are related to the overlap and coupling of the organic and inorganic vibrational states.

Preliminary measurements of LUMCs indicate that the thermal conductivity is

between 0.2 and 0.4 W/mK at the temperature of 300 K, comparable to that of an amorphous polymer. A slight increase in thermal conductivity is observed for the binary-species LUMCs that contain fullerene derivatives over their corresponding mono-species LUMCs composed of inorganic core superatoms. This increase may be attributed to the stronger ionic intermolecular bonds in the binary LUMCs. The presence of a larger chalcogenide element in the inorganic core superatom decreases the thermal conductivity of the LUMC. This decrease is consistent with lower frequency vibrational modes that have a lower group velocity in the crystal. The temperature dependent thermal conductivity of a mono-species CoSe LUMC has a crystalline-like behavior, unlike most low thermal conductivity materials.

Nanoscale superstructured organic-inorganic materials self-assemble from solutions and can be scalable to replace single crystal semiconductors for many technologies. Arrays of ligand-stabilized colloidal nanocrystals with size-tunable electronic structure are promising alternatives to single-crystal semiconductors in electronic, opto-electronic, and energy-related applications. The low thermal conductivity in the NCA presents a challenge for thermal management but a boon for thermoelectric waste heat scavenging. The class of large unit cell molecular crystals investigated here have low thermal conductivity and a moderate electrical conductivity, making them novel candidates for thermoelectricity.



# TABLE OF CONTENTS

<b>ACKNOWLEDGEMENTS.....</b>	<b>ii</b>
<b>ABSTRACT.....</b>	<b>iv</b>
<b>TABLE OF CONTENTS.....</b>	<b>vii</b>
<b>LIST OF TABLES.....</b>	<b>xii</b>
<b>LIST OF FIGURES.....</b>	<b>xiii</b>
<b>NOMENCLATURE.....</b>	<b>xix</b>
<b>CHAPTER 1.....</b>	<b>1</b>
<b>Superaatom-Assembled Materials .....</b>	<b>1</b>
1.1 Introduction .....	1
1.2 Nanocrystal Arrays.....	2
1.3 Large Unit Cell Molecular Crystals .....	5
1.3.1 Molecular Crystals of C <sub>60</sub> .....	6
1.3.2 Molecular Crystals of Inorganic-organic Superaatoms.....	8
1.4 Overview and Scope.....	11
<b>CHAPTER 2.....</b>	<b>13</b>
<b>Thermal Transport in Three Dimensional Nanocrystal Arrays .....</b>	<b>13</b>
2.1 Overview .....	13
2.2 Introduction .....	14
2.3 Materials and Methods .....	14

2.3.1	Nanocrystal Arrays .....	14
2.3.2	Frequency-domain thermal reflectance (FDTR) .....	17
2.3.3	Molecular Dynamics (MD) .....	19
2.3.4	Vibrational density of states calculation .....	22
2.4	Result and Discussion .....	24
2.4.1	Heat Capacity.....	24
2.4.2	Thickness-dependent Thermal Conductivity .....	25
2.4.3	Core Diameter-dependent Thermal Conductivity .....	26
2.4.4	Effective Medium Approximations.....	27
2.4.5	Temperature-dependent Thermal Conductivity and Interfacial Thermal Conductance .....	32
2.4.6	Core-ligand Chemistry-dependent Thermal Conductivity .....	35
2.5	Conclusion.....	38

## **CHAPTER 3.....40**

### **Coupling of Organic and Inorganic Vibrational States and Their Thermal Transport in**

#### **Nanocrystal Arrays..... 40**

3.1	Overview .....	40
3.2	Introduction .....	41
3.3	Methods.....	42
3.4	Result and Discussion .....	47
3.4.1	Validation of Model .....	47
3.4.2	Diameter-dependent Ligand Footprint .....	49
3.4.3	Core Diameter Series.....	51
3.4.4	Core Mass Series .....	56
3.5	Conclusion.....	60

**CHAPTER 4.....61**

**Large Unit Cell Molecular Crystals and Their Thermal Properties ..... 61**

4.1	Overview .....	61
4.2	Introduction .....	62
4.3	Methods and Materials .....	63
4.3.1	LUMCs.....	63
4.3.2	FDTR Technique.....	64
4.3.3	Heat Capacity of LUMCs .....	66
4.4	Results and Discussion.....	67
4.4.1	Heat Capacity of LUMCs .....	67
4.4.2	Room Temperature Thermal Conductivity.....	72
4.4.3	Temperature Dependent Thermal Conductivity .....	74
4.5	Conclusion.....	75

**CHAPTER 5.....76**

**Other Completed Work..... 76**

5.1	Bi <sub>1-x</sub> Sb <sub>x</sub> Alloy Nanocrystals: Colloidal Synthesis, Charge Transport and Thermoelectric Properties.....	76
5.1.1	Introduction.....	76
5.1.2	Method .....	77
5.1.2	Results and Discussion.....	81
5.2	Experimental estimates of in-plane thermal conductivity in FePt-C granular thin film heat assisted magnetic recording media using a model layered system .....	83
5.3	Compositionally matched nitrogen-doped Ge <sub>2</sub> Sb <sub>2</sub> Te <sub>5</sub> /Ge <sub>2</sub> Sb <sub>2</sub> Te <sub>5</sub> superlattice-like structures for phase change random access memory .....	84
5.3.1	Abstract .....	84

5.3.2	Introduction.....	85
5.3.3	Thermal Conductivity Measurements .....	86
5.4	Vibrational mismatch of metal leads controls thermal conductance of self-assembled monolayer junctions .....	<b>Error! Bookmark not defined.</b>
<b>CHAPTER 6 .....</b>		<b>90</b>
<b>Summary and Outlook .....</b>		<b>90</b>
6.1	Nanocrystal Arrays.....	90
6.2	Large Unit Cell Molecular Crystals .....	93
6.3	Outlook.....	94
<b>Appendix A .....</b>		<b>96</b>
I	Calculation of core volume fraction and interface density in NCA .....	96
II	Figures .....	97
III	Tables.....	98
<b>Appendix B .....</b>		<b>101</b>
I	Inter- and Intra-molecular Potentials .....	101
II	Gold Thermal Conductivity from Molecular Dynamics .....	104
III	Dodecanethiol Solid Thermal Conductivity from Molecular Dynamics .....	105
IV	Molecular Dynamics Prediction of SAM Interfacial Thermal Conductance .....	106
V	Uncertainty Analysis.....	108
<b>Appendix C.....</b>		<b>110</b>
I	Steady-state temperature rise in LUMCs .....	110
II	DFT calculation of heat capacity .....	110
<b>Appendix D .....</b>		<b>113</b>
I	Calibration .....	113

II	Error analysis.....	114
III	Software for Performing Steady State Measurements.....	114
	<b><i>References</i> .....</b>	<b>123</b>

# LIST OF TABLES

## Table

2.1	Nanocrystals and ligands used for the preparation of NCAs thin films .....	15
3.1	Simulated NCA thermal conductivity for cross-sectional area convergence for 1.6 nm diameter nanocrystals.....	47
4.1	LUMCs used in thermal conductivity measurements.....	64
4.2	Room temperature thermal conductivity of LUMCs.....	73
5.1	Pellets process history and their average grain size.....	82
A1	Fitting parameters for FDTR .....	99
A2	Characterisation of NCA film roughness using AFM .....	100
A3	Core volume fraction and interface density for PbS-Oleic acid NCAs .....	101
A4	Calculated density of NCAs .....	101
B1	Potentials and their parameters.....	103
B2	Thermal conductivity of bulk gold with different mass multiples from molecular dynamics .....	106
C1	The convergent parameters used in the DFT calculations .....	113

# LIST OF FIGURES

## Figure

1.1	Superatoms and Molecular Solids. C <sub>60</sub> , inorganic-organic clusters, and nanocrystals can assemble into molecular solids [2,4] with tailored properties. ....	2
1.2	NCA Synthesis. a, Dropcasting technique. b, NCA with long-range order [18] .....	3
1.3	Two-tier phonon system in NCA arising from two periodic lengthscales: Interatomic distance in a nanocrystal and inter-nanocrystal in the NCA.....	5
1.4	Structures of the superatoms. The ethyl groups (Et <sub>3</sub> ) on the phosphines (P) were removed to clarify the view [4]. ....	9
1.5	Structures of molecular crystals. a, Structure of Co <sub>6</sub> Se <sub>8</sub> (PEt <sub>3</sub> ) <sub>6</sub> •2C <sub>60</sub> showing the crystal packing looking along the ab plane. b, down the c axis. c, Structure of Ni <sub>9</sub> Te <sub>6</sub> (PEt <sub>3</sub> ) <sub>8</sub> •C <sub>60</sub> . Carbon, black; nickel, red; cobalt, blue; phosphorus, orange; tellurium, teal; selenium, green. The ethyl groups on the phosphines were removed to clarify the view [4] .....	10
2.1	Structure and heat capacity of NCA films. a, Schematic of a gold-coated NCA film where an intensity modulated pump laser periodically heats the sample and a probe laser senses the resultant temperature change by thermorefectance to measure thermal conductivity. The magnified view to the right depicts the NCA thin film. b, SEM cross-sectional image of a 7.5 nm diameter PbS NCA film. c, Planar TEM image of a 8 nm diameter Fe <sub>3</sub> O <sub>4</sub> NCA film showing a regular close-packed arrangement. d, Specific heat capacity data as a function of temperature for a diameter series of PbS nanoparticles coated with oleic acid ligands. e, The specific heat capacity of a NCA at 300 K can be estimated as a mass-weighted function of the specific heat capacities of the core material ( $C_{core}$ ) and the ligand ( $C_{Ligand}$ ) (i.e., $C_P = m_{core} C_{core} + m_{Ligand} C_{Ligand}$ where $m_{core}$ is the mass-fraction of the core and $m_{Ligand}$ is the mass-fraction of the ligand). The plot shows the measured and estimated values using bulk values of PbS ( $C_{core} = 0.19$ J/g-K, ref. 24) and oleic acid ( $C_{Ligand} =$	

2.043 J/g-K, ref. [60]).....	16
2.2 FDTR schematic and data. a, An intensity modulated pump laser (488 nm) is periodically modulated by an electro-optic modulator and heats the sample periodically. An unmodulated probe laser (532 nm), coincident with pump at the sample surface, senses the periodic temperature change by thermorefectance. The thermorefectance signal is monitored by a lock-in amplifier, measuring the phase lag of the temperature change relative to the heat flux as a function of frequency. b, FDTR phase lag data and fits, plotted as a function of modulation frequency for bare silicon and a NCA film on silicon. The differences in the signals indicate a high sensitivity to the NCA thermal conductivity .....	17
2.3 MD simulation model. The model used in the MD simulations simplifies a NCA into a linear chain. In this case, eight cores (red spheres) with their tethered ligands (six yellow chains on each core with two along each Cartesian direction) are shown. A typical simulated steady-state temperature profile after a heat flux is applied is plotted below. Each point represents an average temperature in one-half of a core, depicting a constant temperature profile in each core with significant temperature drops across the ligand bridges between the cores .....	19
2.4 Vibrational density of states (vDOS) of a 2.8-nm diameter Au nanocrystal and its individual constituents (Au core and a dodecanethiol ligand) predicted from lattice dynamics calculations. The blue vertical lines represent the vibrational spectrum of one ligand. The yellow region is the vDOS of the Au core, which is enclosed in the green vDOS of the nanocrystal. The vertical red line represents the thermal activation frequency ( $\frac{k_B T}{h_c}$ ) at a temperature of 300 K ( $k_B$ is the Boltzmann constant and $h_c$ is the Planck constant). .....	25
2.5 Thermal conductivity thickness series for NCAs. a, Film-thickness series for CdSe (diameter = 4.1 nm) NCA showing invariant thermal conductivity with thickness at temperatures of 10 K, 77 K, and 300 K. A similar trend is observed in the MD simulation result. b, The thermal conductivities of various NCAs at a temperature of 300 K showing invariance with thicknesses. The number in parentheses is the core diameter. The ligand groups for the different NCAs can be	



found in Table 2.1 .....	26
2.6 Effects of NCA geometry on thermal conductivity. a, Diameter series data for various NCAs have increasing thermal conductivity with core diameter regardless of core composition. The trend of the MD simulation results agrees with the experimental data. Inset shows that $k_{NCA}$ does not strongly depend on the thermal conductivity of the bulk core material. The orange dotted line here and in b is the thermal conductivity of Pb-oleate at 300 K. b, Effective medium approximations cannot explain the PbS NCA data [73,74] without the use of a finite thermal conductance at the core-ligand interface integral to HJ-ME and Minnich models. These models clarify that increased $k_{NCA}$ results from decreased interface density (from $4.37 \times 10^8 \text{ m}^2/\text{m}^3$ to $3.43 \times 10^8 \text{ m}^2/\text{m}^3$ ) and increased core volume fraction (from 0.24 to 0.43) over the diameter range 3.3 - 7.5 nm.....	27
2.7 Effects of temperature on thermal conductivity. a, Temperature series for CdSe (diameter = 4.1 nm, $\theta_{D,CdSe} = 182 \text{ K}$ ; ref. [79]), PbS (diameter = 7.5 nm, $\theta_{D,PbS} = 225 \text{ K}$ ; ref. [80]), PbSe (diameter = 7.5 nm, $\theta_{D,PbSe} = 175 \text{ K}$ ; ref. [80]), PbTe (diameter = 7.5 nm, $\theta_{D,PbTe} = 136 \text{ K}$ ; ref. [80]) and $\text{Fe}_3\text{O}_4$ (diameter = 8.0 nm, $\theta_{D,Fe_3O_4} > 350 \text{ K}$ ; ref. [81]) NCAs, and Pb-oleate ligands. The points have been slightly offset in temperature so errorbars can be resolved. $T^2$ and $T^3$ scalings are included for reference. b, Normalized temperature series for Pb-oleate ligands and PbSe and $\text{Fe}_3\text{O}_4$ NCAs (with the respect to their maximum thermal conductivity) plateau above 150 K for Pb-oleate, 200 K for PbSe and 300 K for $\text{Fe}_3\text{O}_4$ NCA. ....	33
2.8 Fitted h using HJ-ME for PbSe and $\text{Fe}_3\text{O}_4$ NCAs .....	34
2.9 Effects of NCA chemistry on thermal conductivity. a, Oleate-capped lead chalcogenide NCAs show a decrease in thermal conductivity with larger mass ratio, i.e., smaller core Debye temperature $\theta_D$ ( $\theta_D$ from ref. [80]). The MD simulation data are displaced horizontally for clarity. b, NCA thermal conductivity for different inorganic ( $\text{In}_2\text{Se}_4^{2-}$ , $\text{AsS}_3^{3-}$ , $\text{N}_2\text{H}_4$ ) and organic ligands [tetradecylphosphonic acid (TDPA) and oleic acid (OA)] on CdSe and PbS NCs. Shorter inorganic ligands increase the thermal conductivity by 50% relative to organic ligands .....	37
3.1 Building an NCA with 1.6 nm diameter cores. a, Gold core surrounded with excess ligands.	

Scale bar applies to all sub-figures. b, Ligands redistribute and attach across the core surface. c, After filtering excess ligands, nanocrystals are stacked to form an open FCC 3x2x2 unit cell. d, After relaxation, a close-packed structure forms. Different layers in the stack are distinguished by their colors. e, Using this relaxed unit cell, different NCA thicknesses can be formed by tiling. The non-equilibrium MD direct method for predicting thermal conductivity is performed on an n-layer NCA array bounded by heat source, heat sink, and fixed regions. The ligands are translucent here so that the cores are visible..... 46

3.2 Predicted thermal conductivities and corresponding experimental measurements [55] of varying the NCA thickness..... 48

3.3 Diameter-dependent footprint of dodecanethiol ligands on a gold core. The MD-predicted footprints agree well with predictions from equation 3.1 (dotted line) [102]. The  $R^2$  value of the fit is 0.86. See Appendix B Section V for discussion of error bars..... 50

3.4 EMA investigation for diameter series. a, Interfacial thermal conductance from the FCC NCA cuboid scales according to equation 3.3, where  $h_{SAM/gold}$  is the predicted SAM thermal conductance and  $c = 0.76$  nm is obtained from the footprint scaling law (Figure 3.3). The red shaded region depicts the uncertainty in the  $h_{SAM/gold}$  value (see Appendix B section V). The value of  $h_{SAM/gold}$  is plotted as a blue dotted line with its associated uncertainty (blue shaded area). Inset: Interfacial thermal conductance shows no temperature-dependence between 200 to 400 K, indicating a dominance of elastic scattering between the core and ligands. b, MD diameter series is well-described by EMA- $h$  using the interfacial thermal conductance values calculated from equation 3.3. The red shaded region marks the uncertainty range associated with the EMA- $h$  model due to the uncertainties in the inputs to equation 3.2. The EMA- $h$  trend calculated using  $h_{SAM/gold}$  underestimates the simulated diameter series by at most 10%. Note that the top axis is non-linear. The inset identifies the different inputs to the EMA- $h$  formulation, equation 3.2 ..... 54

3.5 Core mass series. a, Molecular dynamics interfacial thermal conductance values for a 4.0 nm diameter core at different gold mass multiples. b, NCA thermal conductivity from MD simulations and the EMA- $h$  model (equation 3.2). The upper and lower limits mark the range of

thermal conductivity accessible with changing mass multiple. c, Vibrational spectra of a dodecanethiol ligand (blue vertical lines) and 4 nm gold nanoparticles of different mass multiples. ....	59
4.1 LUMC crystal structures. Mono-species LUMC: $\text{Co}_6\text{Se}_8(\text{PEt}_3)_6$ structure a, top view (o-c direction) b, side view (o-b direction). Binary-species LUMC: $\text{Co}_6\text{Se}_8(\text{PEt}_3)_6 \cdot 2\text{C}_{60}$ structure c, top view (o-c direction) d, side view (o-b direction). Blue – cobalt, yellow – selenium, orange – phosphorous, gray – carbon, and white – hydrogen .....	63
4.2 FDTR lasers on a $\text{Co}_6\text{Se}_8(\text{PEt}_3)_6$ molecular crystal sample. a, Microscopic view of several crystals. The black regions are crystals with surfaces that reflect the incident light away from the incident path. The lines on the reflective crystals are the boundaries of the tilted crystal facets. b, Artistic impression of the FDTR technique on the molecular crystal .....	64
4.3 DFT vibrational spectra of superatoms. a, An isolated CoSe. b, An isolated CoTe. c, An isolated $\text{C}_{60}$ . d, A periodic FCC $\text{C}_{60}$ . The vertical red dotted line represents the thermal activation frequency ( $\frac{k_B T}{h_c}$ ) at a temperature of 300 K ( $k_B$ is the Boltzmann constant and $h_c$ is the Planck constant) .....	68
4.4 Temperature dependent heat capacity values of $\text{C}_{60}$ . a, Comparison between experimental [111], DFT isolated system prediction, and DFT periodic system predictions. b, Above temperatures of 200 K, a maximum deviation of 20% is seen. This value increases rapidly to about 60% at 100 K. c, Using the spectrum from an FCC unit cell, the maximum deviations drops to below 35% .....	70
4.5 Baseline heat capacity trends for some LUMCs. These values are calculated using equation 4.1 with inputs from the DFT-driven gamma-point vibrational spectra and scaled by their respective bulk densities .....	71
4.6 Heat capacities of a, CoSe and b, CoTe LUMCs. Some of the measured heat capacities exceed the classical Dulong Petit limit at temperatures above 200 K. ....	72
4.7 Temperature dependent thermal conductivity of CoSe LUMC .....	74

5.1	Setup for steady-state measurement. The jig with a sample sandwiched between the stainless steel top and aluminium bottom is shown in the bottom left corner. Nichrome wires on top acted as the Joule heater. Platinum thermistors were used to measure the temperatures across the jig at designated locations. The red circle, blue square, and black triangle correspond to positions of the first, second, and third thermistor whose representative readings are shown in Figure 5.2 .	78
5.2	a, Temperature profiles of the thermistors with time. After 1500s, steady state was reached as evident from the flat temperature profiles from all three thermistors. b, Measured heat flow as a percentage of heat supplied. c, Corresponding thermal conductivity of the sample .....	81
5.3	Temperature dependent thermal conductivity of Bi <sub>1-x</sub> Sb <sub>x</sub> pellets. The temperature dependent trend obtained is similar to that of a bulk Bi <sub>1-x</sub> Sb <sub>x</sub> sample [116].....	83
5.4	Thermal conductivity of the N-GST/GST samples .....	87
5.5	X-ray Diffraction spectra of N-GST-4 %, N-GST-2 %, and GST.....	88
A1	EMA models with PbS-oleic NCA series using thermal conductivity of liquid oleic acid. The thermal conductivity of liquid oleic acid is 0.23 W/m-K [76] .....	98
B1	SAM junction used for predicting the interfacial thermal conductance. A representative temperature profile and the fits are shown below.....	109
D1	Temperature-dependent thermal conductivity of Pyrex .....	115

# NOMENCLATURE

$\alpha_{NCA}$	NCA thermal diffusivity
$a_i$	Dihedral constant i
$B_{cc}$	Three-body bending energy term between atoms in the ligand
$B_{cNP}$	Three-body bending energy term between atoms in the ligand and the core
$C_{core}$	Specific heat capacities of the core material
$C_{Ligand}$	Specific heat capacities of the ligand
$C_p$	Specific heat capacity
$d$	Diameter
$diaCore$	Diameter of core
$D_e$	Force constant for Morse
$\theta_{D,M}$	Debye temperature of material M
$\frac{dT}{dx}$	Temperature gradient
$E_\theta$	Bond bending energy
$E_D$	Dihedral energy
$E_{LJ}$	Lennard-Jones energy
$E_{morse}$	Morse energy
$E_s$	Bond stretching energy
$F_{dist}$	Face-diagonal distance on a conventional FCC unit cell
$h_c$	Planck constant

$\hbar$	Planck constant divided by $2\pi$
$h$	Interfacial thermal conductance / thermal interface conductance
$h_{SAM/gold}$	Interfacial thermal conductance of SAM on gold
$k_B$	Boltzmann constant
$k_\theta$	Force constant for bond bending
$k_{NCA}$	Thermal conductivity of nanocrystal array
$k_{LUMC}$	Thermal conductivity of large unit cell molecular crystal
$k_m$	Bulk thermal conductivity of matrix phase
$k_p$	Bulk thermal conductivity of solid inclusions phase
$k_s$	Force constant for bond stretching
$L_{Al}$	Distance below the upper edge of the bottom piece
$L_{NCA}$	NCA film thickness
$L_{SS}$	Distance above the lower edge of the top piece
$M$	Mass
$m_{core}$	Mass of the core material
$m_{Ligand}$	Mass of the ligand
$\varphi$	Core volume fraction
$\vec{q}$	Heat flux
$\Phi$	Interface density
$S$	Seebeck coefficient,
$\sigma_d$	Diameter-dependent footprint
$\sigma_e$	Electrical conductivity

$\sigma_{SAM}$	Footprint of a SAM
$\tau_{NCA}$	NCA thermal time constant
$T$	Temperature
$V$	Volume
$Vol_{eff\_cell}$	Effective volume of a cell containing a core
$v_m$	Volume fraction of matrix phase
$v_p$	Volume fraction of solid inclusions phase

## Abbreviations

AFM	Atomic Force Microscope
DSC	Differential Scanning Calorimetry
DFPT	Density Functional Perturbation Theory
DFT	Density Functional Theory
DFT+D	Density Functional Theory with Dispersion Forces
EAM	Embedded-atom method
EMA	Effective Medium Approximation
EMT	Effective Medium Theory
Et <sub>3</sub>	Ethyl group
FCC	Face-centered cubic
FDTR	Frequency Domain Thermoreflectance
GULP	General Utility Lattice Program
GGA	Gradient???

GGA+U	Gradient??? With U-factor
GST	Ge <sub>2</sub> Sb <sub>2</sub> Te <sub>5</sub>
HAMR	Heat Assisted Magnetic Recording
HCP	Hexagonal Close-packed
HJ-ME	Hasselman and Johnson – Maxwell Eucken
LAMMPS	Large-scale Atomic/Molecular Massively Parallel Simulator
LD	Lattice Dynamics
LDA	Local-density Approximations
LJ	Lennard-Jones
LUMC(s)	Large Unit Cell Molecular Crystal(s)
MD	Molecular Dynamics
ME	Maxwell Eucken
MFP	Mean Free Path
N-GST	Nitrogen-doped GST
NC(s)	Nanocrystal(s)
NCA(s)	Nanocrystal Array(s)
NEMD	Non-equilibrium Molecular Dynamics
NVE	Microcanonical ensemble enforcing constant number of particles, volume of simulation cell, and total energy
PBE	Perdew–Burke–Ernzerhof
PCBM	1-(3-methoxy-carbonyl)propyl-1-phenyl[6,6]C <sub>61</sub>
PCRAM	Phase Change Random Access Memory
SAM(s)	Self-assembled Monolayer(s)



SEM	Scanning Electron Microscope
SC	Simple cubic
SLL	Superlattice-like
VASP	Vienna <i>Ab initio</i> Simulation Package
vDOS	Vibrational Density of States
ZT	Thermoelectric Figure of Merit



# CHAPTER 1

## Superatom-Assembled Materials

### 1.1 Introduction

A superatom is a cluster of atoms behaving as a stable or metastable unit with emergent properties distinct from its constituent atoms [1]. A common example is the buckminsterfullerene ( $C_{60}$ ) molecule, where sixty carbon atoms form a cage-like structure with properties unlike elemental carbon. Superatoms are used as building blocks for assembling three-dimensional hierarchical materials (Figure 1.1). Analogous to atoms that occupy the lattice sites in a crystal, assembled superatoms occupy similar crystallographic sites to form a periodic superstructured solid (i.e., superlattice) with “made-to-order” properties [2]. The resulting solid is often termed as a designer or “LEGO” material [3]. In this work, I have investigated the thermal properties of nanoscale superstructured solids built from two classes of organic-inorganic superatoms - monodispersed nanocrystals (i.e., each nanocrystal diameter varies less than 10% from the mean diameter) and inorganic-organic superatoms of precise stoichiometric composition.

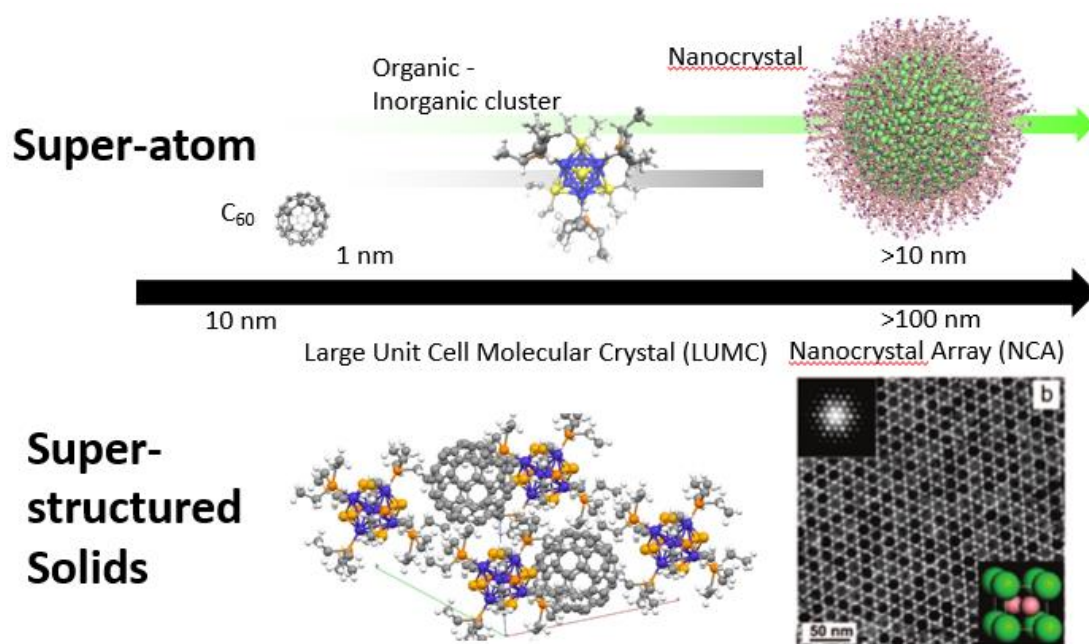


**Figure 1.1 Supratoms and Molecular Solids.**  $C_{60}$ , inorganic-organic clusters, and nanocrystals can assemble into molecular solids [2,4] with tailored properties.

## 1.2 Nanocrystal Arrays

A nanocrystal is built from inorganic cores 2 – 20 nm in diameter encapsulated in a layer of organic ligands. Each core contains hundreds to thousands of atoms and can be a semiconductor, metal, and/or magnetic material. Due to the small number of core atoms, the nanocrystal's electronic, optical, and magnetic properties become tunable with its size-dependent electronic band structure.

Electronic or optoelectronic devices will contain layers or large-area arrays of these nanocrystals. A nanocrystal array (NCA) is a close-packed periodic structure of nanocrystals that self-assembles from a colloidal suspension through spin-coating, drop-

casting, or inkjet printing (Figure 1.2). A critical criterion needed for self-assembly into a periodic crystal-like structure is the monodispersity of the cores. Monodispersity can be achieved through selective surface passivation with organic ligands during the colloidal synthesis process. The resulting macroscopic three-dimensional superstructured material contains well-ordered domains that can span several microns [2,5,6] and has an electronic band structure that is further tunable through the nanocrystal composition and size [2]. Due to this tunability and the inexpensive solution-based fabrication technique, NCAs have been proposed as cost-effective and versatile alternatives for expensive single-crystal semiconductors in field-effect transistors [7], memory devices [8], light-emitting diodes [9], photodetectors [10,11], solar cells [12–14], and thermoelectric generators [15–17].

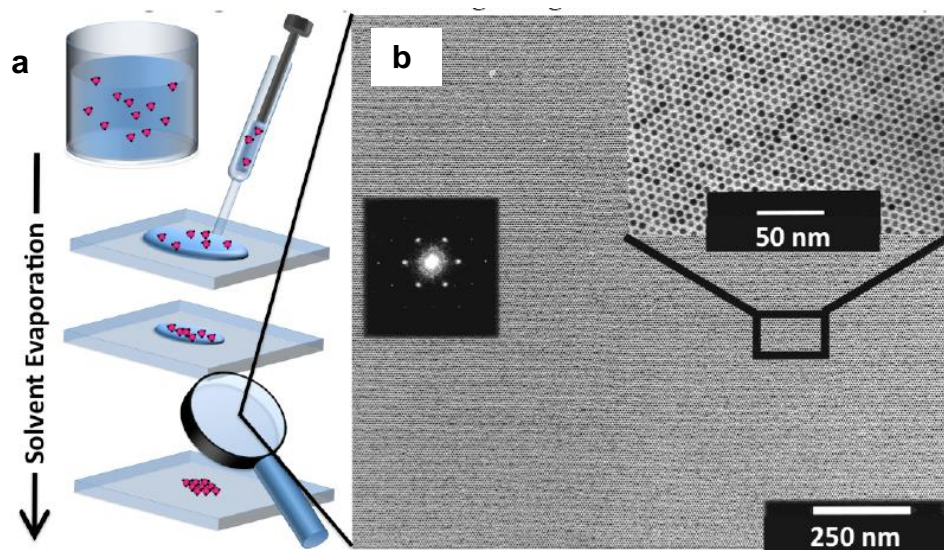


**Figure 1.2 NCA Synthesis.** **a**, Dropcasting technique. **b**, NCA with long-range order [18].

Extensive efforts have been made to understand and improve the electronic and optoelectronic properties of the NCAs [2]. Little is known, however, about the nature of thermal transport in this class of material. Understanding thermal transport in a material is critical [19,20] in any device roadmap for managing the heat generated as a parasitic byproduct of device operation. Without proper considerations, a device efficiency, efficacy, and lifetime will be adversely affected. Any proposed solutions to this problem will be ineffective without a proper understanding of the thermal transport in NCAs. In addition, knowing the thermal transport mechanisms in NCAs can guide the design of low thermal conductivity NCAs to increase the efficiency in thermoelectric devices.

The organic-inorganic material system closest to the NCAs with reported thermal transport studies is the self-assembled monolayers (SAMs) on inorganic bulk substrates [21–23]. A SAM is a monolayer of organic molecules that forms on an inorganic substrate due to the good bonding affinity between the functional end groups of the molecules with the inorganic bulk substrate. Typically, a SAM is sandwiched at the interface of two inorganic substrates to form a SAM junction. Using both experimental and computational techniques [24,25], thermal transport in SAMs is found to be largely hindered at the organic-inorganic interfaces with ballistic transport occurring within the molecules themselves [26]. Heat transfer in this hybrid material is independent of pressure and molecule length (beyond a certain chain length) [23,27–29] but dependent on the interfacial bonding strength [30–32]. In addition, a SAM junction can act as a thermal bridge to increase thermal transport between a metal-dielectric interfaces [32].

Although the ligand layer on a nanocrystal resembles a SAM on a curved surface, it is distinctly different from a SAM when the nanocrystal is part of an array. An NCA is a three-dimensional material with interdigitated ligands from neighboring cores that themselves form a higher-order periodicity in the material, resulting in a vast network of inorganic-organic and organic-organic interfaces. The presence of this higher-order periodicity may give rise to a novel two-tier phonon system in NCA (Figure 1.3). In contrast, SAMs are two-dimensional molecular monolayers that self-assemble on bulk inorganic substrates in a regular pattern. The added structural complexities in NCAs, hence, pose the question of whether the properties of an NCA can be inferred from those of a comparable SAM. The study of thermal transport in NCAs is, thus, an important endeavor for pushing our scientific understanding to alleviate the critical engineering problem of thermal management and, therein, increase device efficiency.

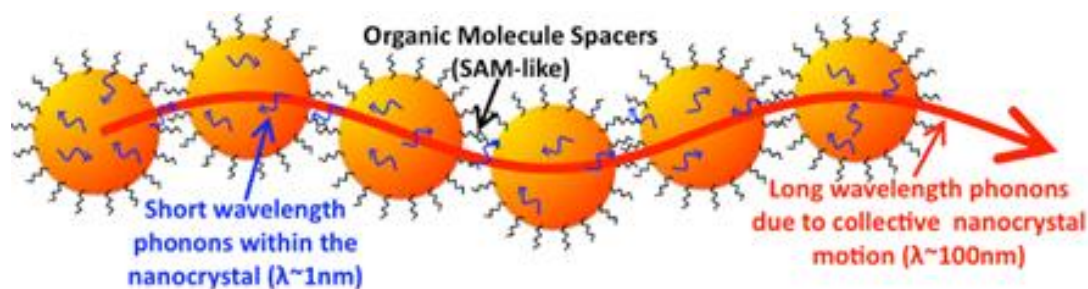


**Figure 1.3 Two-tier phonon system in NCA arising from two periodic lengthscales: Interatomic distance in a nanocrystal and inter-nanocrystal in the NCA.**

### 1.3 Large Unit Cell Molecular Crystals

Molecules can pack periodically to form a molecular crystal. For example, a  $N_2$

(simple molecule) or  $C_{60}$  (superatom) crystal. Molecules in these assembled crystals are stoichiometrically precise, in contrast to with the less exact nature of nanocrystals in an NCA. In my work, I have looked at large unit cell molecular crystals (LUMCs) assembled from superatoms by our collaborators at Columbia University [4]. These LUMCs have nanometer-size lattice constants, which is an order of magnitude bigger than those found in many atomic crystals.

In a molecular crystal, individual molecules are typically held together by weak size-dependent van der Waals forces (i.e., comparatively weaker than metallic, covalent, and ionic bonds) [1]. In some molecular crystals, stronger electrostatic, hydrogen, and/or halogen bonds may also exist between the molecules through the polar nature of these molecules or overlap interactions of the  $\pi$ -orbitals. The strength of these intermolecular forces and the bonding environment within a molecule give rise to the various properties (e.g. semi-conducting, conducting or magnetic) found in these crystals. A common example of an LUMC is the fullerene crystal (e.g.,  $C_{60}$  crystal).

### **1.3.1 Molecular Crystals of $C_{60}$**

A  $C_{60}$  molecule is a symmetric cage-like structure of sixty carbon atoms bonded together with alternate single ( $\sigma$ ) and double ( $\pi$ ) bonds [33]. This structure has a relatively high electron affinity with a large number of  $\pi$ -orbitals protruding from the surface that give rise to electronic properties that make  $C_{60}$  a promising self-assembled electronic material [34].

The basic fullerene architecture is also pliable to structural modifications to form functional materials [35]. The cage structure may be doped with other atoms or ions,



modulating its electronic and magnetic properties [36,37]. For example, fullerenes become superconducting when doped with alkali atoms [38–40]. Fullerene assemblies are successfully used in thin-film organic solar cells. The most widely used fullerene-derived molecule in solar cells is the PCBM [1-(3-methoxy-carbonyl)propyl-1-phenyl][6,6]C<sub>60</sub>] which is a C<sub>60</sub> molecule functionalized with an organic molecule to enhance its solubility for fabrication [41,42].

The thermal conductivity of C<sub>60</sub> crystal has been previously studied [43,44]. Its temperature dependent thermal conductivity trend shows a discontinuous drop at a temperature of 260 K upon heating, coinciding with a transition from a low temperature simple cubic (SC) to a high temperature face-centered-cubic (FCC) packing. In a dielectric crystal, the dominant heat transfer mode is through lattice vibrations called phonons [45]. The Debye model is typically used to describe thermal transport in a crystal and assumes a single group velocity for all the phonons propagating in a solid. As temperature increases, phonon-phonon scattering processes increase, which lowers the thermal conductivity. This scattering process, however, does not explain the observed discontinuity in the C<sub>60</sub> crystal. Instead, at temperatures below 260 K, C<sub>60</sub> molecules jump between discrete orientations of comparable energy levels [46,47]. These discrete jumps transform into a continuous diffusive rotational motion at temperatures above 260 K [46,47]. This orientation disorder scatters phonons more readily, creating the observed discontinuity drop as well as the subsequent plateau in the thermal conductivity at and above temperatures of 260 K [43].

In contrast, the vibration spectrum in a C<sub>60</sub>/C<sub>70</sub> compact (a polycrystalline disordered solid formed by compressing the C<sub>60</sub>/C<sub>70</sub> powder under high pressure) is

found to be dominated by localized modes [48]. In a disordered or amorphous-like material, the lack of a well-defined lattice structure negates the existence of phonons as the major form of heat carriers. Thermal energy is, instead, slowly transferred through the solid by localized vibrations affecting the neighboring domains, resulting in a low thermal conductivity value. The common model used to elucidate these localized modes is the Einstein model where individual entities in a solid vibrate independently (as opposed to collectively) at a same frequency [45]. By measuring the temperature dependent specific heat capacity and thermal conductivity of the  $C_{60}/C_{70}$  compact, the nature of thermal vibrations across a wide temperature range was studied. Below the temperature of 4 K, collective vibrations of the  $C_{60}/C_{70}$  molecules dominate, a characteristic of amorphous solids [48]. Between temperatures of 4 K and 40 K, the specific heat results point to the existence of Einstein oscillators in the form of rigid vibrations of the whole  $C_{60}/C_{70}$  molecules. Above the temperature of 40 K, the surface vibration modes within a  $C_{60}/C_{70}$  molecule increase the heat capacity of the compact [48].

### **1.3.2 Molecular Crystals of Inorganic-organic Superatoms**

Molecular crystals are commonly assembled with mono-species superatoms made of inorganic and/or organic elements. The final structure and properties of these crystals, as mentioned earlier, are a result of the delicate amalgamation between the various intermolecular forces (i.e., van der Waals, electrostatic, hydrogen- and halogen-bonds) and, if present, the overlap of the  $\pi$ -orbitals in the superatoms [49]. In the case

of overlapping  $\pi$ -orbitals creating an extensive network, electrons can readily travel between molecular sites giving rise to electronic properties in some of these LUMCs. Although these conducting/semi-conducting crystals have been available for some time, their electronic properties have been largely unexplored except for some notable cases [50–52].

Recently, our collaborators from Columbia University synthesized a new class of molecular crystals [4]. Instead of using a single superatom species, two different but electronically and structurally compatible superatoms are combined to form atomically-precise binary crystals. An electron-rich superatom [i.e.,  $\text{Co}_6\text{Se}_8(\text{PET}_3)_6$  (**1**),  $\text{Cr}_6\text{Te}_8(\text{PET}_3)_6$  (**2**), and  $\text{Ni}_9\text{Te}_6(\text{PET}_3)_8$  (**3**) see Figure 1.4] is combined with an electron-poor superatom (i.e.,  $\text{C}_{60}$ ) to produce a crystal exhibiting collective properties such as electrically conducting networks and magnetic ordering [4] (Figure 1.5).

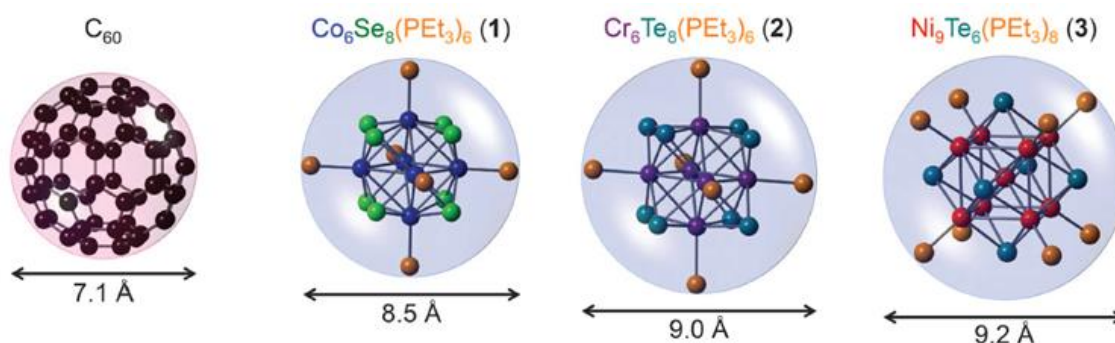


**Figure 1.4 Structures of the superatoms.** The ethyl groups ( $\text{Et}_3$ ) on the phosphines (P) were removed to clarify the view. Figure is modified from ref [4].

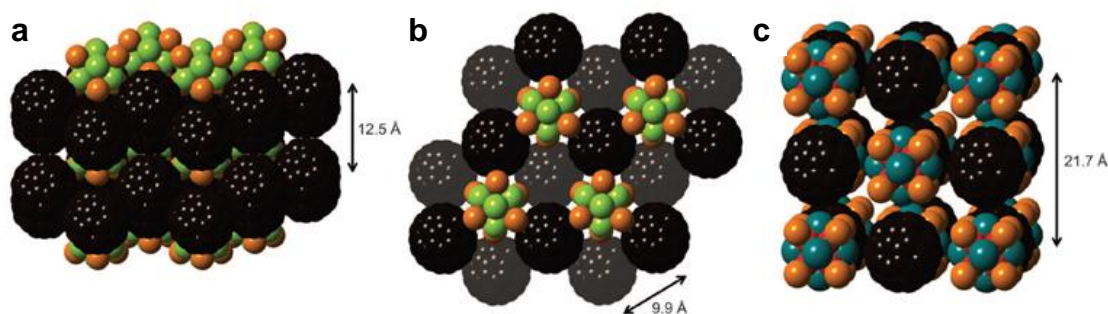


**Figure 1.5 Structures of molecular crystals.** **a**, Structure of  $\text{Co}_6\text{Se}_8(\text{PEt}_3)_6 \cdot 2\text{C}_{60}$  showing the crystal packing looking along the  $ab$  plane. **b**, down the  $c$  axis. **c**, Structure of  $\text{Ni}_9\text{Te}_6(\text{PEt}_3)_8 \cdot \text{C}_{60}$ . Carbon, black; nickel, red; cobalt, blue; phosphorus, orange; tellurium, teal; selenium, green. The ethyl groups on the phosphines were removed to clarify the view. Figure is modified from ref [4].

With  $\text{C}_{60}$  and superatom type (1) or (2), a hexagonally close-packed structure is obtained while  $\text{C}_{60}$  and (3) produces a rock-salt structure. Crystals from (1) and (2) are fair electrical conductors at room temperature with resistivities on the order of 10 ohm-cm [4] but become gapped semiconductors with decreasing temperature. In addition, magnetic properties differ with different inorganic core elements. These results show that properties of such superatom-assembled crystals can be tailored by changing the constituent elements in them. Further, due to the strong intermolecular forces created through electron transfer, structures of such crystals are more stable than conventional large unit cell molecular crystals, making interstitial insertion a feasible method for tuning properties [49].

Similar to the nanocrystal arrays, the thermal conductivity of these newly synthesized crystals is unknown although their electronic properties have been investigated. Except for  $\text{C}_{60}$  and certain fullerene-derived crystals, heat transport

mechanisms in this class of large unit cell molecular crystals have not been studied. Several scientifically interesting questions for thermal transport in these crystals include: Is heat transfer in large unit cell molecular crystals crystalline or amorphous in nature? Do the orientations of the molecules scatter phonons as postulated in the case of a  $C_{60}$  crystal? Can we ignore the intra-molecular thermal vibrations (i.e., localized surface vibration modes) when considering the heat flow in these crystals? Will there be a significant contribution to thermal conductivity from the collective modes? Answering these questions will shed light on the nature of thermal transport in this class of materials.

## 1.4 Overview and Scope

The common theme of this work is the study of thermal transport in novel three-dimensional superstructured organic-inorganic materials. Both experimental [i.e., frequency domain thermoreflectance (FDTR) and differential scanning calorimetry (DSC)] and computational techniques [i.e., molecular dynamics (MD), density functional theory (DFT), and lattice dynamics (LD)] are used to characterize and understand the thermal transport mechanisms in nanocrystal arrays (NCAs) and large unit cell molecular crystals (LUMCs). The chapters are organized as follows:

Experimental characterizations of the heat capacity and thermal conductivity for a wide range of NCAs are presented in Chapter 2. The FDTR working principle is briefly discussed. Simple MD modeling was also performed to support and elucidate the experimental trends. A variety of NCAs with semiconducting and metallic cores of different core diameters were measured at room temperature. NCA temperature dependent thermal conductivity behaviors were probed down to liquid helium boiling

temperature. The effects of changing the chemical compositions of the core and ligand to thermal conductivity were also studied. From these trends, important conclusions on the thermal transport mechanisms in NCAs were drawn.

Further study of the thermal transport in NCA are performed in Chapter 3 using MD and LD. Vibrational spectra of a core and a single molecule were obtained to assist in understanding the effect of overlap in the vibrational states to the NCA thermal transport. An NCA model containing several hundred thousands of atoms that interact with realistic potentials was built and studied using MD. The NCA thermal conductivities were predicted using non-equilibrium molecular dynamics technique (NEMD) for different thicknesses, core diameters, and atomic masses in cores. The interfacial thermal conductances between the core and the passivating ligands were obtained for different core diameters and temperatures using NEMD. The importance of the interfacial thermal conductance in the thermal transport is further clarified.

In Chapter 4, our preliminary measurements and predictions of thermal properties of the LUMCs are presented. We studied a class of LUMCs synthesized by collaborators from Columbia University. Experimental measurements of the heat capacity and thermal conductivity were performed. Theoretical determination of the heat capacity was also calculated with vibrational frequencies obtained from DFT.

Chapter 5 contains a brief discussion of other projects that resulted in publications. There are four such successful projects among the projects undertaken.

In Chapter 6, the major contributions of the main work are presented with suggestions for future work.

## CHAPTER 2

# Thermal Transport in Three Dimensional Nanocrystal Arrays

## 2.1 Overview

Arrays of ligand-stabilized colloidal nanocrystals with size-tunable electronic structure are promising alternatives to single-crystal semiconductors in electronic, optoelectronic, and energy-related applications [2,7,13,53,54]. Hard-soft interfaces in these nanocrystal arrays (NCAs) create a complex and uncharted vibrational landscape for thermal energy transport that will influence their technological feasibility. In this chapter, we present the thermal conductivity measurements of NCAs (having CdSe, PbS, PbSe, PbTe, Fe<sub>3</sub>O<sub>4</sub>, and Au core) and reveal that energy transport is mediated by the density and chemistry of the organic/inorganic interfaces as well as the volume fractions of nanocrystal cores and surface ligands. NCA thermal conductivities are controllable within the range 0.1–0.3 W/m-K, and only weakly depend on the thermal conductivity of the inorganic core material. This range is 1,000 times lower than the thermal conductivity of silicon, presenting challenges for heat dissipation in NCA-based electronics and photonics. It is, however, 10 times smaller than that of Bi<sub>2</sub>Te<sub>3</sub>, which is advantageous for NCA-based thermoelectric materials [55]. [Published in “Surface chemistry mediates thermal transport in three-dimensional nanocrystal arrays”, W-L.

Ong, S.M. Rupich, D.V. Talapin, A.J.H. McGaughey, J.A. Malen, *Nat. Mater.* **12** (5), 410-415.]

## **2.2 Introduction**

As discussed in Chapter 1, colloidal nanocrystals (NCs) self-assemble into NCAs with electronic and optical properties that can be broadly tuned by nanocrystal composition and size [2,5,7,13,53,56,57]. In metals, the majority of heat is carried by electrons, while in semiconductor and insulating crystals, thermal conductivity arises from the transport and scattering of quantized vibrations that are born from the periodic atomic lattice, i.e., phonons. Our NCAs are assembled by our collaborators from the chemistry department of The University of Chicago. These NCAs are non-metallic and have a vibrational structure that is complicated by compositional heterogeneity and periodicity at two length scales: the atomic lattice within each core and the array of periodic cores separated by ligand monolayers. Studies of planar self-assembled monolayer (SAM) junctions have shown that surface chemistry can control energy transport at the interface between two solids [58]. The question we set to answer is how thermal transport in a bulk three-dimensional NCA with its complex network of internal interfaces will be influenced by chemistry between the core and ligands.

## **2.3 Materials and Methods**

### **2.3.1 Nanocrystal Arrays**

Our collaborators from The University of Chicago prepared a series of NCAs with



varying core diameters, core materials, and ligand groups (Table 2.1) through spin-coating concentrated colloidal solutions onto silicon wafers [56]. During film formation, the monodispersed nanocrystals self-assembled into arrays, as seen in Figures 2.1a-c. For thermal conductivity measurements, the NCA films were coated with a gold transducer (150 to 250 nm thick) by electron-beam evaporation.

**Table 2.1 Nanocrystals and ligands used for the preparation of NCAs thin films.**

Core	Diameter (nm)	Ligand	Core Type
CdSe	3.5, 4.1	n-Tetradecylphosphonic acid (TDPA)	Semiconductor
	5.2	n-Octylphosphonic acid	
	4.8	(N <sub>2</sub> H <sub>5</sub> ) <sub>2</sub> In <sub>2</sub> Se <sub>4</sub>	
PbS	3.5, 4.5, 5.2	Oleic acid (OA)	Semiconductor
	7.5	Oleic acid, Nonanoic acid (NA), Na <sub>3</sub> AsS <sub>3</sub> , N <sub>2</sub> H <sub>4</sub>	
PbSe	7.5	Oleic acid	Semiconductor
PbTe	7.5	Oleic acid	Semiconductor
Fe <sub>3</sub> O <sub>4</sub>	4.5, 8	Oleic acid	Metal Oxide
Au	4.5	n-Dodecanethiol	Metal

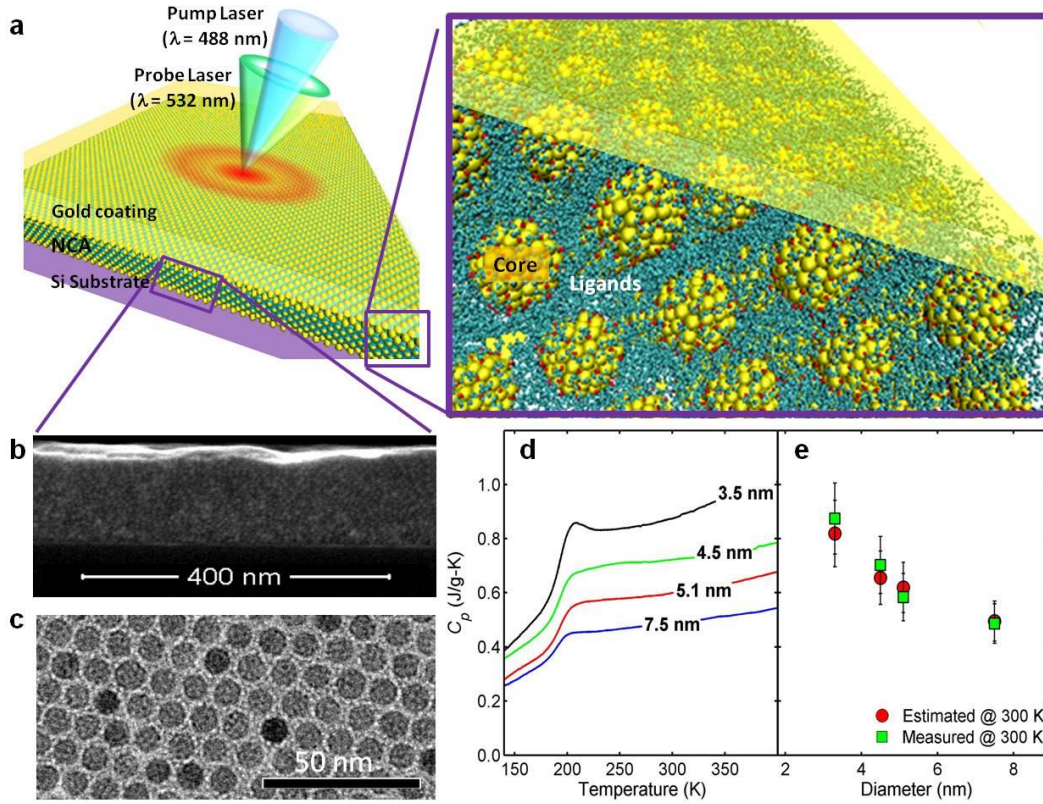


**Figure 2.1 Structure and heat capacity of NCA films.** **a**, Schematic of a gold-coated NCA film where an intensity modulated pump laser periodically heats the sample and a probe laser senses the resultant temperature change by thermorefectance to measure thermal conductivity. The magnified view to the right depicts the NCA thin film. **b**, SEM cross-sectional image of a 7.5 nm diameter PbS NCA film. **c**, Planar TEM image of a 8 nm diameter  $\text{Fe}_3\text{O}_4$  NCA film showing a regular close-packed arrangement. **d**, Specific heat capacity data as a function of temperature for a diameter series of PbS nanoparticles coated with oleic acid ligands. **e**, The specific heat capacity of a NCA at 300 K can be estimated as a mass-weighted function of the specific heat capacities of the core material ( $C_{core}$ ) and the ligand ( $C_{Ligand}$ ) (i.e.,  $C_P = m_{core} C_{core} + m_{Ligand} C_{Ligand}$  where  $m_{core}$  is the mass-fraction of the core and  $m_{Ligand}$  is the mass-fraction of the ligand). The plot shows the measured and estimated values using bulk values of PbS ( $C_{core} = 0.19$  J/g-K, ref. [59]) and oleic acid ( $C_{Ligand} = 2.043$  J/g-K, ref. [60]).

### 2.3.2 Frequency-domain thermal reflectance (FDTR)

To measure the thermal conductivity of the NCA thin films, we employed the FDTR technique [61]. Our FDTR technique, diagrammed in Figure 2.2a, employs two continuous wave lasers (Coherent Inc.) to heat the sample and measure its thermal response to identify the unknown NCA thermal conductivity [24].

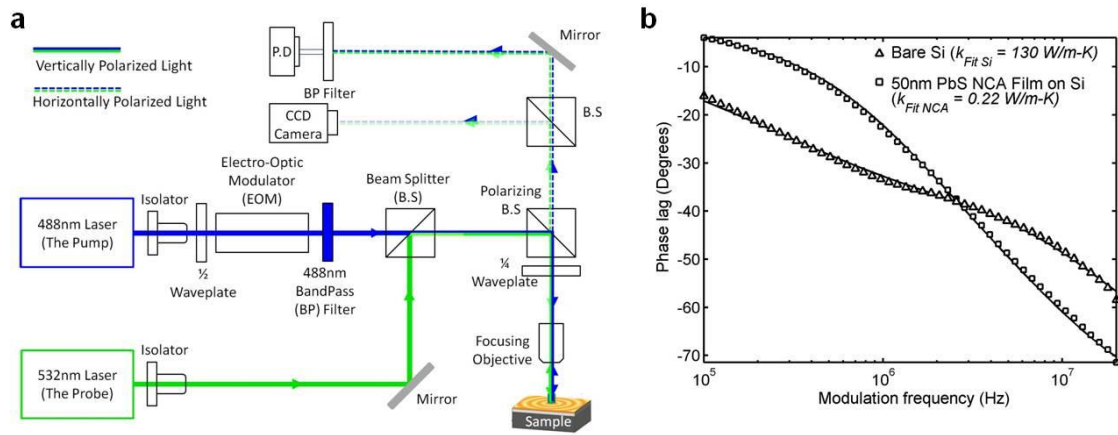


**Figure 2.2 FDTR schematic and data.** **a**, An intensity modulated pump laser (488 nm) is periodically modulated by an electro-optic modulator and heats the sample periodically. An unmodulated probe laser (532 nm), coincident with pump at the sample surface, senses the periodic temperature change by thermoreflectance. The thermoreflectance signal is monitored by a lock-in amplifier, measuring the phase lag of the temperature change relative to the heat flux as a function of frequency. **b**, FDTR phase lag data and fits, plotted as a function of modulation frequency for bare silicon and a NCA film on silicon. The differences in the signals indicate a high sensitivity to the NCA thermal conductivity.

The 488 nm laser (“the pump”) is intensity-modulated and periodically heats the gold surface while the 532 nm laser (“the probe”) continuously monitors the resultant thermal response through the thermoreflectance of a gold (Au) layer that is coated on

the NCA surface. The pump is modulated sinusoidally from 100 kHz to 20 MHz. The resulting probe signal is measured using a radio frequency lock-in amplifier (Stanford Instrument, SR844), producing a set of frequency-dependent phase data, related to the thermal properties of the sample. These data are then fit using a thermal conduction model (see Appendix A Table A1 for fitting parameters) to determine the unknown thermal conductivity of the NCA [24].

The phase data and fits shown in Figure 2.2b for a bare silicon substrate and a silicon (Si) substrate with a 50 nm PbS NCA demonstrate the high sensitivity of the FDTR technique to the presence of the NCA. The resulting thermal conductivity has an uncertainty of 15-20% due to goodness of fit of the heat conduction model and input parameter uncertainties (NCA thickness, NCA heat capacity, Si substrate thermal conductivity, Au film thermal conductivity, Au film thickness, laser spot diameter) [61]. To minimize this uncertainty, we separately measured the thermal conductivities of the Si substrate (using FDTR) and gold film (using either FDTR or the Wiedemann-Franz law through sheet resistance measurements made on a dielectric sample that was coated with Au at the same time as the NCAs). The largest uncertainty comes from thickness variations in the NCA film, which were quantified to be approximately 10% of the film thickness by both SEM and AFM (Appendix A Table A2 for sample images).

Experimentally measured heat capacity values were used as input to the heat conduction model for temperatures greater than 150 K. The fitting model is insensitive to the exact NCA heat capacity values at lower temperature. At these low temperatures, changing the heat capacity values by an order of magnitude causes the resultant thermal conductivity value to vary within the experimental error. This is a result of the pump

being typically modulated with a period much longer than the NCA film thermal time constant ( $\tau_{NCA} = L_{NCA}^2 / \alpha_{NCA}$ , where  $L_{NCA}$  is the NCA film thickness and  $\alpha_{NCA}$  is the NCA thermal diffusivity). In this regime the NCA heat capacity becomes unimportant for determining the thermal conductivity because the temperature profile in the film is quasi steady-state. For example, the thermal time constant at temperatures of 150K and 300K for a 50 nm thick 7.5 nm diameter PbS NCA are approximately 19 ns and 27 ns, restricting the heating frequency to below 52 MHz and 36 MHz for quasi steady behavior and insensitivity to the NCA heat capacity.

### 2.3.3 Molecular Dynamics (MD)

To gain additional insight into the thermal conductivity measurements, molecular dynamics simulations were performed on a simplified non-dimensionalized NCA model as shown in Figure 2.3.

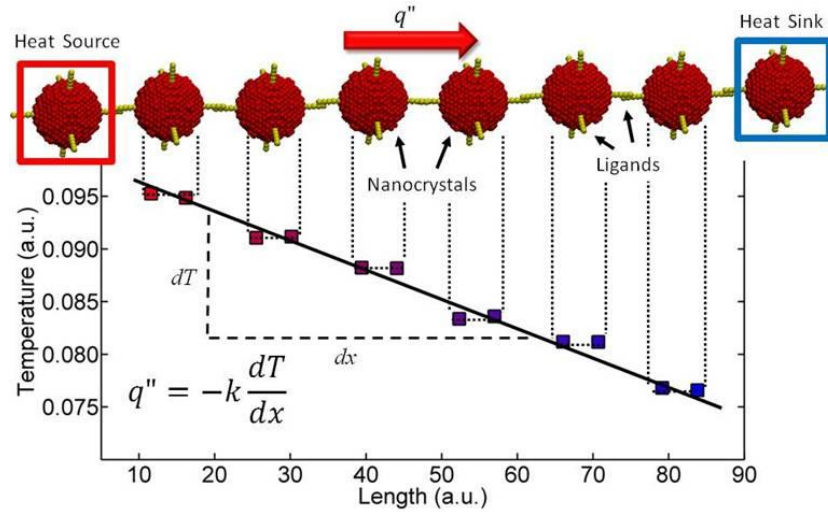


**Figure 2.3 MD simulation model.** The model used in the MD simulations simplifies a NCA into a linear chain. In this case, eight cores (red spheres) with their tethered ligands (six yellow chains on each core with two along each Cartesian direction)

are shown. A typical simulated steady-state temperature profile after a heat flux is applied is plotted below. Each point represents an average temperature in one-half of a core, depicting a constant temperature profile in each core with significant temperature drops across the ligand bridges between the cores.

This model mirrors several salient features of real NCAs. Notably, (i) a similar mass ratio of the core and ligand species, (ii) overlapping ligands between neighboring nanocrystals, and (iii) weak inter-ligand interactions. Molecular dynamics simulations are performed using the LAMMPS package [62] to predict the thermal conductivity of a simple NCA model. The basic motif is a sphere of atoms (the core) with six linear chains of atoms (the ligands) perpendicularly grafted onto its surface in the three Cartesian directions (Figure 2.3). The core is carved from a FCC lattice and contains between 135 and 1721 atoms, interacting via a 12-6 Lennard-Jones (LJ) potential with length scale  $\sigma$  and energy scale  $\epsilon$ . A single ligand is built from a straight chain of five atoms that are bonded to their closest neighbours using Hookean springs of stiffness  $118\epsilon$  at an equilibrium distance of  $1.1\sigma$ . An additional three-body bending energy term of the form  $B_{cc}(1 + \cos\theta)$  with  $\theta = 180^\circ$  and  $B_{cc} = 400\epsilon$  constrains the ligand linearly. The atom in the ligand closest to the core is bonded to the four nearest core atoms with the same set of Hookean springs. This geometry results in an equilibrium angle of  $\varphi_0 = 135^\circ$  between each of these four core atoms and the two ligand atoms that are nearest to the core. This angle is enforced through a three-body bending energy term,  $B_{cNP}(\varphi - \varphi_0)$  where  $B_{cNP} = 200\epsilon$ . This motif is repeated along the  $x$ -axis to form a chain of desired length. Alternate motifs along the chain are offset at a distance of  $1.1\sigma$  in the  $y$ -

direction to prevent atoms in the overlapping ligands (two atoms in each consecutive ligand overlap) from occupying identical initial positions. The overlapping ligands interact weakly via a 12-6 LJ potential with length scale  $\sigma$  and energy scale  $0.2\epsilon$ , mimicking the weak interactions between nanocrystals in the NCA. The ends of the non-overlapping ligands in the  $y$ - and  $z$ -directions are tethered to their initial positions using a Hookean spring with stiffness identical to the weak LJ interactions between the overlapping linear chains.

Fixed boundary conditions were imposed along the three Cartesian directions. The system was initially thermalized to a dimensionless temperature of 0.165 and then allowed to relax and equilibrate in the  $NVE$  ensemble (i.e., the total number of particles, system volume, and total system energy are kept constant). A non-equilibrium molecular dynamics (NEMD) technique was then employed to impose a heat flux across the system, leading to a steady-state temperature gradient that can be used with the Fourier law to predict thermal conductivity [63]. The motif at the left edge of the system was used as the heat source while the motif at the right edge was the heat sink (Figure 2.3). Using a dimensionless time-step of 0.001, one million steps were used for relaxation and equilibration, after which another 30 to 50 million steps were used in the NEMD simulations to reach steady-state (i.e., the temperature gradient across the system remains invariant) before the start of the data collection period.

In all simulations, the dimensionless steady-state system temperature was about 0.0852 with a dimensionless temperature difference between 0.00827 and 0.02 established across the system during NEMD. The temperature gradient (Figure 2.3) was averaged from five to eight blocks of ten million time steps and the same cross-

sectional area was used in all simulations to calculate the thermal conductivity. An overall mean and variance for the calculated thermal conductivity were obtained by combining the individual means and variances from six to eight different initial conditions using the pooled mean and variance estimators [64].

The MD simulation data are plotted in Figures 2.5a, 2.6a and 2.9a. In Figure 2.6a, the simulation data has been scaled by a factor of 1.7 on the y-axis and 0.5 on the x-axis in order to make the experimental and simulation data share the same set of axes for easier representation. The overall upward trend is, however, unaffected. Although the simulation values (which are dimensionless) cannot be directly compared with experiments, these non-dimensionalized predictions can elucidate the transport physics in NCAs through the predicted trends for the different experimental parameters (i.e., film thickness, nanocrystal diameter, and mass ratio).

#### **2.3.4 Vibrational density of states calculation**

The model used for calculating the nanocrystal array (NCA) vibrational density of states (vDOS) consists of the Au core and a monolayer coating of ligands. The united atom method is used to simplify the ligand (dodecanethiol,  $C_{12}H_{25}SH$ ) by lumping the mass of each hydrogen atom with the carbon/sulfur atom that it is bonded to [65]. The interatomic potentials used are the same as those used by Luo et al. [66], except for the interactions between the Au atoms, which are described using an embedded-atom method (EAM) potential [67]. This EAM implementation results in a bulk Au density of states that agrees well with experimental measurements [68].

The Au core is a sphere of diameter 2.8 nm carved out from a face centered cubic



(FCC) crystal having a lattice constant of 4.08 Å. Using the LAMMPS package [62] to perform molecular dynamics (MD) simulations, the core was first thermalized and equilibrated at a temperature of 400 K for 1 ns using velocity rescaling. It was then cooled at a rate of 100 K/ns to a temperature close to 0 K (i.e.,  $1 \times 10^{-6}$  K) using a Nose-Hoover thermostat. The simulation time step was 1 fs. This procedure produces a fully relaxed Au core that can be used in lattice dynamics calculation [69] to obtain the vDOS.

The dodecanethiol ligand was initialized as a linear chain of twelve carbon atoms connected in series and terminated with a sulfur atom. It was subjected to the same temperature cycling process as the Au core to get a fully relaxed structure at a final temperature of 0 K. The final structure of the relaxed ligand obtained was as expected with the equilibrium torsional and 3-body angles in the ligand similar to experimental values.

The nanocrystal consists of the Au core and 112 ligands. These ligands were initialized as in the single ligand case and placed perpendicularly at random positions located 5 Å above the core surface with the sulfur atoms nearest to the core. This configuration was thermalized at a temperature of 400 K and equilibrated for 5 ns to allow the ligands to explore the energy surface and rearrange into a minimum energy configuration. Afterwards, an identical cooling temperature cycle as described earlier was applied to obtain a relaxed nanocrystal.

Using these three relaxed structures, lattice dynamics calculations were performed using the GULP package [70]. The resulting vibrational states were binned with intervals of 0.1 THz and plotted as the vDOS in Figure 2.4.

## 2.4 Result and Discussion

### 2.4.1 Heat Capacity

Our collaborators measured the specific heat capacity ( $C_p$ ) of the NCAs using the differential scanning calorimetry (DSC). The measured  $C_p$  varies with temperature and nanocrystal size as shown for a diameter series of PbS NCAs in Figures 2.1d and 2.1e. The abrupt change in slope in  $C_p$  around 200 K is the result of a glassy transition of the oleate ligands [71,72], as these unsaturated hydrocarbon tails do not crystallize at the nanocrystal surface. We find that  $C_p$  can be estimated from a weighted average based on the constituent mass-fractions and the bulk specific heat capacities of the inorganic core material and the ligand (Figure 2.1e).

Molecular dynamics simulations and harmonic lattice dynamics calculations were performed to elucidate how the vibrational structure of a nanocrystal is related to its constituent core and ligands. The vibrational density of states (vDOS) of a 2.8-nm diameter Au nanocrystal and its constituent Au core and dodecanethiol ligands are shown in Figure 2.4. The  $C_p$  of solids results from occupation of the vDOS according to Bose-Einstein statistics. All core vibrational states overlap with ligand states below the thermal activation frequency at 300 K. Higher-frequency ligand states have no corresponding core states to overlap with at higher temperatures. These two general features will be found for core materials of similar Debye temperature to Au (165 K). Similarities in the vDOS of the nanocrystal and its components thus explain why the measured  $C_p$  is consistent with the estimate based on mass fraction.

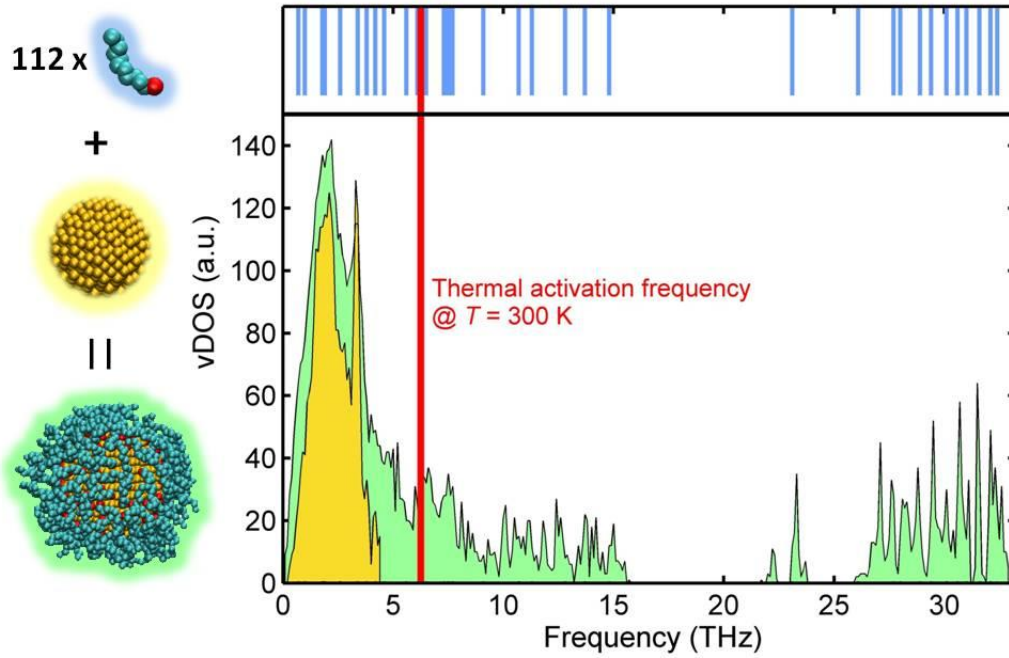


**Figure 2.4** Vibrational density of states (vDOS) of a 2.8-nm diameter Au nanocrystal and its individual constituents (Au core and a dodecanethiol ligand) predicted from lattice dynamics calculations. The blue vertical lines represent the vibrational spectrum of one ligand. The yellow region is the vDOS of the Au core, which is enclosed in the green vDOS of the nanocrystal. The vertical red line represents the thermal activation frequency ( $\frac{k_B T}{h_c}$ ) at a temperature of 300 K ( $k_B$  is the Boltzmann constant and  $h_c$  is the Planck constant).

#### 2.4.2 Thickness-dependent Thermal Conductivity

We measured a series of different film thicknesses for different NCAs at the temperature of 300 K and for CdSe NCAs at temperatures of 10 K, 77 K, and 300 K. In addition, we also simulated the effect of the film thickness on the NCA thermal conductivity. It is evident from both experimental and simulation results shown in Figure 2.5 that the NCA thermal conductivity is independent of its thickness. This

result paints a picture of diffusive thermal transport in NCAs that is dominated by short mean free path phonons. Furthermore, the thickness invariance indicates that our measured values are bulk-like and not distorted by thermal resistances at the Au-NCA and NCA-Si boundaries.

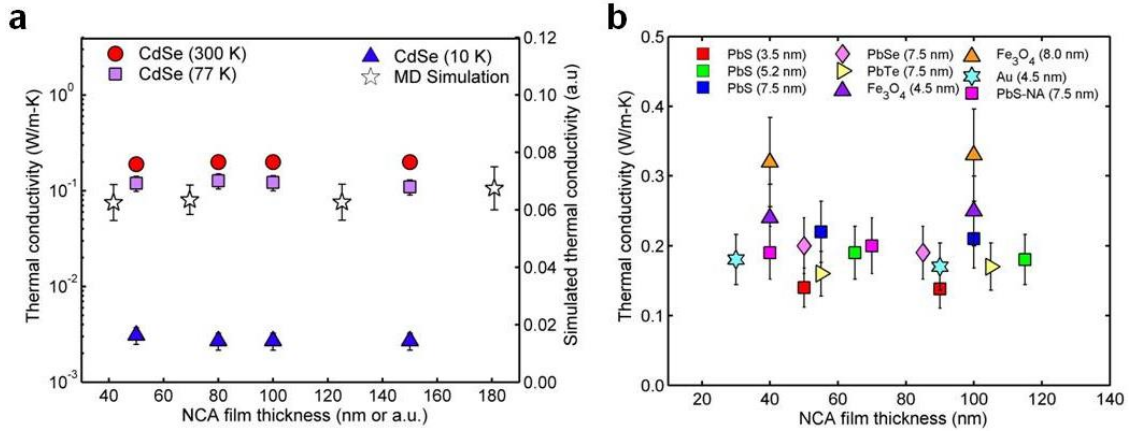


**Figure 2.5 Thermal conductivity thickness series for NCAs.** **a**, Film-thickness series for CdSe (diameter = 4.1 nm) NCA showing invariant thermal conductivity with thickness at temperatures of 10 K, 77 K, and 300 K. A similar trend is observed in the MD simulation result. **b**, The thermal conductivities of various NCAs at a temperature of 300 K showing invariance with thicknesses. The number in parentheses is the core diameter. The ligand groups for the different NCAs can be found in Table 2.1.

### 2.4.3 Core Diameter-dependent Thermal Conductivity

The measured thermal conductivity as a function of core diameter for CdSe, PbS, PbSe, Au, and Fe<sub>3</sub>O<sub>4</sub> NCAs is shown in Figure 2.6a. Regardless of the core material, the NCA thermal conductivity increases with increasing diameter. This diameter-dependence is also found in our simulations (Figure 2.6a). To understand these diameter-dependent trends, effective medium approximations (EMAs) of thermal

conductivity are compared with the data for PbS NCAs in Figure 2.6b.

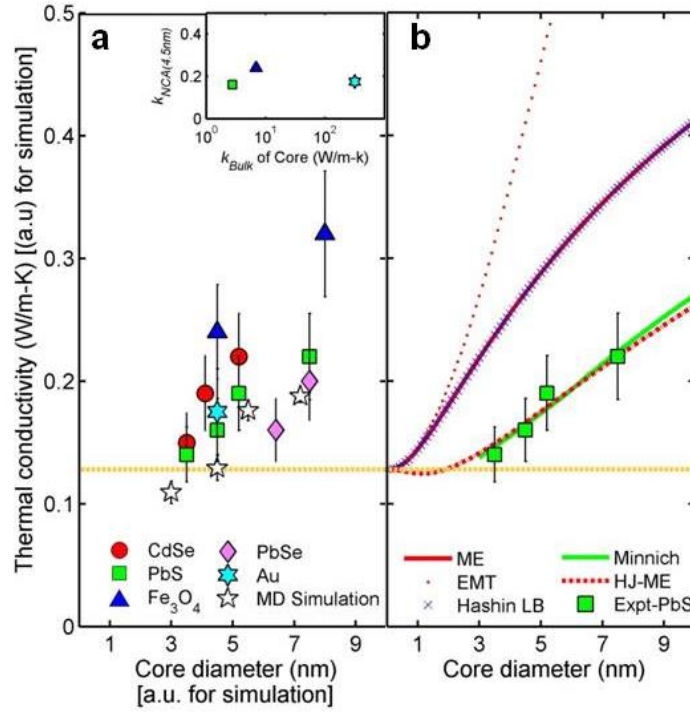


**Figure 2.6 Effects of NCA geometry on thermal conductivity.** **a**, Diameter series data for various NCAs have increasing thermal conductivity with core diameter regardless of core composition. The trend of the MD simulation results agrees with the experimental data. **Inset** shows that  $k_{NCA}$  does not strongly depend on the thermal conductivity of the bulk core material. The orange dotted line here and in **b** is the thermal conductivity of Pb-oleate at 300 K. **b**, Effective medium approximations cannot explain the PbS NCA data [73,74] without the use of a finite thermal conductance at the core-ligand interface integral to HJ-ME and Minnich models. These models clarify that increased  $k_{NCA}$  results from decreased interface density (from  $4.37 \times 10^8 \text{ m}^2/\text{m}^3$  to  $3.43 \times 10^8 \text{ m}^2/\text{m}^3$ ) and increased core volume fraction (from 0.24 to 0.43) over the diameter range 3.3–7.5 nm.

#### 2.4.4 Effective Medium Approximations

Available formulations of EMA consider a dispersion of particle inclusions within

a continuous matrix, which is representative of the NCA structure. We considered a series of EMA models and plot the most relevant ones together with the lead sulfide (PbS-Oleic acid) NCA diameter series in Figure 2.6b. The PbS diameter series is chosen as it contains the most data points and the variables required in the different EMA models are either known or can be reasonably estimated. The inputs to the EMA models are: the bulk thermal conductivity of the inclusions (nanocrystals), the bulk thermal conductivity of the matrix (ligands), the volume fractions of the inclusions and matrix, and, in some cases, the finite thermal interface conductance ( $h$ ) at the inclusions-matrix (nanocrystal-ligand) interface.

For PbS inclusions, the bulk thermal conductivity is available from Ref. [59]. As described below, however, the EMA model of Minnich et. al. [75] requires some modification. In PbS NCA, the matrix phase is oleic acid. The oleic acid ligands are covalently bound to the inorganic cores, creating structure that is otherwise absent in the bulk. To estimate the thermal conductivity of bound oleic acid ligands we used FDTR to independently measure the thermal conductivity of Pb-oleate (oleic acid terminated by a Pb atom; a waxy solid at 300 K). We find  $k_{Pb-O}=0.13 \pm 0.02$  W/m-K, which is 40% lower than liquid oleic acid [76]. Volume fractions of the respective phases are calculated based on a formulation found in Minnich et. al. [75] (see Appendix A Section I for these calculations). As  $h$  is unknown but required for some EMA models, it is chosen as a fitting parameter to the experimental data.

The available EMA models can be categorized into two classes: conventional EMA models and EMA- $h$  models that consider finite thermal interface conductance. For the first category, we considered: (i) the Maxwell-Eucken [73] model (ME), which has

spherical particles dispersed in a continuous matrix, (ii) EMT [73], which models the material as a random distribution of particles in a continuous matrix, and (iii) Hashin [74] self-consistent model (Hashin LB) which considers a statistically homogeneous and isotropic two-phase material with the thermal conductivity of the particle phase higher than the matrix phase. As seen in Figure 2.6b, these three models overestimated the NCA thermal conductivity. Hence, it can be seen that conventional EMA models are inadequate for explaining the thermal conductivity of the NCA diameter series.

The HJ-ME [77] and Minnich [75] EMA- $h$  models are also plotted in Figure 2.6b. In both cases,  $h$  is used as a fitting parameter to the experimental data. For the Minnich model, an additional complexity arises due to the need to consider a reduction in the thermal conductivities of the particle inclusions (nanocrystals) and matrix (ligands) due to boundary scattering. The original method presented in the Minnich model uses the respective materials' phonon group velocity and bulk mean free path (MFP) to estimate the thermal conductivity reductions. As the phonon group velocity and bulk MFP (and hence the  $h$ ) of PbS and oleic acid are either not available or difficult to estimate, we modify the original Minnich model by:

- i) Using the thermal conductivity accumulation function of bulk PbTe [78] to estimate the relative reduction of the thermal conductivity in the PbS cores. We map the size of the core diameter to the MFP to obtain the reduction in bulk thermal conductivity. This reduction creates a lower bound because, realistically, phonons with MFPs larger than the diameter are not completely excluded but instead contribute to the thermal conductivity with a MFP close to the diameter. As PbS and PbTe belong to the lead chalcogenide family, we believe this procedure to be a reasonable first

approximation.

ii) Ignoring the reduction in thermal conductivity in the matrix as its thermal conductivity is already low. The disordered structure in the Pb-Oleate film is unlikely to permit long MFP energy carriers that will be influenced by interface spacing.

Both the HJ-ME and modified Minnich models fit the experimental data well, giving  $h$  values of  $140^{+170}_{-80}$  MW/m<sup>2</sup>K and  $190^{+400}_{-130}$  MW/m<sup>2</sup>K. It appears that the additional complexity of Minnich does not lead to an improved fit – perhaps because  $k_{NCA}$  is insensitive to the thermal conductivity of the cores as shown in the inset to Figure 2.6a.

These fitted  $h$  values can be compared with measurements of thermal conductance through a planar alkanethiol-SAM/Au interface by Wang et. al. [26] and SAM junctions by Losego et. al. [58] and Wang et. al. [27]. This value is comparable with direct measurements of thermal conductance through a planar alkanethiol-SAM/Au interface ( $220 \pm 100$  MW/m<sup>2</sup>-K) [26]. SAM junctions [27,58] have a lower measured thermal conductance (25-70 MW/m<sup>2</sup>-K) because they include additive resistances due to the SAM itself and two interfaces. To compare with the fitted  $h$ , these SAM conductances should be approximately doubled. The agreement between the fitted  $h$  values and various SAM experimental measurements supports the use of EMA- $h$  models to predict the thermal conductivity of NCAs.

To summarize, conventional EMA models fail to predict the thermal conductivity vs. diameter trend measured in our NCA films. The two EMA- $h$  models, which take into account the finite thermal interface conductances, are able to fit the experiment data



when the  $h$  is used as a fitting parameter. Amendments to HJ-ME by Minnich et al.<sup>17</sup> include reduced phonon mean free paths, do not improve upon the fit since  $k_{\text{NCA}}$  is insensitive to the core thermal conductivity (Figure 2.6a).

Although the EMA- $h$  models can be fit to match the experimental trend, several questions about their application to NCAs include:

- i) The matrix phase thermal conductivity is a critical input to all the EMA models. In the NCAs, all the ligand species are anchored covalently to the inorganic cores, creating structure that is otherwise absent in bulk (e.g., oleic acid ligands form solid PbS NCAs, but is a liquid phase in isolation). Although we have considered a structurally and chemically similar solid film to get a representative thermal conductivity in our EMA analysis, the molecules in this film are still randomly orientated. Alternatively, the bulk thermal conductivities of the liquid phase can be used to predict the NCA thermal conductivity and the results are plotted in Appendix A Figure A1. For liquid oleic acid, its 300 K thermal conductivity was measured to be 0.23 W/m-K (ref. [76]). Using this value, both EMA- $h$  models yield a much smaller  $h$  (44 MW/m<sup>2</sup>K from the HJ-ME model) and a worse fit (compare Figure 2.6b with Appendix A Figure A1).
- ii) EMA models assume a continuous matrix phase. This assumption may not be an accurate description of the structure of a NCA. The ligands in NCAs have some order and there may be empty spaces within the close-packed NCA structure, especially for the larger core NCAs.

Notwithstanding, the results from the EMA- $h$  models support our proposition that the thermal conductivity of the NCA film is mitigated by ligand-core and ligand-ligand interfaces. Without considering the  $h$ , conventional EMA models cannot accurately

describe the thermal conductivity of the NCA diameter series.

The representative temperature profile obtained in our simulations is shown in Figure 2.3. All the temperature drops occur across the ligand junctions between the isothermal cores. This behavior supports our experimental conclusion that thermal transport is ligand mediated and influenced by  $h$ .

#### **2.4.5 Temperature-dependent Thermal Conductivity and Interfacial Thermal Conductance**

The EMA analysis points to  $h$  as a crucial factor in explaining  $k_{NCA}$  and temperature-dependent measurements of  $k_{NCA}$  can provide additional insight. The thermal conductivities of PbS, PbSe, PbTe, and CdSe NCAs increase from 10 to 200 K and plateau above 200 K, as shown in Figures 2.7a and 2.7b. This behavior suggests that interfacial vibrational energy transport at the measured temperatures is dominated by elastic events, whereby the frequencies of the interacting states are the same, and can be understood by considering the vDOS.

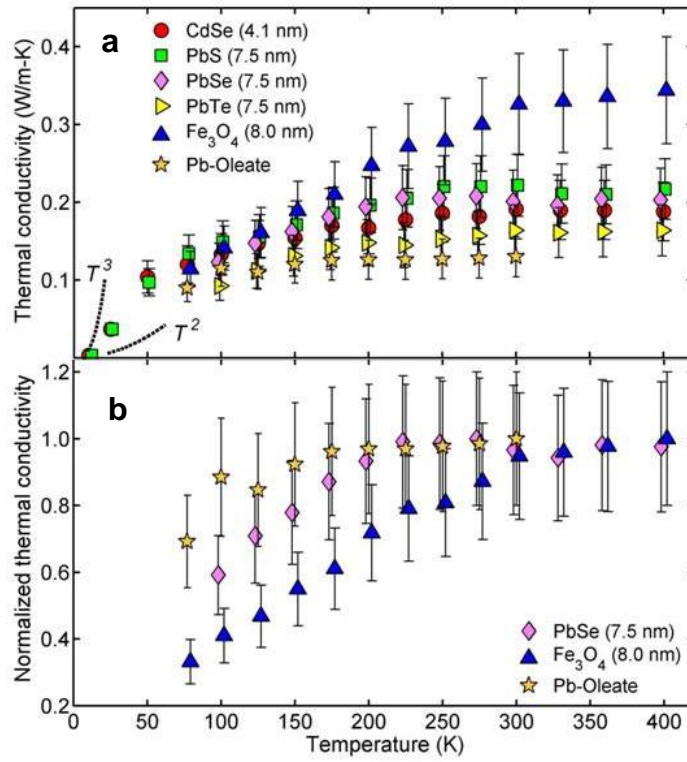


**Figure 2.7 Effects of temperature on thermal conductivity.** **a**, Temperature series for CdSe (diameter = 4.1 nm,  $\theta_{D,CdSe} = 182$  K; ref. [79]), PbS (diameter = 7.5 nm,  $\theta_{D,PbS} = 225$  K; ref. [80]), PbSe (diameter = 7.5 nm,  $\theta_{D,PbSe} = 175$  K; ref. [80]), PbTe (diameter = 7.5 nm,  $\theta_{D,PbTe} = 136$  K; ref. [80]) and Fe<sub>3</sub>O<sub>4</sub> (diameter = 8.0 nm,  $\theta_{D,Fe_3O_4} > 350$  K; ref. [81]) NCAs, and Pb-oleate ligands. The points have been slightly offset in temperature so errorbars can be resolved.  $T^2$  and  $T^3$  scalings are included for reference. **b**, Normalized temperature series for Pb-oleate ligands and PbSe and Fe<sub>3</sub>O<sub>4</sub> NCAs (with the respect to their maximum thermal conductivity) plateau above 150 K for Pb-oleate, 200 K for PbSe and 300 K for Fe<sub>3</sub>O<sub>4</sub> NCA.

Below a temperature of 200 K, which is near the Debye temperatures ( $\theta_D$ ) of CdSe, PbS, PbSe and PbTe ( $\theta_{D,CdSe} = 182$  K, ref. [79];  $\theta_{D,PbS} = 225$  K,  $\theta_{D,PbSe} = 175$  K,  $\theta_{D,PbTe} = 136$  K, ref. [80]) increasing the temperature increases the populations of vibrational states with frequencies that are common to the cores and ligands. When the

temperature increases beyond the core  $\theta_D$ , the vibrational frequencies common to the cores and ligands are fully activated. Additional higher-frequency ligand states continue to be activated (see Figure 2.4) but as these ligand states do not have core states to couple with elastically, the thermal conductivity plateaus. To test this hypothesis, we fit the thermal conductivity temperature series (77 K to 300 K; Pb-oleate melts slightly above 300 K) of PbSe (core diameter of 6.4 nm and 7.5 nm) and Fe<sub>3</sub>O<sub>4</sub> (core diameter of 5 nm and 8 nm) to the HJ-ME model to extract  $h$  at each temperature. The result is plotted in Figure 2.8. These two NCA types are chosen as they have a large difference in Debye temperature ( $\theta_{D,PbSe} = 175$  K, ref. [80] and  $\theta_{D,Fe_3O_4} > 350$  K, ref. [81]).

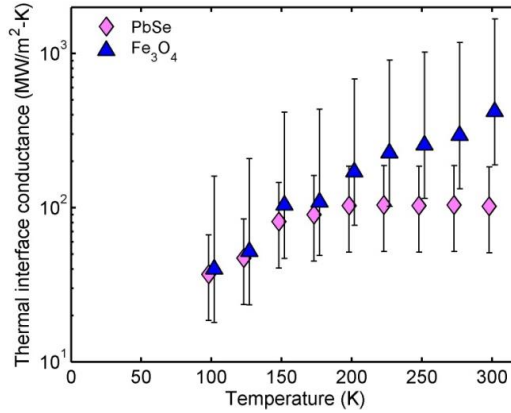


**Figure 2.8** Fitted  $h$  using HJ-ME for PbSe and Fe<sub>3</sub>O<sub>4</sub> NCAs.

PbSe NCAs display a thermal conductance plateau after 200 K while Fe<sub>3</sub>O<sub>4</sub> NCA has an increasing thermal conductance – an observation consistent with our thermal conductivity measurements in Figures 2.7a and 2.7b. The shape of the temperature-dependent thermal conductance in the PbSe NCA is consistent with the experimental data for a self-assembled monolayer (SAM) found in the Luo et al. (ref. [66]). The

appearance of the thermal conductance plateau is supportive of elastic phonon scattering at the core-ligand interface in NCAs. If inelastic events were present at the interface, then the thermal conductance would continue to increase with increasing temperature [82]. In addition, comparison of these two thermal conductance trends in Figure 2.8 supports the postulation where the core vDOS influences the thermal conductance of the core-ligand interface and the thermal conductivity of the NCA. The critical role of the interface in the temperature dependence is also confirmed by the thermal conductivity of Pb-oleate (oleate is the ligand in the  $\text{Fe}_3\text{O}_4$ , PbS, PbSe, and PbTe NCAs), which shows a weaker temperature dependence and an earlier plateau temperature than the NCAs.

It is important, however, to be cautious in using the absolute values of these thermal interface conductance as changing the EMA-h model (e.g., from HJ-ME to Minnich) produces different values of  $h$ . Further, this method has large uncertainty which propagates from the uncertainty in the measured thermal conductivity of the NCAs and Pb-oleate. Nonetheless, the trend of the fitted  $h$  is supportive of two postulations:

- i. Elastic scattering dominates across the interfaces in NCAs.
- ii. The core vDOS influences the thermal conductance of the core-ligand interface and the thermal conductivity of the NCA.

We also observe that the thermal conductivity scales as  $T^\alpha$  below a temperature of 50 K, where  $2 < \alpha < 3$ , a scaling that requires further investigation.

#### **2.4.6 Core-ligand Chemistry-dependent Thermal Conductivity**

Core-ligand chemistry defines the electronic properties of NCAs [2]. For example, the electronic conductivity of a PbSe NCA recorded a ten order of magnitude increase

by exchanging the oleic acid ligands with shorter hydrazine molecules [2,7]. To test whether thermal transport parallels charge transport, core and ligand chemistries were systematically changed. Lead chalcogenide (PbS, PbSe, and PbTe cores, all 7.5 nm in diameter) NCAs were chosen to isolate the core species effect as they can be prepared with the same oleate ligand group. Both experimental and MD thermal conductivity results are plotted in Figure 2.9a versus the mass ratio of the core species (species average) and the methylene group ( $\text{CH}_2$ ) of the ligand. A decreasing thermal conductivity with increasing mass ratio is observed in experiments and substantiated by our simulation predictions. This result corresponds to a decreasing thermal conductivity with decreasing  $\theta_D$  (i.e., heavier core species). The 30% reduction for PbS vs. PbTe NCAs cannot be solely explained by the reduced bulk thermal conductivity of PbS vs. PbTe, which amounts to only a 5% change in  $k_{NCA}$  (based on HJ-ME) [59]. Additionally, lower  $\theta_D$  identifies a shift of core phonons to lower-frequency states having less overlap with the high-frequency ligand states. Theory suggests that this misalignment will reduce  $h$  [83] and based on  $k_{NCA}$  data, HJ-ME indicates that  $h$  is reduced from  $140^{+170}_{-80}$  MW/m<sup>2</sup>-K for PbS to  $72^{+57}_{-34}$  MW/m<sup>2</sup>-K for PbTe NCAs.

The role of ligand chemistry in NCA thermal transport was elucidated by exchanging the long organic ligands with short inorganic ligands ( $\text{N}_2\text{H}_4$ ,  $\text{AsS}_3^{3-}$ ,  $\text{In}_2\text{Se}_4^{2-}$ ) on PbS and CdSe NCs originally capped with oleate and n-tetradecylphosphonate ligands, respectively. The thermal conductivities increased by 50% after the ligand exchange, as shown in Figure 2.9b. NCAs with long organic ligands are electrically-insulating, inhibiting electrons as potential heat carriers. NCAs with short inorganic

ligands, however, have such a small inter-core separation that electronic coupling between neighboring nanocrystals has been reported [56].

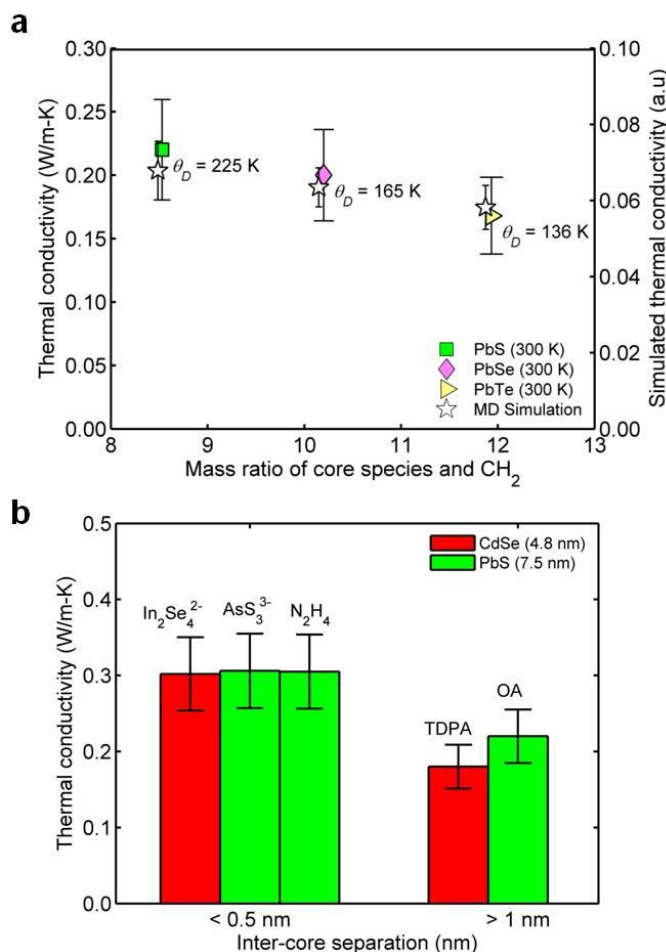


**Figure 2.9 Effects of NCA chemistry on thermal conductivity.** **a**, Oleate-capped lead chalcogenide NCAs show a decrease in thermal conductivity with larger mass ratio, i.e., smaller core Debye temperature  $\theta_D$  ( $\theta_D$  from ref. [80]). The MD simulation data are displaced horizontally for clarity. **b**, NCA thermal conductivity for different inorganic (In<sub>2</sub>Se<sub>4</sub><sup>2-</sup>, AsS<sub>3</sub><sup>3-</sup>, N<sub>2</sub>H<sub>4</sub>) and organic ligands [tetradecylphosphonic acid (TDPA) and oleic acid (OA)] on CdSe and PbS NCs. Shorter inorganic ligands increase the thermal conductivity by 50% relative to organic ligands.

Using the Wiedemann-Franz law for PbSe-N<sub>2</sub>H<sub>4</sub> and CdSe-In<sub>2</sub>Se<sub>4</sub><sup>2-</sup> NCAs [56,84] , we estimate the electronic thermal conductivities of  $6.2 \times 10^{-3} \text{ W m}^{-1} \text{ K}^{-1}$  and  $2.7 \times 10^{-2} \text{ W m}^{-1} \text{ K}^{-1}$  based on their electrical conductivities. These estimates are at least an order of magnitude smaller than our measured values, verifying that electronic contributions to  $k_{NCA}$  are negligible.

Despite higher interface density and absent electronic contributions, several explanations for increased  $k_{NCA}$  in Figure 2.9b may be at play within the framework of HJ-ME. Using PbS nanocrystals capped with N<sub>2</sub>H<sub>4</sub> or oleate ligands as an example, the shorter N<sub>2</sub>H<sub>4</sub> ligands have a higher bulk thermal conductivity [85] than oleic acid [76]. Contraction of the NCA structure due to shorter ligands increases the core volume fraction for PbS core (7.5 nm) from 0.43 to 0.61, which alone increases the HJ-ME prediction from 0.22 to 0.28 W/m-K. Finally, the value of  $h$  may increase due to improved alignment of the core-ligand vibrational states resulting from heavier ligand atoms.

## 2.5 Conclusion

In summary, we have shown that the NCA thermal conductivity is mitigated by the overlap and coupling of the core and ligand vibrational states and the volume fractions of the constituents. Based on our measurements, the temperature gradient within a NCA-based light emitting diode active region or field-effect transistor will be 100 - 1000 times higher than in commercial devices that use Si or other single-crystal semiconductors, posing additional requirements for thermal management and electronics packaging. Nevertheless, exchanging the long organic ligands with shorter



inorganic ligands increases the electrical conductivity by many orders of magnitude<sup>5</sup> with an accompanied increase of only 50% in thermal conductivity. This decoupling of the thermal and electronic properties evokes hope for solution-processible NCA-based thermoelectrics.

## CHAPTER 3

### **Coupling of Organic and Inorganic Vibrational States and Their Thermal Transport in Nanocrystal Arrays**

#### **3.1 Overview**

Through atomistic computational analysis of thermal transport in nanocrystal arrays (NCAs), the vibrational states were found to couple elastically across the organic-inorganic interfaces with a resulting flux that depends on the ligand grafting density and the overlap between the core and ligand vibrational spectra. The modeling was performed using molecular dynamics simulations and lattice dynamics calculations on a gold-dodecanethiol NCA built using a robust self-assembly methodology. The predicted NCA thermal conductivities was validated against experimental measurements (as reported in Chapter 2) with agreement found in both magnitude and trends. The self-assembly methodology enables prediction of general NCA behavior and detailed probing of experimentally inaccessible nanoscale phenomena [86]. [Published in “Coupling of Organic and Inorganic Vibrational States and Their Thermal Transport in Nanocrystal Arrays”, W-L. Ong, S. Majumdar, J.A. Malen, A.J.H. McGaughey, *J. of Phys. Chem. C* **118** (14), 7288-7295.]

## 3.2 Introduction

In Chapter 2, the first-ever experimental measurements of NCA thermal conductivity was reported, studying the effects of the core diameter, and the core and ligand compositions [55]. In that work, molecular dynamics (MD) simulations were performed using a rudimentary NCA model built by placing simplified nanocrystal motifs into a linear chain. Each motif was comprised of a multi-atom spherical core and six ligands (equally-spaced and oriented along the three Cartesian directions) that weakly interacted with its nearest neighbors. Together with simple inter- and intra-molecular potentials (which hereafter referred as potentials), those MD simulations resulted in thermal conductivity predictions that qualitatively captured the measured trends but not their magnitudes. This single NCA thermal transport study stands in contrast to a collection of experimental measurements [26,27,32,58,87,88] and computational predictions [23,28,89,90] performed on SAMs. Specialized synthesis techniques and the challenges of thermal conductivity metrology hinder experimental investigations of NCAs [55], while the need for a large number of atoms (30,000 to 500,000) [91] and the lack of a good methodology to form a full-scale NCA model impedes simulation.

In our experiments [55], we found that surface chemistry mediates thermal transport in NCAs by controlling the interfacial thermal conductance between the ligands and the core. What remains unknown is how this interfacial thermal conductance, which cannot be directly measured experimentally, will change with various NCA design parameters. Questions include: Will this interfacial thermal conductance be equivalent

to that of a SAM with identical species? Will the interfacial thermal conductance change with nanocrystal diameter, and if so, how? How will the mass of the core atoms affect the interfacial thermal conductance? Another important experimental finding is a thermal conductivity plateau at temperatures higher than the core Debye temperature. This result suggests that elastic rather than inelastic vibrational scattering dominates at the interfaces, a hypothesis that requires testing.

In this chapter, the above questions, which cannot be readily answered experimentally, are investigated using MD simulations and lattice dynamics calculations. Using existing simulation and experimental observations, a methodical way to build an NCA model is formulated for use in MD-based predictions of thermal conductivity and interfacial thermal conductance. The thermal conductivity predictions are assessed by comparing with existing experimental thermal conductivity measurements and interpreted using effective medium approximations (EMAs) [55,77]. Through these studies, a scaling law for predicting the interfacial thermal conductance is proposed and a computationally inexpensive framework for estimating NCA thermal conductivity. In addition, we provide strong evidence for the presence of elastic vibrational scattering at the interfaces in an NCA.

### **3.3 Methods**

We focus on gold-dodecanethiol (Au core-C<sub>12</sub>H<sub>25</sub>SH ligand) NCAs as our case study. This selection is motivated by the availability of experimental thermal conductivity measurements [55] and well-characterized potentials for modeling the NCA species interactions [66,92].

The ability of MD simulations to mimic and predict the behavior of real systems hinges on the appropriate choice of potentials and building a physically-realistic simulation structure. Details on the potentials used can be found in the Appendix B Section I and Table B1. The MD simulations were performed using LAMMPS [62] with a time-step of 1 fs. The ligand vibrational density of states was obtained using harmonic lattice dynamics calculations in GULP [70] and the density of states for the nanoparticles was obtained using the velocity autocorrelation function from MD simulations.

Previous computational work has addressed the interactions between a few nanocrystals and specifically the role of the ligands and the solvent species [91,93–96]. To date, only four studies have created full-scale NCAs [91,95,97,98]. Luedtke and Landman [95] used gold cores of 140 atoms (diameter < 2 nm) to study how the NCA assembly is influenced by factors including ligand length and temperature. They found that dodecanethiol-grafted gold nanocrystals form a distorted face centered cubic (FCC) structure at a temperature of 300 K. Kaushik and Clancy [91] studied how the NCA packing structure changed with different solvents. In their model, alkane ligands were pre-attached using a carbon-lead bond at a grafting density of 3 ligands/nm<sup>2</sup> onto hollow-core lead selenide nanocrystals that were explicitly surrounded with solvent molecules. The nanocrystals packed into a FCC structure when the ligand length-to-core diameter ratio was below unity. Recently, Zanjani and Lukes [97,98] assembled a CdSe-hexylthiol NCA to predict its elastic properties and later its thermal properties. In their approach, ligands are attached one-by-one to the surface cadmium atoms to create the nanocrystals.

All MD simulations were performed using LAMMPS with a time step of 1 fs. Periodic boundary conditions in the three Cartesian directions were implemented in all simulations except during the determination of NCA thermal conductivity, where nanocrystals are fixed along the two boundaries in the direction of heat flow (Figure 3.1e).

To build a full-scale NCA, it is imperative to start by forming a nanocrystal building block. First, a core ranging from 55 to 3925 atoms was carved from a bulk gold FCC lattice (as-cut diameters of 0.9, 1.6, 1.8, 3.0, 4.0, and 5.0 nm). For the smallest three diameters, the core is not spherical but rather octahedral or tetrahedral in shape due to the small number of atoms. We did not use the hollow-core approach of Kaushik and Clancy, [91] as all atoms are required to capture the full spectrum of thermal vibrations. To save computational time, we did not consider the effect of the surrounding solvent molecules on the packing structure, as most experimental NCAs have the FCC structure [2]. In analogy to the colloidal synthesis, the gold core was then surrounded by excess dodecanethiol molecules (Figure 3.1a) and thermalized at a temperature of 300 K using velocity rescaling for 1 ns and subsequently relaxed under a microcanonical ensemble (i.e., constant mass, volume, and total energy) for an additional 5 ns. During this process, the ligands explored the core potential energy surface and encapsulated the whole core in a monolayer (Figure 3.1b). The sulfur atom of each ligand was trapped slightly above the hollow sites (2-fold, 3-fold, and 4-fold) between the surface gold atoms of the core – an observation consistent with earlier experimental and computational findings [99,100]. At some positions, the sulfur atoms embedded into the core. Our approach differs from that of Luedtke and Landman, [95] where

butanethiol molecules were lengthened to dodecanethiol after the attachment process. Longer dodecanethiol ligands might cause steric hindrances during ligand attachment that would result in a different topological arrangement on the core surface. Unattached ligands were then filtered and the ligand-passivated nanocrystal was duplicated and stacked in the [111] direction to form an open 3x2x2 FCC unit cell (Figure 3.1c). Subsequently, the nanocrystals in this unit cell were induced to close pack into a minimal energy configuration under an isothermal-isobaric ensemble at a temperature and pressure of 300 K and 0 bar using a Nose-Hoover thermostat and barostat for 5 – 10 ns (Figure 3.1d). This close-packed structure was then tiled to obtain the desired NCA thickness (9 – 90 nm) for thermal conductivity predictions (Figure 3.1e).

The NCA thermal conductivity ( $k_{NCA}$ ) is predicted using the direct method under non-equilibrium molecular dynamics (NEMD) simulation.[101] NCAs of desired thickness (10 to 90 nm, requiring between 30,000 to 300,000 atoms) were thermalized at a temperature of 300 K for 1 ns using velocity rescaling and equilibrated for a further 1 ns under the microcanonical ensemble before the start of the direct method. By randomizing the initial velocity for each atom, any artificial periodicity in the NCA created during the duplication and stacking of the unit cell is removed. During the direct method simulations, a heat flow was induced through the NCA by sourcing and sinking a predetermined amount of heat ( $\vec{q}$  ranging from 0.075 to 0.31 eV/ps) at the source and sink regions (Figure 3.1e) for a total time of 20 – 40 ns. Only the cores were used to source and sink heat as a few (5 to 8) ligands can dislodge and bond to other

cores during the simulations. The targeted steady state temperature difference between region  $L_1$  and  $L_n$  is  $30 \pm 10$  K (i.e., 10 % of average simulation temperature). The thicker the NCA, the longer it takes to reach steady-state – a condition determined by comparing the time-averaged temperature profile after each nanosecond. A layer's (as depicted in Figure 3.1e) temperature is obtained by averaging all core temperatures in that layer (core-to-core temperature variation  $< 1$  %). The resulting steady-state temperature gradient ( $\frac{dT}{dx}$ ) between region  $L_1$  and  $L_n$ , obtained by averaging blocks of 1 ns for a total duration of 10 ns, was used in the Fourier law ( $\vec{q} = -k_{NCA} A \frac{dT}{dx}$ , where  $A$  is the area perpendicular to the heat flow) to obtain the thermal conductivity.

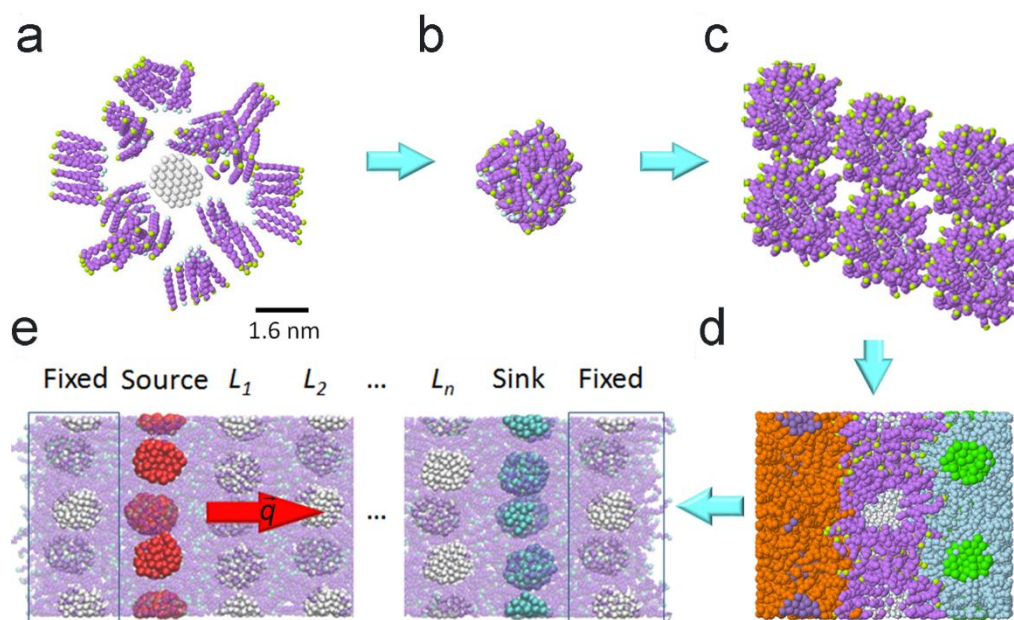


**Figure 3.1. Building an NCA with 1.6 nm diameter cores.** **a**, Gold core surrounded with excess ligands. Scale bar applies to all sub-figures. **b**, Ligands redistribute and attach across the core surface. **c**, After filtering excess ligands, nanocrystals are stacked to form an open FCC 3x2x2 unit cell. **d**, After relaxation, a close-packed structure



forms. Different layers in the stack are distinguished by their colors. **e**, Using this relaxed unit cell, different NCA thicknesses can be formed by tiling. The non-equilibrium MD direct method for predicting thermal conductivity is performed on an n-layer NCA array bounded by heat source, heat sink, and fixed regions. The ligands are translucent here so that the cores are visible.

## 3.4 Result and Discussion

### 3.4.1 Validation of Model

We first determined the cross-sectional area required to get converged thermal conductivity predictions. Using an NCA of 9 nm in thickness built from cores of 1.6 nm in diameter, thermal conductivity predictions were made using three progressively larger cross-sectional areas. As shown in Table 3.1, all systems predict a value approximately at 0.16 W/m-K, indicating the suitability of the smallest model (i.e., cross-sectional area of 32.86 nm<sup>2</sup>, 2 x 2 nanocrystals). The 2 x 2 nanocrystal cross section is used for all diameters.

**Table 3.1 Simulated NCA thermal conductivity for cross-sectional area convergence for 1.6 nm diameter nanocrystals.**

Cross-sectional Area (nm <sup>2</sup> )	Thermal conductivity (W/m-K)
32.85	0.166
65.71	0.159
131.43	0.163

We validate our full-scale NCA model by comparing the thickness- and core diameter-dependence of thermal conductivity with experimental measurements [55]. For the thickness series, thermal conductivities of NCAs built using cores of 1.6 nm and 4.0 nm in diameter were predicted for thicknesses between 9 and 90 nm. The results are plotted alongside experimental measurements for a 4.5 nm core gold NCA of similar film thicknesses in Figure 3.2. As shown in Figure 3.2, the full-scale NCA model captures both the magnitude and trend of the experimental measurements with respect to the film thickness. Both simulation and experiment show a thickness-invariant thermal conductivity with similar magnitudes. This invariance indicates diffusive thermal transport in the NCAs with scattering from the boundaries playing a negligible role [55].

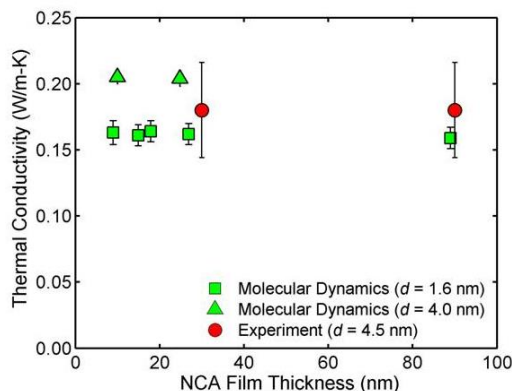


**Figure 3.2 Predicted thermal conductivities and corresponding experimental measurements [55] of varying the NCA thickness.**

Given the thickness-invariance of the thermal conductivity, the diameter series was performed using the minimum number of layers (three) required to establish a steady-

state temperature gradient during the direct method simulation. The thermal conductivity predictions for six different core diameters and the single 4.5 nm gold core experimental point are plotted in Figure 3.4b. The simulations show an increasing thermal conductivity trend when the diameter is larger than 2 nm, capturing the upward experimental trend we measured for PbS, PbSe, PbTe, CdSe, and Fe<sub>3</sub>O<sub>4</sub> NCAs [55]. In addition, the predicted magnitude for a diameter of 4.5 nm is within the uncertainty of the corresponding experimental measurement. It is thus evident that the full-scale NCA model captures both the magnitude and trend of the existing experimental measurements well, giving confidence to the chosen potentials and their extension to future predictions [27,58].

### 3.4.2 Diameter-dependent Ligand Footprint

The average area occupied by a ligand grafted on a surface,  $\sigma$ , is termed the ligand footprint [102] and is the reciprocal of the grafting density. The footprint of an optimally-grafted alkanethiol SAM on a flat gold surface,  $\sigma_{SAM}$ , is  $21.6 \pm 0.2 \text{ \AA}^2/\text{ligand}$  [103,104]. Experimental [105] and simulation [102] results, however, suggest that alkanethiols are more closely packed on curved nanocrystal cores, giving a lower footprint at smaller core diameters. Our prior study [55] found that the thermal conductivity of an NCA depends on the diameter,  $d$ , of its constituent nanocrystals. A natural question is whether the ligand grafting density (i.e., the number of ligands per unit surface area,  $\frac{1}{\sigma}$ ) influences NCA thermal conductivity.

In a prior simulation study [102], Jimenez *et al.* found the optimal footprint by

changing the surface area required for a predetermined number of ligands to get a net-zero surface pressure across the nanocrystal surface. Our alternative approach of forming an optimally-grafted nanocrystal allows the ligands to naturally explore the potential energy surface on a core. Our diameter-dependent footprints,  $\sigma_d$ , are plotted in Figure 3.3, normalized by the footprint value for a SAM. The data agree with the geometry-based analytical model of Jimenez *et al.* [102],

$$\frac{\sigma_d}{\sigma_{SAM}} = \frac{1}{1 + \frac{2c}{d}}, \quad (3.1)$$

giving a fitted  $c$  value of 0.76 nm, which is comparable with the 0.8 nm obtained in the original study. The bigger footprint for the larger cores implies a smaller grafting density due to increased steric hindrance from smaller surface curvature. At the largest nanocrystal diameter of 5 nm, the footprint is 71% of that for the SAM.

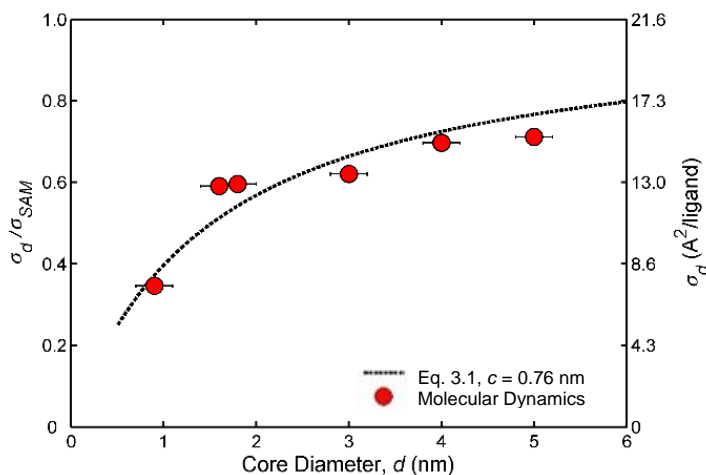


**Figure 3.3 Diameter-dependent footprint of dodecanethiol ligands on a gold core.** The MD-predicted footprints agree well with predictions from equation 3.1 (dotted line) [102]. The  $R^2$  value of the fit is 0.86. See Appendix B Section V for discussion of error bars.

### 3.4.3 Core Diameter Series

In simple EMA formulations, the effective thermal conductivity of a composite material is a function of the volume fractions ( $v_p$ ,  $v_m$ ) and bulk thermal conductivities ( $k_p$ ,  $k_m$ ) of the solid particle and matrix phases [73]. By including a finite interfacial thermal conductance,  $h$  (which is a per unit area quantity), between the particle and matrix phases, the resulting formulations have been found to better match experimental measurements for some composites [77,106]. The Hasselman-Johnson EMA- $h$  model for spherical inclusions is

$$k_{EMA-h} = k_m \frac{k_p (1 + 2\alpha) + 2k_m + 2v_p [k_p (1 - \alpha) - k_m]}{k_p (1 + 2\alpha) + 2k_m - v_p [k_p (1 - \alpha) - k_m]} , \quad (3.2)$$

where  $\alpha = \frac{k_m / h}{\frac{d}{2}}$ . Here,  $\alpha$  can be viewed as a ratio between the matrix Kapitza

length and the particle diameter. When the diameter is smaller than or similar in magnitude to the Kapitza length, the interfacial thermal conductance becomes important in determining the composite thermal conductivity. On the other hand, when the diameter is much bigger than the Kapitza length,  $\alpha$  tends to zero and equation 3.2 simplifies to an EMA formulation that has no dependence on the interfacial thermal conductance [77].

In our previous study [55], the experimentally-measured thermal conductivities of PbS NCAs with diameters greater than 3.5 nm agree with the predictions of equation 3.2 when the interfacial thermal conductance between the core and ligands is used as a

fitting parameter. We now use this EMA-*h* model to interpret our simulation predictions. Our MD-based approach allows us to specify all unknown inputs to the EMA-*h* formulation in a self-consistent manner, thus requiring no approximations or fitting parameters.

To evaluate equation 3.2, we require the bulk solid thermal conductivities and volume fractions of the particle (i.e., gold core) and the matrix (i.e., dodecanethiol ligands) phases, and the interfacial thermal conductance between the particle and the matrix (see schematic diagram in inset in Figure 3.4b). The volume fraction is determined from the NCA geometry. The bulk solid thermal conductivity of the core is obtained by applying the direct method to a block of FCC gold atoms at an average temperature of 300 K with heat flow in the [111] direction. The resulting thermal conductivity is  $1.8 \pm 0.3$  W/m-K (details in Appendix B Section II). This small thermal conductivity of gold compared to its textbook value is due to the absence of electrons in MD simulations. The assumption of neglecting electrons in our model is supported by the negligible electronic contribution to thermal transport in NCAs with dielectric ligands longer than 0.5 nm (the dodecanethiol molecule is 1.5 nm long) [2,55]. The thermal conductivity of the ligand solid is obtained using the direct method on a solid block of amorphous dodecanethiol ligands at an average temperature of 300 K, to extract a value of  $0.15 \pm 0.01$  W/m-K (details in Appendix B Section III).

The last component of the EMA-*h* model is the interfacial thermal conductance. This value is obtained by imposing a heat flow on 10% of the gold atoms located in the heart of a central core that is surrounded by 34 other cores to form a FCC NCA cuboid with periodic boundary conditions. This arrangement allows heat to flow radially

outward from the central core to the surrounding cores, which act as heat sinks. Ligands attached to the central core can be assumed to be isothermal internally and with one another due to the short chain length, strong carbon-carbon bonds [107,108], and geometric symmetry of the radial heat flow. The interfacial thermal conductance is obtained by dividing the imposed heat flow by the core surface area and the average temperature difference between the unheated atoms in the central core and the attached ligands. The temperature difference in these simulations is  $15 \pm 5$  K.

The predicted interfacial thermal conductance varies with the core diameter, as seen in Figure 3.4a. The grafting density, plotted in Figure 3.3, also changes with diameter. We thus postulate that the thermal energy crossing the inorganic-organic interfaces depends on the number of ligands grafted per unit area on the core. By assuming that the interfacial thermal conductance scales proportionally to the grafting density, a scaling model was derived from equation 3.1,

$$\frac{h}{h_{SAM/gold}} = 1 + \frac{2c}{d} \quad . \quad (3.3)$$

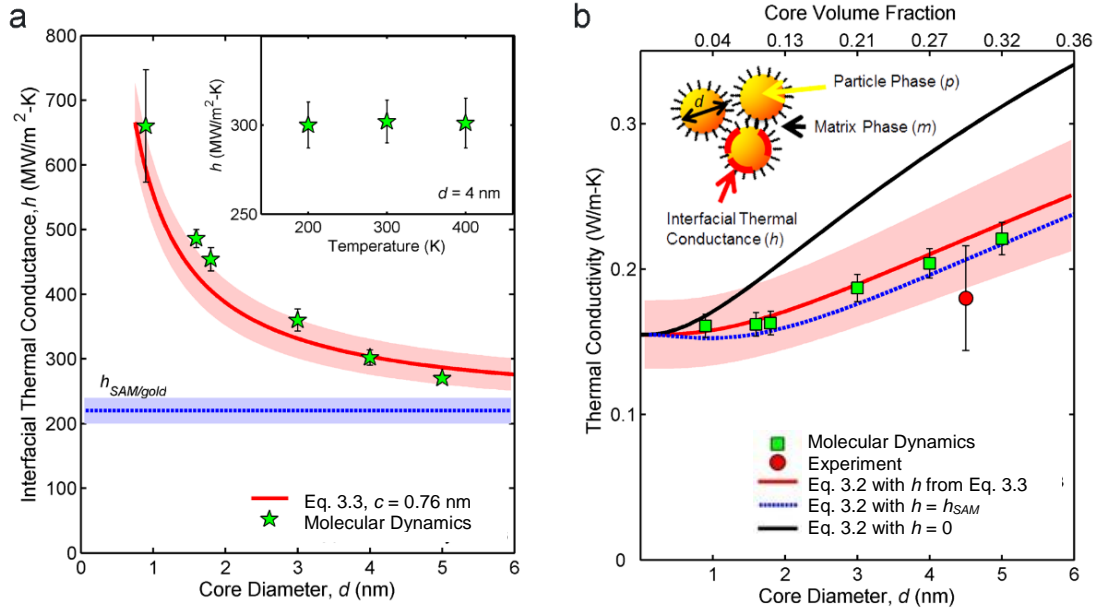


**Figure 3.4 EMA investigation for diameter series.** **a**, Interfacial thermal conductance from the FCC NCA cuboid scales according to equation 3.3, where  $h_{SAM/gold}$  is the predicted SAM thermal conductance and  $c = 0.76$  nm is obtained from the footprint scaling law (Figure 3.3). The red shaded region depicts the uncertainty in the  $h_{SAM/gold}$  value (see Appendix B section V). The value of  $h_{SAM/gold}$  is plotted as a blue dotted line with its associated uncertainty (blue shaded area). Inset: Interfacial thermal conductance shows no temperature-dependence between 200 to 400 K, indicating a dominance of elastic scattering between the core and ligands. **b**, MD diameter series is well-described by EMA- $h$  using the interfacial thermal conductance values calculated from equation 3.2. The red shaded region marks the uncertainty range associated with the EMA- $h$  model due to the uncertainties in the inputs to equation 3.2. The EMA- $h$  trend calculated using  $h_{SAM/gold}$  underestimates the simulated diameter series by at most 10%. Note that the top axis is non-linear. The inset identifies the different inputs to the EMA- $h$  formulation, equation 3.2.

Using  $c = 0.76$  nm (as obtained from Figure 3.3) and  $h_{SAM/gold} = 220 \pm 20$  MW/m<sup>2</sup>K (the predicted interfacial thermal conductance of a dodecanethiol SAM on a flat Au



surface, see Appendix B Section IV), we plot equation 3.3 in Figure 3.4a. The good agreement between the raw MD data and equation 3.3 indicates that the diameter-dependence of interfacial thermal conductance (which is a per unit area quantity) can be attributed to the changing ligand grafting density that results from steric hindrance. A smaller core has a larger grafting density, allowing for increased thermal transport per unit area. The agreement between equation 3.3 and the simulation data also indicates that the interfacial thermal conductance per ligand is independent of core diameter. The per ligand interfacial thermal conductance calculated from the different diameter cores fluctuates between 42 and 62 pW/K, while the SAM/gold interface has a value of  $48 \pm 4$  pW/K. This scaling model provides a computationally inexpensive method for obtaining the diameter-dependence of interfacial thermal conductance for other NCA systems. Once the grafting density is known, only one further simulation is required to predict  $h_{SAM/gold}$ , which can then be used in equation 3.3. Deviations may exist at smaller diameters, where the shape of the nanocrystal core becomes irregular.

As MD is a classical technique where all vibrational states are fully activated, any temperature-related increase in the interfacial thermal conductance will be a result of inelastic scattering at the interface [82]. Inelastic scattering increases the number of pathways for heat to move across interfaces, increasing the interfacial thermal conductance and hence the overall NCA thermal conductivity. As seen from the inset in Figure 3.4a, the predicted interfacial thermal conductance for a 4.0 nm diameter core is constant between average system temperatures of 200 to 400 K. This result confirms that, in agreement with our previous assertion [55], elastic vibrational scattering at the core-ligand interfaces is responsible for the plateau in the experimentally measured NCA

thermal conductivity.

The EMA- $h$  and EMA (setting  $\alpha = 0$  in equation 3.2) predictions are plotted together with the MD thermal conductivities for the NCA diameter series in Figure 3.4b. The diameter-dependent interfacial thermal conductance values for EMA- $h$  are obtained from equation 3.3. The MD data do not agree well with the EMA predictions but match well with EMA- $h$  predictions, indicating the importance of including the interfacial thermal conductance in describing the thermal transport in an NCA. The EMA- $h$  model predicts a thermal conductivity trend with two distinct regimes: (i) diameter-independence at small core diameters ( $d < 2$  nm for this system), and (ii) monotonic increase at larger core diameters. Previous experimental measurements were only able to observe the second regime [55]. In comparison, our MD results span a larger diameter range, capturing and verifying the full EMA- $h$  prediction. We attribute the invariant thermal conductivity at small core diameters, which is close to the bulk ligand value, to the high volume fraction of the matrix phase, which forms a percolating network. The predictions of equation 3.2 using the single  $h_{SAM/gold}$  are also plotted in Figure 3.4b. This set of results is at most 10% lower than the predictions using the diameter-dependent  $h$ . This close agreement further substantiates that  $h_{SAM/gold}$  is a computationally cost-effective approximation for the interfacial thermal conductance needed to predict NCA thermal conductivity in the EMA- $h$  formulation.

#### 3.4.4 Core Mass Series

Experiments found that increasing the core Debye temperature, which is inversely proportional to the square root of atomic mass [45], increased the NCA thermal

conductivity [55]. This result was attributed to an increase in interfacial thermal conductance due to a higher number of overlapping vibrational states between the cores and ligands [55,109]. This proposition holds true only in the event of elastic vibrational scattering at the core-ligand interfaces; a condition that we validated in the previous section. To further probe the underlying transport physics, we now isolate the core mass effect by using core atoms of different atomic mass while using the same potentials for all interactions.

To create cores of different Debye temperature, we set the core atomic mass to 0.01, 0.05, 0.3, 1, 2, 4, 8, and 16 times that of gold for a core diameter of 4.0 nm. The NCA interfacial thermal conductance and thermal conductivity are plotted in Figures 3.5a and 3.5b.

The interfacial thermal conductance first increases, peaks, and then decreases as the mass multiple decreases from 16 to 0.01 (Figure 3.5a). To gain insight into this non-monotonic trend, we calculated the vibrational density of states of bulk gold and examined its overlap with the vibrational density of states of a dodecanethiol ligand (see Figure 3.5c). The number of ligand vibrational modes overlapping with the gold density of states increases as the gold mass multiple decreases from 16 to 0.01. The corresponding number of overlapping gold vibrational modes, on the other hand, remains constant ( $\pm 9\%$  about the average value) before dropping rapidly when the gold mass multiple becomes smaller than 0.3. This rapid decrease happens because the overlap occurs mostly in the low frequency region of the gold density of states, where the number of states follows a Debye-like  $\omega^2$  scaling. Based on the thermal conductance trend, we postulate that the maximum conductance exists when the density

of states on both sides are high. One should also consider the transmission coefficient and group velocity of each mode in order to fully account for the observed interfacial thermal conductance trend.

The NCA thermal conductivity shows a similar non-monotonic trend, as plotted in Figure 3.5b. The similarities between Figures 3.5a and 3.5b, together with the diameter series result, point convincingly to the importance of the interfacial thermal conductance in NCA thermal transport. We can set the upper and lower limits on the NCA thermal conductivity using equation 3.2. The upper line in Figure 3.5b is calculated using an infinite interfacial thermal conductance and a very high core thermal conductivity (1000 W/m-K). The lower line uses a zero core thermal conductivity. These two lines bound the MD predictions in Figure 3.5b. The EMA-h results in Figure 3.5b are calculated with equation 3.2 using the predicted interfacial thermal conductance and core thermal conductivity at each mass multiple and are in close agreement with the MD results.

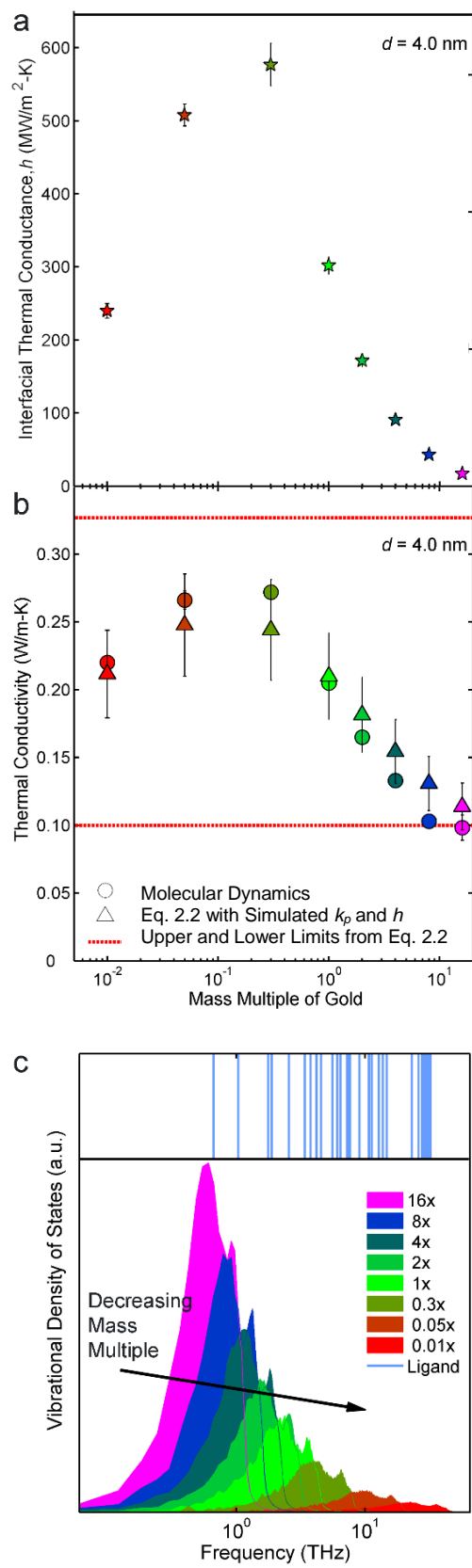


**Figure 3.5 Core mass series.** **a**, Molecular dynamics interfacial thermal conductance values for a 4.0 nm diameter core at different gold mass multiples. **b**, NCA thermal conductivity from MD simulations and the EMA- $h$  model (equation 3.2). The upper and lower limits mark the range of thermal conductivity accessible with changing mass multiple. **c**, Vibrational spectra of a dodecanethiol ligand (blue vertical lines) and 4 nm gold nanoparticles of different mass multiples.

### 3.5 Conclusion

Our computationally self-assembled gold NCA model gives thermal conductivity values and trends that agree well with experimental measurements [55]. Using this NCA model, the interfacial thermal conductance between the core and ligands was investigated – a quantity not directly measurable in experiments. We arrive at a scaling law between the interfacial thermal conductance and core diameter (equation 3.3) that clarifies the importance of curvature-dependent ligand grafting density and enables a computationally-inexpensive framework for estimating the NCA thermal conductivity diameter series. Observations of invariant interfacial thermal conductance at different system temperatures provides evidence that only elastic vibrational scattering occurs at the core-ligand interfaces. By changing the atomic mass of the core atoms while keeping the bonding environment constant, we find a non-monotonic relationship between the core atomic mass and the interfacial thermal conductance. This relationship, which propagates to the NCA thermal conductivity, can be qualitatively explained by considering the overlap between the ligand and gold density of states. While we focused on thermal transport properties, our methodology for quickly building an NCA superstructure has general utility for studying other properties of an NCA.

## CHAPTER 4

# Large Unit Cell Molecular Crystals and Their Thermal Properties

### 4.1 Overview

Large unit cell molecular crystals (LUMCs) are crystals assembled from superatoms and have lattice constants on the order of nanometers (an order of magnitude larger than atomic crystals). As weak intermolecular forces act between these superatoms, the appendage parts of a superatom can rotate or wobble in its lattice site (e.g., the alkyl groups shown in Figure 4.1 can rotate about bonded phosphorus-cobalt axis at low temperature). In certain LUMCs, extensive overlaps of the surface protruding  $\pi$ -orbitals allows electrons to move throughout the crystal, giving rise to electrical conductivity. The two-tier of periodicity in these crystals may challenge the use of conventional theories that were mainly developed for atom-based crystals.

Preliminary results for the heat capacities and thermal conductivity of nano-liter sized single crystal LUMC are discussed in this chapter. Experimental heat capacity measurements were inconclusive and the lower bounds on heat capacity were predicted using density functional theory (DFT) driven lattice dynamics calculations. The measured room temperature thermal conductivities of these LUMCs are between 0.2 to 0.4 W/mK, comparable to amorphous and nano-structured materials. The temperature dependent thermal conductivity trend of LUMCs suggests crystalline behavior, but

remains preliminary due to its dependence on the heat capacity. With the low thermal conductivity but moderate electrical conductivity, these LUMCs may be potential candidates for thermoelectric energy conversion applications.

## 4.2 Introduction

Large unit cell molecular crystals, as introduced in Chapter 1, are formed using superatoms as basic building blocks. Analogous to atoms that occupy the lattice sites in a crystal, the assembled superatoms occupy similar crystallographic sites to form a periodic solid (i.e., a superlattice) with tailored properties [1,4]. The final structure and properties of the LUMCs, as mentioned in Chapter 1, are a result of the delicate amalgamation between the various intermolecular forces (i.e., van der Waals, electrostatic, hydrogen- and halogen-bonds) and, if present, the overlap of the  $\pi$ -orbitals [49]. In the case where overlapping  $\pi$ -orbitals create a crystal-wide network, electrons can readily travel between molecular sites, giving rise to electronic properties in these crystals [49]. Similar to the nanocrystal arrays presented in Chapter 2, these newly synthesized crystals have unknown thermal conductivities but documented electronic properties [4]. I have studied both mono- and binary-species LUMCs. Examples of such LUMCs are depicted in Figure 4.1. Weak van der Waals intermolecular forces hold the superatoms together in any LUMC lattice like in the case of a  $C_{60}$  crystal. In the binary LUMCs, however, stronger electrostatic/ionic forces strengthen these intermolecular forces [4,49]. The question we set forth to understand is how thermal energy moves through these LUMCs, some of which are held together by stronger intermolecular forces than those in  $C_{60}$  crystals.



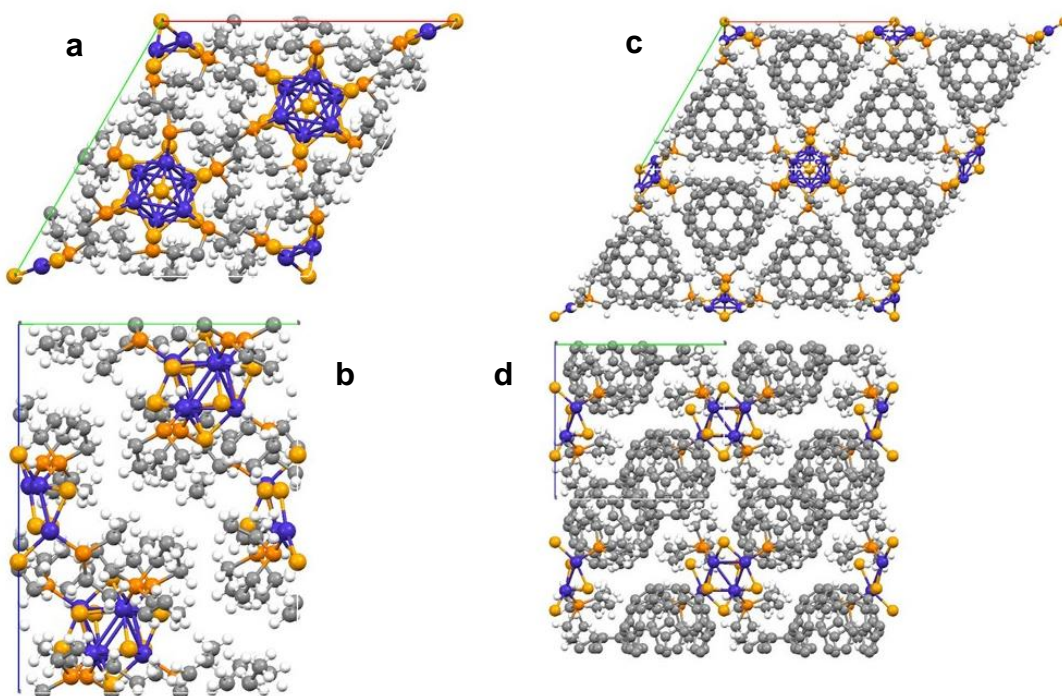


**Figure 4.1 LUMC crystal structures.** Mono-species LUMC:  $\text{Co}_6\text{Se}_8(\text{PEt}_3)_6$  structure **a**, top view (o-c direction) **b**, side view (o-b direction). Binary-species LUMC:  $\text{Co}_6\text{Se}_8(\text{PEt}_3)_6.2\text{C}_{60}$  structure **c**, top view (o-c direction) **d**, side view (o-b direction). Blue – cobalt, yellow – selenium, orange – phosphorous, gray – carbon, and white – hydrogen.

## 4.3 Methods and Materials

### 4.3.1 LUMCs

Our collaborators from Columbia University (the group that synthesized these new LUMCs last year) [4] synthesized a family of LUMCs by changing the chalcogenide groups in the mono-species LUMCs and combining them with  $\text{C}_{60}$  or  $\text{C}_{70}$  superatoms to form binary LUMCs. The samples tested are listed in the table below.

**Table 4.1 LUMCs used in thermal conductivity measurements**

Acronym	Full chemical formula	Type
CoSe	$\text{Co}_6\text{Se}_8(\text{PEt}_3)_6$	Mono
CoSe.C60	$\text{Co}_6\text{Se}_8(\text{PEt}_3)_6.2\text{C}_{60}$	Binary
CoTe	$\text{Co}_6\text{Te}_8(\text{PEt}_3)_6$	Mono
CoTe.C60	$\text{Co}_6\text{Te}_8(\text{PEt}_3)_6.2\text{C}_{60}$	Binary
CoTe.C70	$\text{Co}_6\text{Te}_8(\text{PEt}_3)_6.2\text{C}_{70}$	Binary

#### 4.3.2 FDTR Technique

The thermal conductivity of the nano-liter sized single crystal LUMCs is measured using the FDTR technique (schematic shown in Figure 4.2). Details of this technique are provided in Chapter 2. These crystals were grown on a gold-coated silicon substrate to improve crystal adhesion to the substrate although crystals can still dislodge during the course of an experiment. A layer of 60 nm of gold transducer is then coated on these crystals for the FDTR measurements. Measuring these LUMCs posed several challenges not encountered for the NCA films. Firstly, the surfaces on these crystals are generally not normal to the laser. Some are tilted at a small angle while others reflect the laser totally away from the incident path, rendering incomplete signal collection. The steady state temperature rise in the crystal induced by the lasers is not negligible because the LUMC thermal conductivity is low and these crystals are large enough to act as semi-infinite solids that retain all the deposited heat (in contrast with

the nanometer thick NCA films, where heat is easily sunk by a high thermal conductivity substrate).

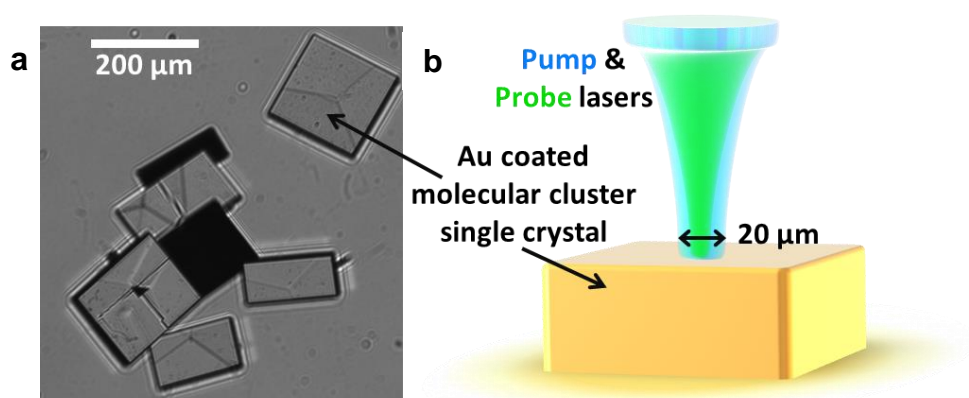


**Figure 4.2** FDTR lasers on a  $\text{Co}_6\text{Se}_8(\text{PET}_3)_6$  molecular crystal sample. **a**, Microscopic view of several crystals. The black regions are crystals with surfaces that reflect the incident light away from the incident path. The lines on the reflective crystals are the boundaries of the tilted crystal facets. **b**, Artistic depiction of the FDTR technique on the molecular crystal.

The first issue was resolved by mounting the crystals on a goniometer that adjusts the low-tilt crystal surfaces to achieve specular reflection of the lasers. The rise in the crystal's steady-state temperature was mitigated by optimizing the laser power to achieve an acceptable signal-to-noise ratio (at least 20 times) while keeping the temperature rise as low as possible. Even at the optimized laser power input, we still find a steady-state temperature rise of approximately 40 K for a crystal with a thermal conductivity of 0.2 W/mK (see details in Appendix C). The FDTR data was first fit at the experimental temperature to get an initial estimate for the LUMC thermal conductivity, which was then used to estimate the steady-state temperature rise in the

LUMC. Iterations were performed by fitting with properties at the elevated temperature to get a new thermal conductivity estimate and the steady-state temperature rise until a converged thermal conductivity and steady-state temperature rise were obtained.

### 4.3.3 Heat Capacity of LUMCs

The heat capacities of these LUMCs were measured using the differential scanning calorimetry (DSC) setup in Carnegie Mellon University (by my labmate Jillian Epstein) and Columbia University. In addition, I performed gamma-point vibrational analyses on isolated superatoms of these LUMCs using density functional theory (DFT) softwares [Vienna *Ab initio* Simulation Package (VASP) and Quantum Espresso] to get baseline heat capacity values for comparison with the experimental DSC measurements. By combining the DFT vibrational frequency spectrum with the theoretical phonon heat capacity formulation shown in equation 4.1, the heat capacity of these LUMCs can be calculated.

$$C_{lat} = \frac{k_B}{V} \sum_i \frac{x_i^2 \exp(x_i)}{[\exp(x_i) - 1]^2} \quad \text{where } x_i = \frac{\hbar \omega_i}{k_B T}, \quad (4.1)$$

where  $k_B$  is the boltzman constant,  $\omega_i$  is the vibrational frequency of phonon mode  $i$ ,  $T$  is the temperature,  $V$  is the lattice volume and  $\hbar$  is the Planck constant divided by  $2\pi$  [110].

## 4.4 Results and Discussion

### 4.4.1 Heat Capacity of LUMCs

As seen from equation 4.1, the only input required for calculating the heat capacity of a crystal lattice is its vibrational frequency spectrum. Frequencies throughout the whole Brillouin zone of a crystal can be accurately determined using DFT-based lattice dynamics and are typically needed to get good agreement with experimental measurements. A superatom in our mono-species LUMCs typically contains more than 100 atoms. Relaxing and calculating the vibrational spectrum of a single isolated superatom is computationally expensive, taking on the order of one month. I have, hence, only performed DFT vibrational calculations on single, isolated superatoms (detailed in Appendix C) from which only the frequency spectrum at the gamma-point is obtained. (i.e., at the Brillouin zone center). Vibrational calculations for multiple phononic  $k$ -points using a periodic unit cell to get the required frequencies throughout the full Brillouin zone is intractable with the computation resources available to me. The heat capacity values calculated for the different LUMCs shown in the subsequent plots can, thus, be only treated as a lower bound for the experimental results due to additive contribution from cooperative vibrational modes. Vibrational spectra for CoSe and CoTe superatoms are shown in Figures 4.3a and 4.3b.

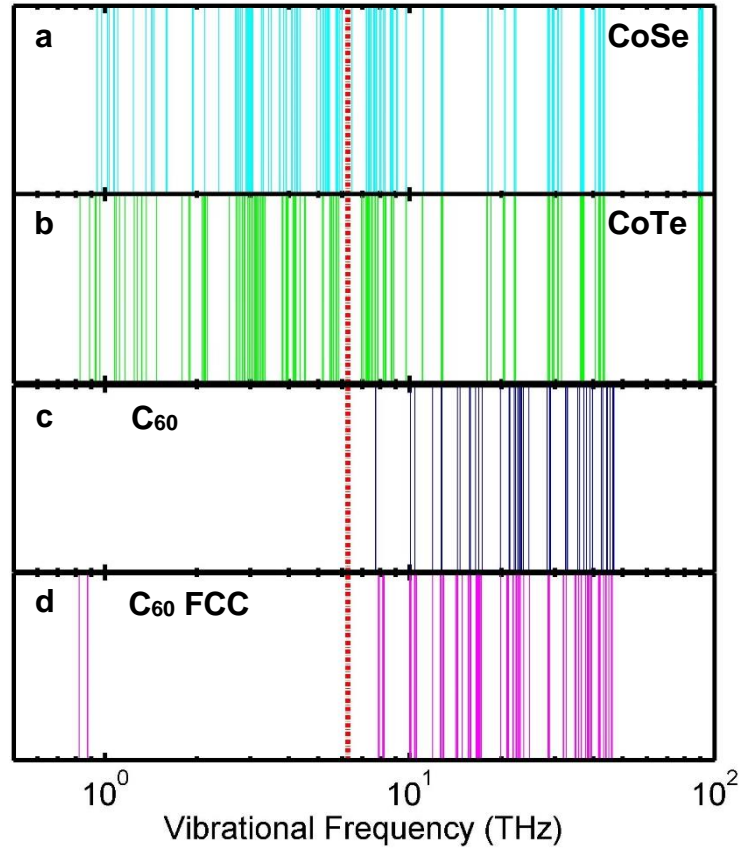


**Figure 4.3 DFT vibrational Spectra of superatoms.** **a**, An isolated CoSe. **b**, An isolated CoTe. **c**, An isolated C<sub>60</sub>. **d**, A periodic FCC C<sub>60</sub>. The vertical red dotted line represents the thermal activation frequency ( $\frac{k_B T}{h_c}$ ) at a temperature of 300 K ( $k_B$  is the Boltzmann constant and  $h_c$  is the Planck constant).

To gain a sense of the discrepancies between the actual and the calculated baseline heat capacity values, the C<sub>60</sub> superatom is used as a case study. Other than the isolated C<sub>60</sub>, I have also calculated the gamma-point vibrational spectrum of a 1x1x1 FCC C<sub>60</sub> unit cell. The vibrational spectra of an isolated C<sub>60</sub> and C<sub>60</sub> in FCC unit cell are shown in Figures 4.3c and 4.3d. The resulting baseline heat capacity values using these DFT vibrational spectra are compared with the experimental values in Figure 4.4.

The single  $C_{60}$  vibrational spectrum is almost identical with less than one percent difference at all frequencies between the DFT predictions and experimental measurements (not shown). The resulting baseline heat capacity values calculated using equation 4.1 (solid line in Figure 4.4a) are lower than the measured values as the long wavelength modes arising from the periodicity are included in the calculations. The maximum difference is below 20% of the experimental value at temperatures above 200 K but increases rapidly to about 60% at a temperature of 100 K (Figure 4.4b). The larger discrepancy at lower temperatures results from the missing low frequency (i.e., long wavelength) modes that arise from collective motion of the  $C_{60}$  superatoms. This proposition is supported by our observation of smaller discrepancies (Figure 4.4c) when the heat capacity is calculated using the vibrational spectrum of the FCC  $C_{60}$  unit cell (dotted line in Figure 4.4a) that includes frequency modes below 1 THz (Figure 4.3d). For the LUMCs under investigation, a lot more vibrational states of the isolated superatoms are populated at room temperature than in the isolated  $C_{60}$  molecule (see frequencies left of the red dotted line Figure 4.3). This larger number of populated vibrational states suggests that smaller discrepancies will exist between the calculated and actual heat capacities for these LUMCs across the temperature range.

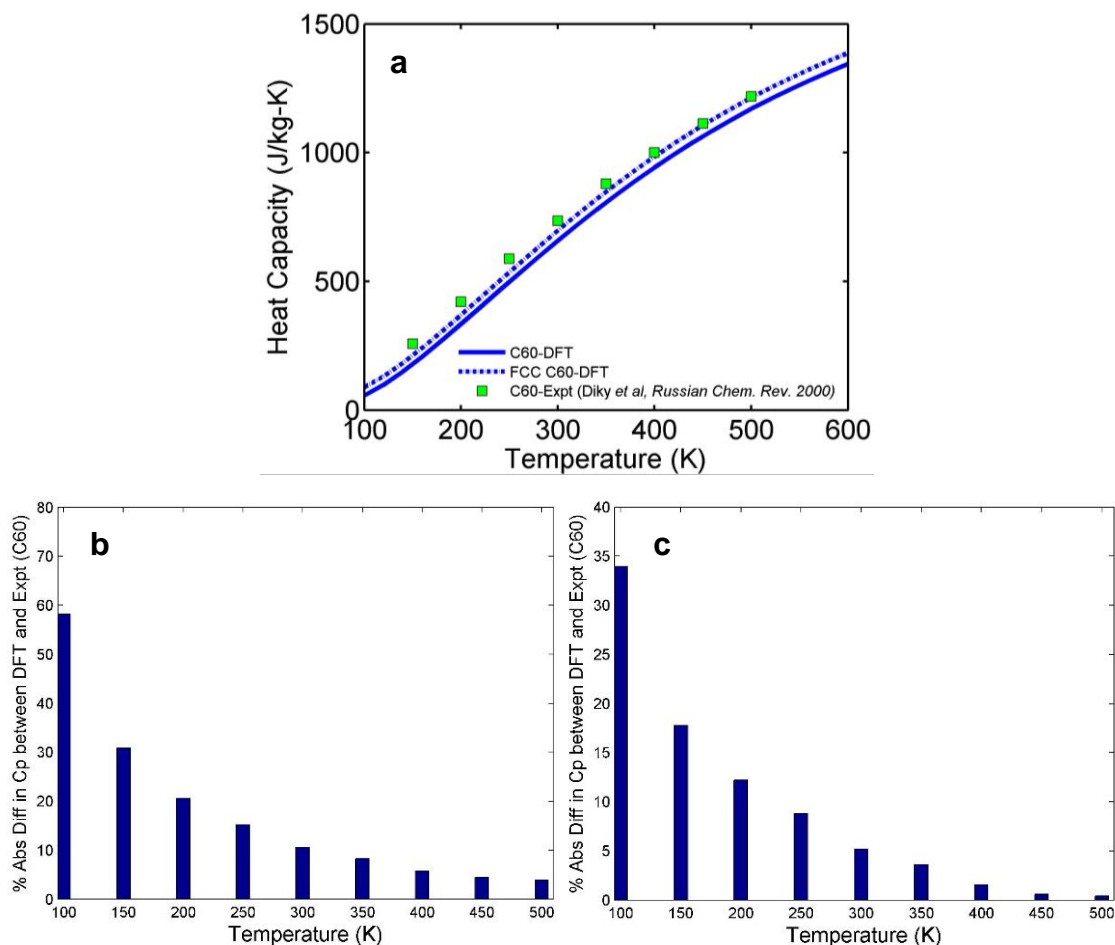


**Figure 4.4 Temperature dependent heat capacity values of C<sub>60</sub>.** **a**, Comparison between experimental [111], DFT isolated system prediction, and DFT periodic system predictions. **b**, Above temperatures of 200 K, a maximum deviation of 20% is seen. This value increases rapidly to about 60% at 100 K. **c**, Using the spectrum from an FCC unit cell, the maximum deviations drops to below 35%.

For the binary LUMCs, the smallest possible system for DFT calculations is a unit cell that typically has more than 250 atoms, making these calculations prohibitively expensive. As an initial approach to determine the baseline heat capacity for these binary LUMCs, we assume that the vibrational spectra of the superatoms in a unit cell are not different from the individual isolated constituents (i.e., ignoring the collective



modes) and arithmetically combine the individual vibrational spectra based on the correct stoichiometric composition. This approach should give reasonable estimates at temperatures above 200 K. The calculated temperature dependent heat capacities for the different LUMCs are shown in Figure 4.5.

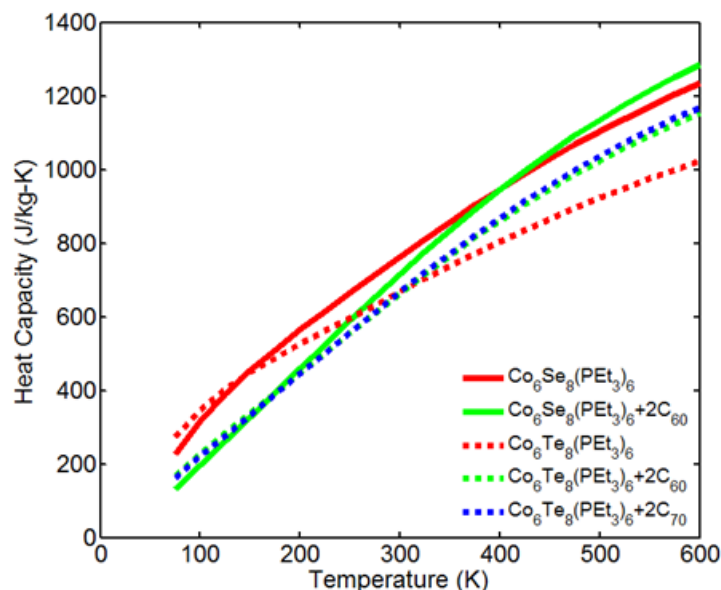


**Figure 4.5 Baseline heat capacity trends for some LUMCs.** These values are calculated using equation 4.1 with inputs from the DFT-driven gamma-point vibrational spectra and scaled by their respective bulk densities.

The heat capacity measurements for CoSe, CoTe, and their binary LUMCs with  $C_{60}$  were measured using the DSC technique. The measured and the DFT-calculated temperature dependent trends of CoTe and CoSe LUMCs are shown in Figure 4.6. The experimental heat capacity trends are not reproducible between different runs and samples of the same material. Further, some of the measured heat capacity values exceed the classical Dulong-Petit limit at relatively low temperatures, making these measurements unreliable. This poses a problem as the LUMC heat capacity value is

needed for determining its thermal conductivity in the FDTR technique. For the CoSe LUMC, the DFT trend does not agree with any of the experimental trends. The CoTe LUMC calculation coincides with one of the measured DSC trends. It is puzzling why DSC measurements are inconsistent between runs; one possible reason could be due to sample degradation within the sealed container. The calculated heat capacity values are a lower bound and, thus, used as a first approximation for fitting the FDTR data that result in an upper bound on the measured thermal conductivity.

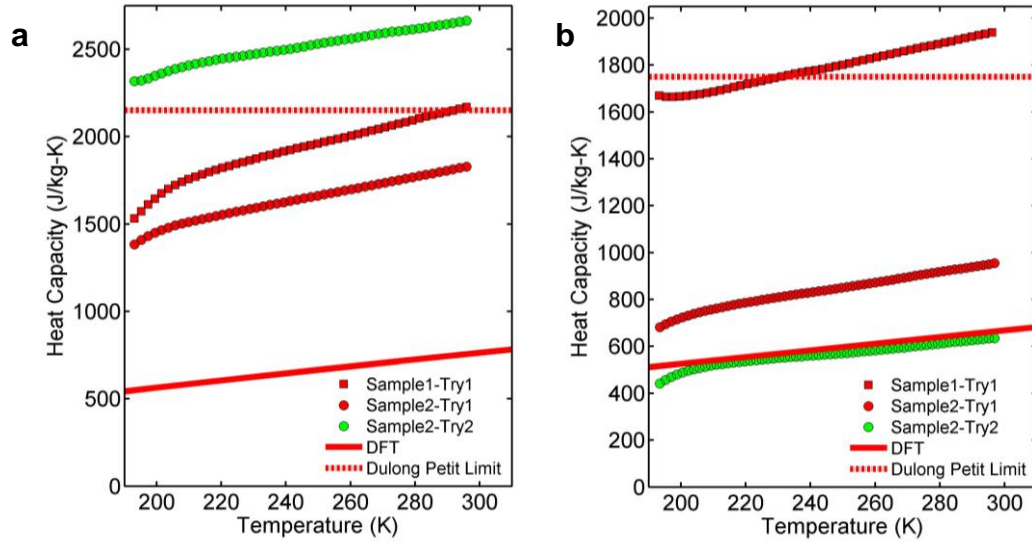


**Figure 4.6** Heat capacities of **a**, CoSe and **b**, CoTe LUMCs. Some of the measured heat capacities exceed the classical Dulong Petit limit at temperatures above 200 K.

#### 4.4.2 Room Temperature Thermal Conductivity

The measured room temperature thermal conductivity of the LUMCs are shown in Table 4.2 below.

**Table 4.2 Room temperature thermal conductivity of LUMCs.**

<b>Acronym</b>	<b><math>k_{LUMC}</math> (W/mK)</b>	<b>Assumed Cp (J/gK)</b>	<b>Type</b>
CoSe	$0.22 \pm 0.05$	0.764	Mono
CoSe.C60	$0.26 \pm 0.06$	0.715	Binary
CoTe	$0.12 \pm 0.03$	0.667	Mono
CoTe.C60	$0.16 \pm 0.04$	0.663	Binary
CoTe.C70	$0.14 \pm 0.04$	0.667	Binary

For both mono- and binary LUMCs, the room temperature thermal conductivities of these crystals are low, comparable to those of amorphous plastics and nano-structured materials. For comparison, a C<sub>60</sub> LUMC has a thermal conductivity of 0.4 W/mK. There is a slight thermal conductivity increase observed for the binary LUMCs over its corresponding mono LUMCs. Strong ionic bonds hold the different superatoms together in the binary LUMCs and might be responsible for our observation of increased thermal conductivity. There is insignificant difference in the measured thermal conductivity between the C<sub>60</sub> or C<sub>70</sub> binary LUMCs, although the C<sub>70</sub> superatoms are less symmetrical and more orientationally disordered. Finally, a more distinct thermal conductivity decrease is seen with a larger chalcogenide element in the superatom core. This decrease can be attributed to the lower vibrational frequency modes in the crystal (i.e., lower Debye temperatures,  $\theta_{Se} = 153 \text{ K} > \theta_{Te} = 139 \text{ K}$ ) when the heavier tellurium element replaces the lighter selenium element in the core (compare Figures 4.3a and 4.3b). Samples with the lightest chalcogenide element, sulfur, are being fabricated to

verify this decrease.

#### 4.4.3 Temperature Dependent Thermal Conductivity

Materials of such low room temperature thermal conductivity value normally exhibit an amorphous-like temperature dependent thermal conductivity trend [55,112] that increases with increasing temperature due to population effects [113,114]. The temperature dependent thermal conductivity trend for the CoSe LUMC is plotted in Figure 4.7.

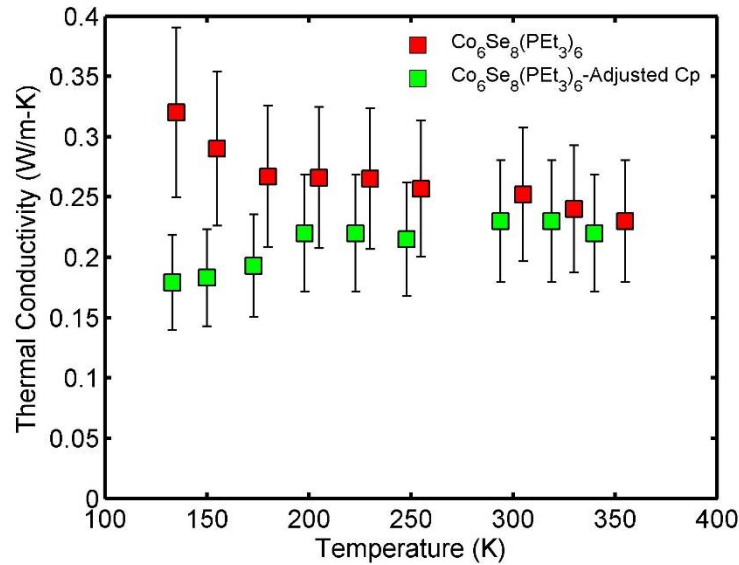


**Figure 4.7** Temperature dependent thermal conductivity of CoSe LUMC.

Two trends can be seen in Figure 4.7, obtained by using two different sets of heat capacity values. The trend represented by the red squares uses the as-calculated heat capacity values. The green squares are thermal conductivity values obtained with the calculated heat capacity scaled using the discrepancy percentages seen in the isolated C<sub>60</sub> case at the corresponding temperatures. These two trends serve as the upper and

lower bounds on the temperature dependent thermal conductivity trend. In both cases, the thermal conductivity of the CoSe LUMC is quite flat with decreasing temperatures until 200 K. These trends diverge around temperatures below 200 K. One trend indicates a crystal-like behavior with increasing thermal conductivity while the other depicts an amorphous-like decrease in thermal conductivity with decreasing temperature. As the calculated heat capacity of an LUMC is expected to agree better with the actual heat capacity than in the C60 case, the true temperature dependent trend should be closer to the upper bound crystalline trend. Getting the correct temperature dependent trend is essential for understanding the transport mechanisms in these mono-species LUMC.

## **4.5 Conclusion**

Thermal properties of a new class of LUMCs were investigated. Using the FDTR technique, we found that these nano-liter sized LUMCs have room temperature thermal conductivity values similar to those of amorphous bulk polymers. The actual transport mechanisms in this material is still currently inconclusive - whether it is phonon-dominated as in other crystals, amorphous-like as in materials of similar low room temperature thermal conductivity, or a combination of the two. With a low thermal conductivity and a moderately high electrical conductivity, these materials are potential candidates for future thermoelectric generators.

## CHAPTER 5

### Other Completed Work

#### 5.1 Bi<sub>1-x</sub>Sb<sub>x</sub> Alloy Nanocrystals: Colloidal Synthesis, Charge Transport and Thermoelectric Properties

##### 5.1.1 Introduction

Bismuth antimony alloys (Bi<sub>1-x</sub>Sb<sub>x</sub>, 0<*x*<1) have attracted extensive attention due to their potential applications as the best *n*-type thermoelectric material at low temperatures (20-200 K) [115]. The material dimensionality and size have strong influence on the transport properties of Bi<sub>1-x</sub>Sb<sub>x</sub> alloys. Dresselhaus *et al.* predicted that thermoelectric figure of merit  $ZT = \frac{S^2 \sigma}{k} T$ , (where *S* is Seebeck coefficient,  $\sigma$  is the electrical conductivity, and *k* is the thermal conductivity) can approach ~2.5 at 77 K for Bi<sub>1-x</sub>Sb<sub>x</sub> nanowires with a diameter smaller than 20 nm [116]. Such high ZT was attributed to the increase in the density of states close to the Fermi level of Bi<sub>1-x</sub>Sb<sub>x</sub> nanowires due to the quantum confinement. So far, most experimental charge transport studies have been performed on polycrystalline Bi<sub>1-x</sub>Sb<sub>x</sub> alloys [117] with grain size in the range of 100 nm to hundreds of microns and on Bi<sub>1-x</sub>Sb<sub>x</sub> nanowires [118] with >~40 nm diameter. Transport and thermoelectric properties of Bi<sub>1-x</sub>Sb<sub>x</sub> alloys with grain sizes below ~40 nm have not yet been studied because of the lack of uniform, high quality Bi<sub>1-x</sub>Sb<sub>x</sub>

nanostructures, especially  $\text{Bi}_{1-x}\text{Sb}_x$  NCs smaller than 20 nm. In view of their peculiar physical properties and promising thermoelectric performance, it is highly desirable to develop a method for synthesizing sub-10 nm  $\text{Bi}_{1-x}\text{Sb}_x$  NCs with good size distribution and precise compositional control. However, this remains a challenge mainly due to the lack of appropriate precursors.

In this work, our collaborators from The University of Chicago developed a colloidal synthesis process for monodispersed sub-10 nm  $\text{Bi}_{1-x}\text{Sb}_x$  alloy nanocrystals (NCs) with controllable size and composition. The surface chemistry of  $\text{Bi}_{1-x}\text{Sb}_x$  NCs was tailored with inorganic ligands to improve the interparticle charge transport as well as to control the carrier concentration. For characterization, the NCs were dried and compressed in a stainless steel die into square-shaped (6 mm side, thickness  $\sim 1\text{-}2$  mm) pellets under  $\sim 15$  MPa for 30 min at room temperature with some pellets subsequently annealed at  $250^\circ\text{C}$ . Our collaborators performed Hall effect and temperature dependent (10-300 K) electrical measurements. We characterized the thermal conductivity of these pellets using a steady-state method [119]. [Published in “ $\text{Bi}_{1-x}\text{Sb}_x$  Alloy Nanocrystals: Colloidal Synthesis, Charge Transport, and Thermoelectric Properties”, H Zhang, JS Son, J Jang, JS Lee, WL Ong, JA Malen, DV Talapin. *ACS Nano* **7** (11), 10296-10306.]

### 5.1.2 Method

The steady-state technique used to determine the thermal conductivity of  $\text{Bi}_{1-x}\text{Sb}_x$  NC pellets employs the experimental setup shown in Figure 5.1. The jig consists of two parts – a stainless steel (material code SS303) top and an aluminum (material code

6061T6) bottom with holes drilled for embedding platinum thermistors (calibrated PT111 from Lakeshore Cryotronic Inc). A nichrome heater wire (Lakeshore Cryotronics Inc) is wound around the top piece while the bottom piece is connected to a cryostat cold finger (Oxford Instrument). Both pieces have the same cross-sectional area,  $A = 6 \times 6 \text{ mm}^2$ , matching that of the samples. All measurements were performed under high vacuum in the cryostat.

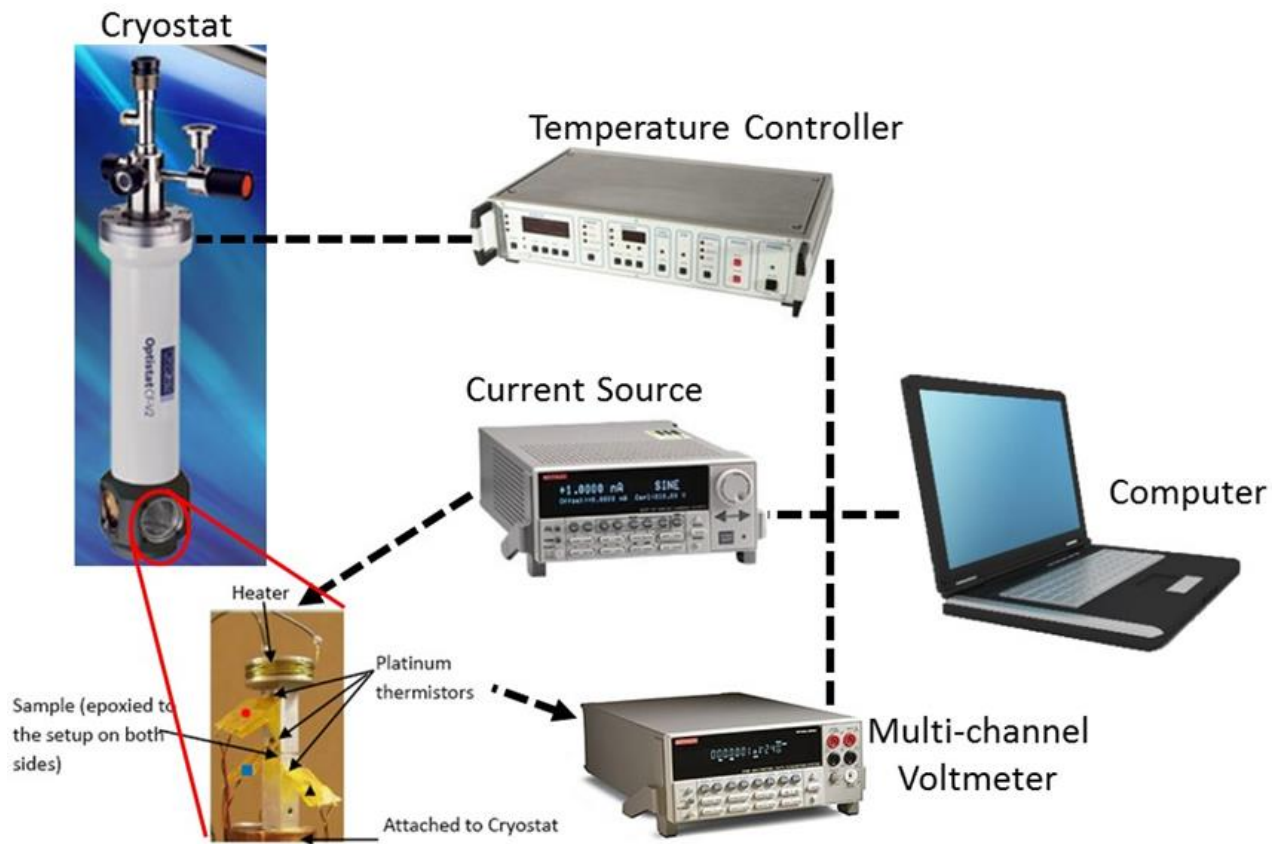


**Figure 5.1 Setup for steady-state measurement.** The jig with a sample sandwiched between the stainless steel top and aluminium bottom is shown in the bottom left corner. Nichrome wires on top acted as the Joule heater. Platinum thermistors were used to measure the temperatures across the jig at designated locations. The red circle, blue square, and black triangle correspond to positions of the first, second, and third thermistor whose representative readings are shown in Figure 5.2.



In the experimental setup, a current is drawn from a digital current source (Keithley 6221) by the heater to Joule heat the jig (Nichrome wire from Lakeshore Inc). The sample is epoxied (using Stycast 2850FT-catalyst 9) and sandwiched between the top and bottom parts of the jig. Two thermistors (denoted with a red dot and blue square in Figure 5.1) are located 10 mm apart on the top piece for metering the heat ( $q$ ) flowing to the sample. The difference in the readings from the lower thermistor in the top piece [denoted with a blue square, located at 2.5 mm ( $L_{SS}$ ) above the lower edge of the top piece] and the thermistor in the bottom piece [denoted with a black triangle, located at 3 mm ( $L_{Al}$ ) below the upper edge of the bottom piece] gives a temperature drop mainly due to the sample. The resistances of these three thermistors are read by a digital multimeter/data acquisition system (Keithley 2700/7700 with 20-channel multiplexer) using a 4-wire configuration to eliminate errors arising from the lead resistances. From the measured resistance, each thermistor temperature is determined by comparing with its calibration curve. These thermistors were continuously monitored for the steady-state condition where a flat temperature profile is obtained with time as shown in Figure 5.2a. The actual amount of heat flow and temperature drop across the sample were then used as inputs to a one-dimensional thermal resistance circuit (simplified to equation 5.1) to obtain the sample thermal conductivity ( $k_{sample}$ ),

$$q = \frac{A(T_{sample,top} - T_{sample,bottom})}{\frac{L_{SS}}{k_{SS}} + \frac{L_{Al}}{k_{Al}} + \frac{L_{epoxy,top}}{k_{epoxy,top}} + \frac{L_{epoxy,bottom}}{k_{epoxy,bottom}} + \frac{L_{sample}}{k_{sample}}} \quad (5.1)$$

The whole experiment was performed under high vacuum to eliminate heat loss through convection. Radiative losses were minimized by i) a radiation shield situated between the jig and the interior wall of the cryostat, ii) ensuring jig surfaces were well-polished to reduce their emissivities, iii) reducing the exposed surface areas, and iv) using a secondary radiation shield around the heater. The steady-state heat flow along the jig was metered using the two thermistors located on the top part of the jig and compared to the supplied electrical heating energy. The metered heat flow was typically within 6% of the possible supplied heat, indicating minimal heat losses (Figure 5.2b). The calculated thermal conductivity of the sample was dynamically updated through the whole duration of the experiment showing minimal variation at steady-state (Figure 5.2c). Calibration of this setup as well as the error analysis for this method can be found in Appendix D Sections I and II. The in-house code for communicating with the respective equipment, acquiring and analyzing the data is discussed in Appendix D Section III

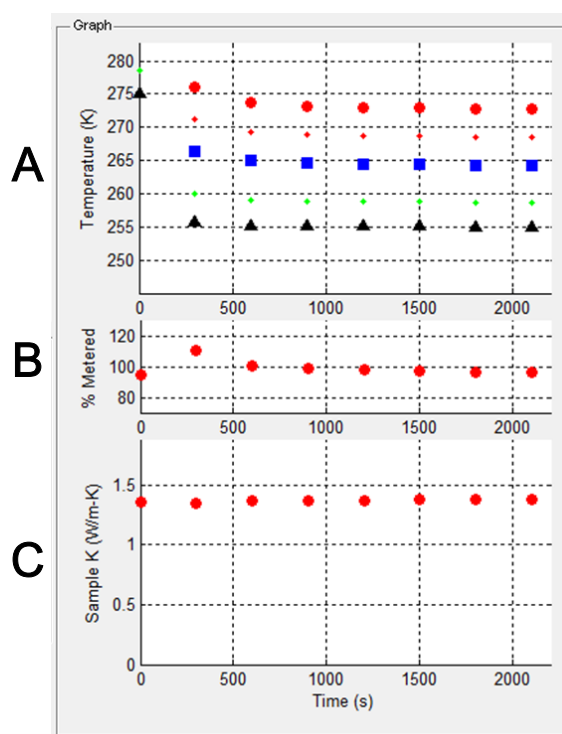


**Figure 5.2 a, Temperature profiles of the thermistors with time.** After 1500s, steady state was reached as evident from the flat temperature profiles from all three thermistors. **b, Measured heat flow as a percentage of heat supplied.** **c, Corresponding thermal conductivity of the sample.**

### 5.1.2 Results and Discussion

Temperature dependent thermal conductivity measurements were performed on four different pellets. The differences between these samples are summarized in Table 5.1.

**Table 5.1 Pellets process history and their average grain size.**

<b>Pellet</b>	<b>Process</b>	<b>Grain size (nm)</b>
I	Cold Pressed	15
II	Same as I but further annealed at 250°C	18
III	Cold Pressed under hydrazine (N <sub>2</sub> H <sub>4</sub> ) environment	33
IV	Same as III but further annealed at 250°C	38

Figure 5.3 contains temperature-dependent thermal conductivity trends of Bi<sub>1-x</sub>Sb<sub>x</sub> samples labeled I to IV as well as for a bulk Bi<sub>1-x</sub>Sb<sub>x</sub> sample [120]. The thermal conductivity of these nanocrystal pellets are lower than their bulk counterparts by at least a factor of two at all temperatures in the tested range. It can be seen that the thermal conductivity of Bi<sub>1-x</sub>Sb<sub>x</sub> nanocrystal pellets reduces with decreasing temperature and flattens out below a temperature of 120 K before increasing again after a temperature of 50 K. This result mirrors the bulk behavior quite well except for an earlier onset of a thermal conductivity minimum upon cooling which plateaus to a temperature of 50 K. A similar discrepancy in the position of the thermal conductivity minimum is also observed for BiSbTe nanostructured pellets, relative to bulk BiSbTe [121]. This minimum is a result of the competition between decreasing phonon contributions and increasing electron contributions to thermal conductivity [122]. Only the room temperature thermal conductivities for these samples are published in the *ACSnano*

article [119].

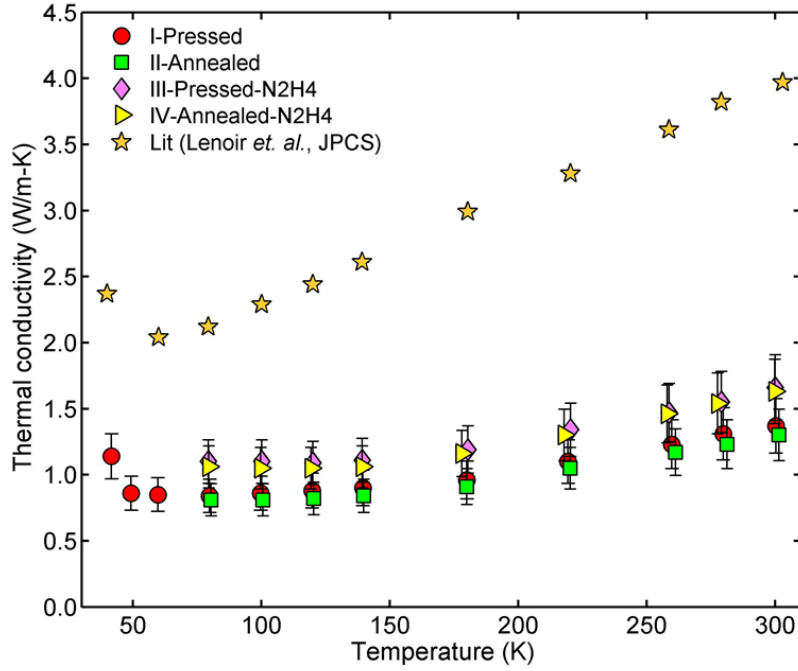


**Figure 5.3** Temperature dependent thermal conductivity of  $\text{Bi}_{1-x}\text{Sb}_x$  pellets. The temperature dependent trend obtained is similar to that of a bulk  $\text{Bi}_{1-x}\text{Sb}_x$  sample [120].

## 5.2 Experimental estimates of in-plane thermal conductivity in FePt-C granular thin film heat assisted magnetic recording media using a model layered system

Cross-plane thermal conductivity  $k$  measurements of vertical stacks of FePt/C were used to estimate the in-plane thermal conductivity of Heat Assisted Magnetic Recording (HAMR) media that consist of columnar FePt grains segregated by thin amorphous

carbon grain boundaries. FePt/C multilayers with varied repeat units and FePt layer thicknesses (chosen to represent HAMR media grain sizes) were measured using the frequency domain thermoreflectance method to determine  $k$  in the direction normal to the layers. The data suggest that when FePt grains are less than 8 nm in diameter, the in-plane  $k$  for HAMR media is below 1 W/m-K and the anisotropy of  $k$  (cross-plane/in-plane) will exceed 10 [123]. I have helped in the thermal conductivity measurements of the films using the FDTR technique. [Published in “Experimental estimates of in-plane thermal conductivity in FePt-C granular thin film heat assisted magnetic recording media using a model layered system”, H Ho, AA Sharma, WL Ong, JA Malen, JA Bain, JG Zhu, *Appl. Phys. Lett.* **103** (13), 131907]

### **5.3 Compositionally matched nitrogen-doped $\text{Ge}_2\text{Sb}_2\text{Te}_5/\text{Ge}_2\text{Sb}_2\text{Te}_5$ superlattice-like structures for phase change random access memory**

#### **5.3.1 Abstract**

A compositionally matched superlattice-like (SLL) structure comprised of  $\text{Ge}_2\text{Sb}_2\text{Te}_5$  (GST) and nitrogen-doped GST (N-GST) was developed to achieve both low current and high endurance phase change random access memory (PCRAM). N-GST/GST SLL PCRAM devices demonstrated ~37 % current reduction compared to single layered GST PCRAM and significantly higher write/erase endurences of  $\sim 10^8$  compared to  $\sim 10^6$  for  $\text{GeTe}/\text{Sb}_2\text{Te}_3$  SLL devices. The improvements in endurance are

attributed to the compositionally matched N-GST/GST material combination that lowers the diffusion gradient between the layers and the lower crystallization-induced stress in the SLL as revealed by micro-cantilever stress measurements [124]. [Published in “Compositionally matched nitrogen-doped  $\text{Ge}_2\text{Sb}_2\text{Te}_5/\text{Ge}_2\text{Sb}_2\text{Te}_5$  superlattice-like structures for phase change random access memory”, CC Tan, L Shi, R Zhao, Q Guo, Y Li, Y Yang, TC Chong, JA Malen, WL Ong, TE Schlesinger, JA Bain, *Appl. Phys. Lett.* **103** (13), 133507.]

### 5.3.2 Introduction

Phase Change Random Access Memory (PCRAM) is a good candidate for replacing FLASH memory due to its long write/erase endurance, fast switching speed and scalability [125]. PCRAM technology relies on the significant but reversible change in the electrical and optical properties of certain class of materials when its atomic structure is transformed through the application of current pulses or other excitation sources [126,127]. For example, the GST electrical resistivity increases reversibly by three orders of magnitude as it switches between its crystalline and amorphous phase when Joule heated [127]. The magnitude of the current pulses needed for heating to phase change the material is currently too high for shrinking the access transistor area small enough to achieve high density memory arrays [127]. One method to reduce the current pulses is decreasing the thermal conductivity of the PCRAM material. Creating a superlattice of the PCRAM material having multiple interfaces for the scattering of thermal carriers is, thus, a possible way to lower the required current pulse magnitude.

### 5.3.3 Thermal Conductivity Measurements

I have performed the FDTR measurements and analyzed the thermal conductivity data for this work. The following set of data is not published in any journal. This work is performed with our collaborators from the Electrical Engineering department in CMU and Data Storage Institute (A\*STAR, Singapore). To investigate the thermal conductivity of this phase change material, amorphous and crystalline single layered GST, single layered N-GST, and SLL N-GST-4%/GST (deposited in 1:1 ratio) structures were fabricated. The total thickness of all the phase change materials and SLL structures is ~50 nm. This is achieved in the SLL by reducing the thickness of each layer to offset the increase in the number of layers. The effective thermal conductivities of these samples are measured using the FDTR technique described in Chapter 2 and plotted in Figure 5.4. These samples were measured as deposited (i.e., amorphous) and after annealing at temperatures of 300°C or 350°C in vacuum for two minutes (i.e., crystalline). The overall uncertainty in the thermal conductivity measurement is between 13-15%. In Figure 5.4, the period length describes the total thickness of each N-GST-4%/GST bilayer while the number beside each SLL data point indicates the number of bilayers in the SLL.



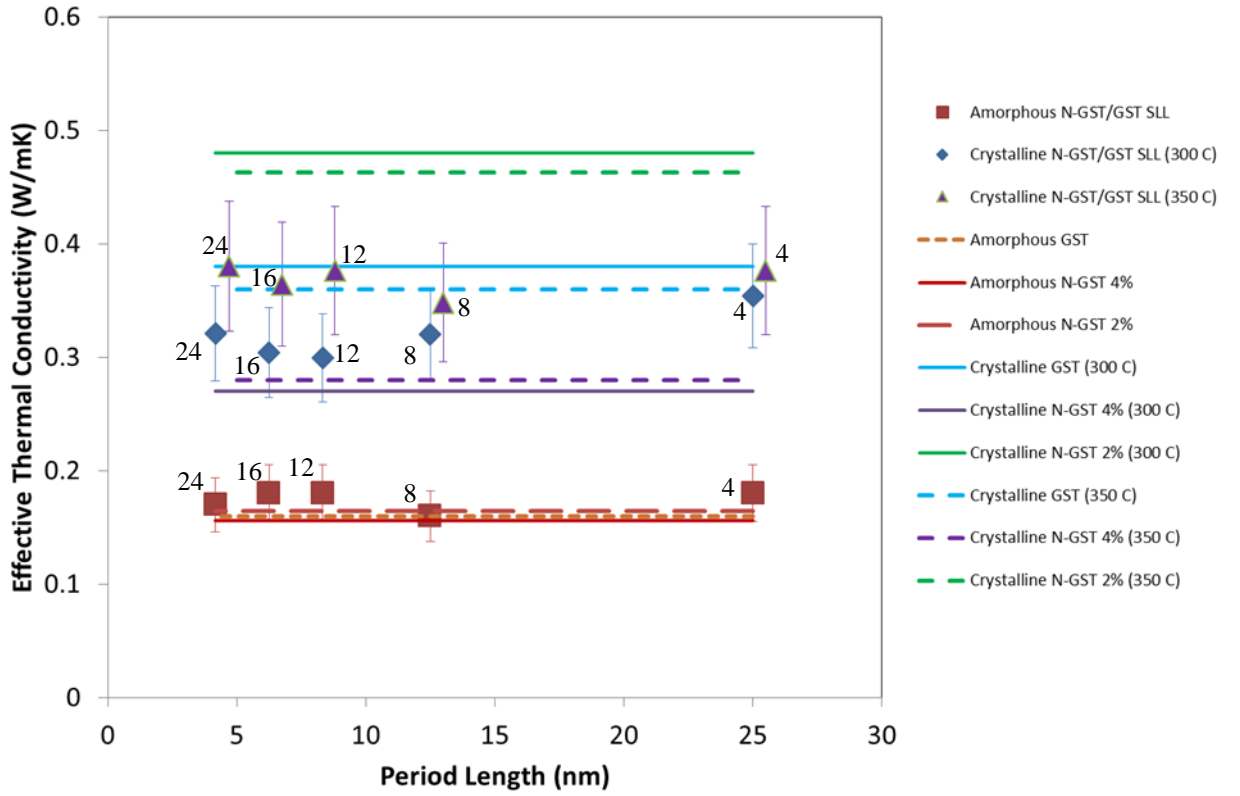


**Figure 5.4 Thermal conductivity of the N-GST/GST samples.**

The thermal conductivities of the amorphous phase change materials in the single layer and the SLL structures are similar. This result is anticipated as thermal transport in amorphous materials at room temperature is dominated by carriers with mean free paths shorter than the period lengths, rendering boundary scattering between layers to be ineffective [128,129].

Annealing at 300°C crystallized these amorphous films. Our collaborator used X-ray diffraction to characterize the single-layer films; the spectra shown Figure 5.5 [130]. The GST and N-GST-4% form a face-centered cubic (FCC) structure with the former having higher crystallinity due to the presence of higher and narrower peaks. The N-GST-2% packs into a hexagonal close-packed (HCP) crystal with even higher

crystallinity than the two other films.

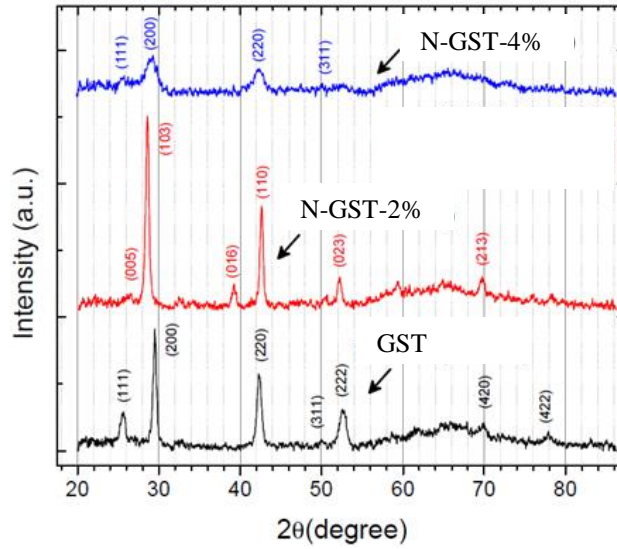


**Figure 5.5 X-ray Diffraction spectra of N-GST-4 %, N-GST-2 %, and GST.**

Of these three materials, N-GST-2% has the highest thermal conductivity while the N-GST-4% has the lowest. The differences in the crystallinity in these three films could account for the thermal conductivity differences [130]. The measured thermal conductivities of the different layers crystalline SLL fall between the values of its constituent components with a slight minimum occurring for the 12-layer structure. A simple effective medium calculation based on the volume fraction of each layer predicts a SLL thermal conductivity of 0.32 W/mK, a value that fits through most of the measured SLL values.

Increasing the annealing temperature to 350°C does not significantly change the thermal conductivities measured for the single layer phase change materials. The thermal conductivity trend of the SLL, however, becomes flat and fluctuates at a higher value of 0.36 W/mK, matching the value measured for the crystalline GST-350°C film.

We postulate that the possible reasons for the disappearance of the minimum are i) a possible change in the packing structure within each layer; ii) substantial increase in interlayer diffusion. We did not, however, characterize these films to investigate these claims.

As the thermal conductivities of the GST and N-GST are inherently low, creating a superlattice did not help to reduce its thermal conductivity significantly. Nano-graining these materials will introduce more scattering boundaries that might further lower the thermal conductivity but only by a small amount. Other means of reducing the current pulses should be explored in order to increase the density of the PCRAM arrays.

# CHAPTER 6

## Summary and Outlook

### 6.1 Nanocrystal Arrays

In Chapter 2, the thermal conductivity for a range of nanocrystal arrays (NCA) thin films was first measured and found to be in a range of 0.1 to 0.3 W/m-K [55]. NCA thermal conductivity trends were obtained with respect to core diameters, temperature, core materials, and ligand types. From these trends, several insights for the thermal transport in NCA were obtained. These original insights include:

- Energy transport in an NCA is mediated by the density and chemistry of the organic/inorganic interfaces as well as the volume fractions of nanocrystal cores and surface ligands.
- The measured NCA thermal conductivity agrees with an effective medium approximation theory only when the interfacial thermal conductance between the core and ligand is taken into account, hinting the importance of the role of the interface.
- Changing the interfacial properties by replacing the ligands or the core materials alters the NCA thermal conductivity, presenting further evidences for interface-mediated thermal transport. A core material of lower Debye temperature will have a lower NCA thermal conductivity as compared to a core of higher Debye temperature. This is due to the higher vibrational overlaps between the higher

Debye temperature core and the ligand. Short inorganic ligand groups will result in higher NCA thermal conductivity than long organic ligands. A composite effect might be in play with an increased interfacial thermal conductivity, a reduced volume fraction of the ligands, and a higher ligand thermal conductivity.

- Thermal conductivity trends upward then plateaus with temperature. This result supports the proposition that elastic scattering occurs at the organic-inorganic interfaces.
- The temperature for the onset of the thermal conductivity plateau in a NCA is related to the location of the overlaps between the vibrational states of the cores and ligands.

In Chapter 3, to get a more in-depth understanding of the NCA heat transport, an atomistic gold-core-dodecanethiol-ligand NCA with realistic empirical potentials was built and studied using MD simulations and LD calculations [86]. This study was the first to use MD to predict NCA thermal conductivity and one of the first in literature to have a full-scale NCA model containing several hundred thousands of atoms [91,95,97,98]. The predicted NCA thermal conductivity values and trends with respect to the thickness and core diameter are in close agreement with the experiments. Using this model, the interfacial thermal conductance between the core and the passivating ligands are predicted with different temperature and core diameters. A self-consistent method is then used to verify the applicability of the EMA models in describing NCA thermal conductivity. The core Debye temperature effect on the NCA thermal conductivity seen in the experiment was also investigated. The following

calculations/results are novel additions to the literature:

- A full-scale NCA model for using the NEMD technique to obtain the NCA thermal conductivity. A different arrangement in the form of a cubic-like structure was implemented to get the interfacial thermal conductance.
- A decreasing interfacial thermal conductance trend for the organic-inorganic interface with increasing ligand footprint on the nanocrystal surface was discovered, which in turn saturates with increasing nanocrystal diameter.
- A geometrical scaling law was derived that successfully relates the interfacial thermal conductance to that of a self-assembled monolayer (SAM) interface having identical ligand group and substrate material. This scaling law, hence, provides a computationally inexpensive method for obtaining the diameter-dependence of interfacial thermal conductance for other NCA systems.
- No temperature dependence of the interfacial thermal conductance was observed from the MD calculations – a result that agrees with our experimental conclusion that elastic scattering events dominate across these organic-inorganic interfaces.
- The first self-consistent test performed on the EMA thermal conductivity models used for predicting the NCA thermal conductivity. A slight thermal conductivity minimum at small nanocrystal diameters is also found but not experimentally verified.
- Changing the atomic mass of the core in the NCA model to understand the core Debye temperature effect on the NCA thermal conductivity. Both the thermal

conductivity and interfacial thermal conductance exhibit a non-monotonic trend that peaks at the same small atomic mass. Several factors could have led to this peculiar trend.

## **6.2 Large Unit Cell Molecular Crystals**

The lower bound for the specific heat capacities of these LUMCs was predicted by using vibrational modes from density functional theory (DFT) based lattice dynamics as inputs to the theoretical phonon heat capacity formulation. These calculations were performed as the experimental heat capacity measurements did not yield repeatable results across different runs. These lower bound values were then used as inputs to the analytical solution for the heat diffusion equation used in the FDTR technique to predict thermal conductivity.

Preliminary measurements of LUMCs indicate that the thermal conductivity is between 0.2 and 0.4 W/mK at the temperature of 300 K, comparable to that of an amorphous polymer. A slight increase in thermal conductivity is observed for the binary-species LUMCs that contain fullerene derivatives over their corresponding mono-species LUMCs. This increase may be attributed to the stronger ionic intermolecular bonds in the binary LUMCs. The presence of a larger chalcogenide element in the inorganic core of the superatom decreases the thermal conductivity of the LUMC. This decrease is consistent with lower frequency vibrational modes that have a lower group velocity in the crystal. The temperature dependent thermal conductivity of a mono-species CoSe LUMC has a crystalline-like behavior, unlike most low thermal conductivity materials.

## 6.3 Outlook

NCAAs have been demonstrated as a technologically important and affordable material for replacing existing expensive single crystal semiconductor in future devices [2]. Thermal management in these devices is an important consideration as waste heat (a byproduct during operation) will adversely affect the device's designed efficiency and lifetime. The low NCA thermal conductivity will be a challenge for heat dissipation for most electronic devices. Better engineering designs to incorporate heat wicking paths are needed to prolong the lifetime of NCA-based devices. Better bonding between the ligands and the cores might also be a possible solution to increase the NCA thermal conductivity if the desired properties are not compromised. On the other hand, the low thermal conductivity is a boon for scavenging waste heat, increasing the NCA thermoelectric performance. The relatively inexpensive solution-based NCA fabrication process mitigates the need for high thermoelectric conversion efficiency in NCA-based thermoelectric devices. The cost-to-performance factor should be, hence, used for deciding the economic feasibility of any NCA-based devices.

It will be interesting to determine the thermal conductivity of binary-core NCA and NCAs with core-shell cores [2]. The binary-core NCAs are NCA formed using two different types of nanocrystals. Will such a NCA still have a thermal conductivity predictable by the EMA? What kind of modifications will be needed in the EMA formulation as there are now more than one type of core, ligand, and interface? A simple arithmetic or geometrical average may be sufficient. This same set of questions exist for the NCAs with core-shell cores. It will be, however, interesting to compare



the interfacial thermal conductance obtained in this core-shell structure with the one from a uniform core of the shell or core materials. Emergent vibrational modes will arise in these core-shell structures resulting in a different interfacial thermal conductance.

The LUMCs discussed in Chapter 4 are quite new and more work is needed. In terms of thermal transport, thermal conductivity values for all the LUMCs have to be further confirmed with better estimates/measurements of their heat capacities. The temperature dependent thermal conductivity trend on the binary LUMCs will be interesting as stronger intermolecular forces act between the different superatoms. The existence of fullerenes in some of these binary LUMCs, however, will scatter more phonons as they can spin continuously at high temperatures (e.g., temperatures above 260 K in pure C<sub>60</sub> crystals) [43]. An additional complication comes from the conducting electrons flowing in the extensive  $\pi$ -orbitals, which may increase the thermal transport. The question, hence, is how the temperature dependent trend be different from that of a mono-species LUMCs. As these binary LUMCs have the potential to be good thermoelectric generators, measurements of the thermopower on these materials will be of interest for comparison to existing materials.

# Appendix A

## I Calculation of volume fraction and interface density in NCA

## II Figures

## III Tables

## I Calculation of core volume fraction and interface density in NCA

The core volume fraction is estimated using the equation from Minnich [75],

$$\text{Core volume fraction, } \varphi = \frac{\frac{4}{3}\pi\left(\frac{diaCore}{2}\right)^3}{Vol_{eff\_cell}} \text{ where } diaCore \text{ is the diameter of the core}$$

and  $Vol_{eff\_cell}$  is the effective volume of a cell containing a core.

As a NCA is a FCC packed film [2], the face-diagonal distance on a conventional FCC unit cell is  $F_{dist} = 2diaCore + 2L$  where  $L$  is the separation between 2 nearest cores due to presence of ligands (e.g., in oleic acid capped PbS,  $L = 1.5\text{nm}$ ).

$$Vol_{eff\_cell} = \frac{\left[F_{dist} \cos(45^\circ)\right]^3}{4} \text{ where the factor of 4 in the denominator results from the}$$

number of cores in a FCC conventional unit cell.

The interface density is estimated following the equation from Minnich [75],

$$\text{Interface density, } \Phi = \frac{6\phi}{\text{diaCore}}$$

The core volume fraction and interface density for the PbS NCA diameter series are shown in Table A3 as an example.

## II Figures

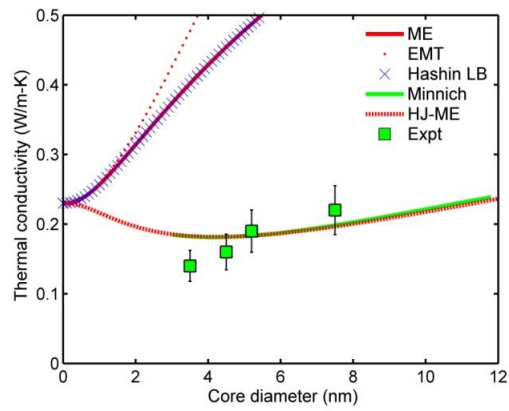


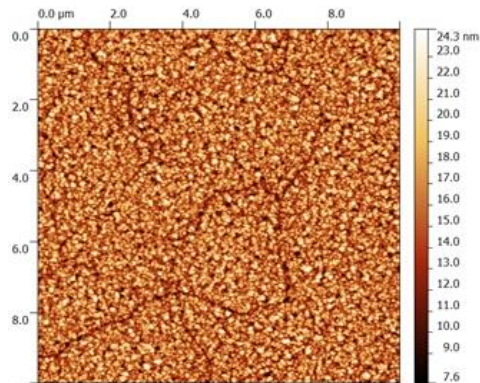
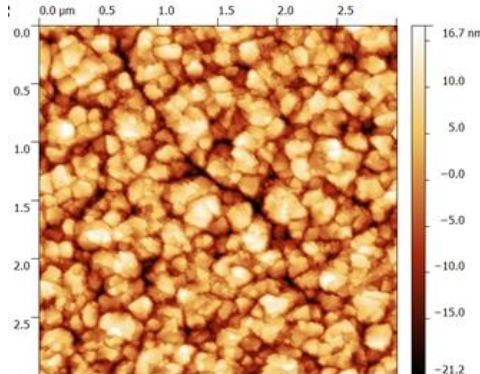
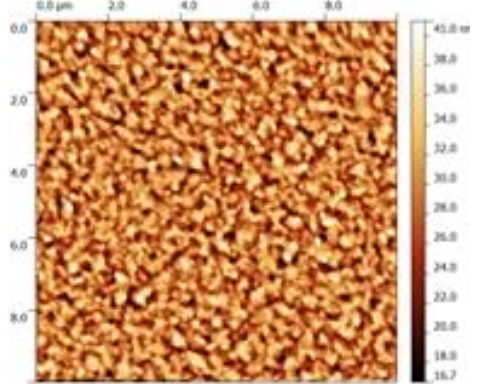
**Figure A1** EMA models with PbS-oleic NCA series using thermal conductivity of liquid oleic acid. The thermal conductivity of liquid oleic acid is 0.23 W/m-K ([76]).

### III Tables

**Table A1 Fitting parameters for FDTR**

	<b>Layer Thickness (nm)</b>	<b>Thermal Conductivity (W/m-K)</b>	<b>Volumetric Heat Capacity (KJ/m<sup>3</sup>-K)</b>
<b>Au Layer</b>	100-250 (measured by SEM & AFM)	Measure using 4-point probe and calculate k from Weidemann Franz Law and FDTR of Au layer on bare substrate	2500 (@ 300 K, otherwise use ref. [131])
<b>NCA Layer</b>	30-150 (measured by SEM & AFM)	fitting parameter from FDTR	<ul style="list-style-type: none"> <li>- Measured by DSC for T &gt;150 K, otherwise unimportant to fitting per discussion in Methods.</li> <li>- To converted from J/g-K to J/m<sup>3</sup>-K, multiply by the relevant density from Table A4</li> <li>- Temperatures where DSC showed a peak, heat capacity used for FDTR model is interpolated from two smooth curves drawn before and after the peak.</li> </ul>
<b>Si Substrate (10<sup>17-18</sup> B atoms/cm<sup>3</sup>)</b>	525 x 10 <sup>3</sup>	Measure using separate FDTR sample without NCA layer (~130 W/m-K at 300K)	1678 (@ 300 K, otherwise use ref. [132])

**Table A2 Characterisation of NCA film roughness using AFM.**

Core (diameter) Ligand type Film thickness	AFM image	Root-mean-square roughness
PbS (7.5 nm) Nonanoic Acid 40 nm		2.5 nm
PbS (7.5 nm) Nonanoic Acid 70 nm		6 - 7 nm
PbS (3.5 nm) Oleic Acid 50 nm		4 – 5 nm

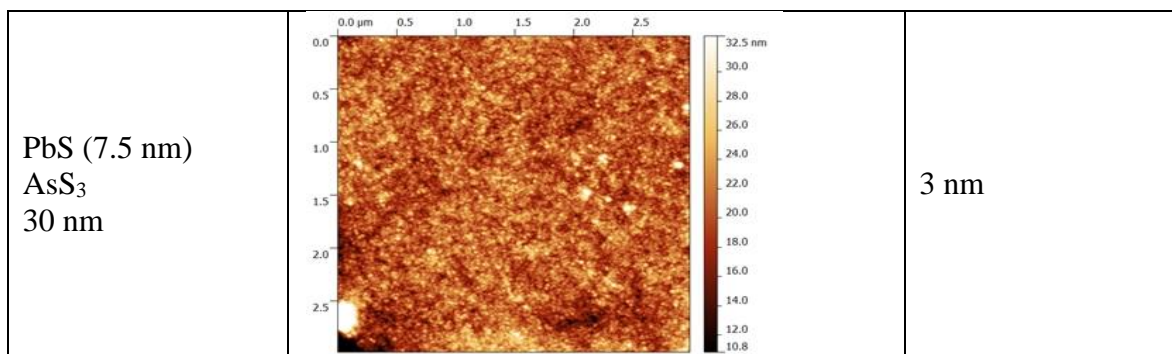


**Table A3 Core volume fraction and interface density for PbS-Oleic acid NCAs.**

Core diameter (nm)	Core volume fraction	Interface density (m <sup>-1</sup> )
3.3	0.24	4.37 x 10 <sup>8</sup>
4.5	0.31	4.17 x 10 <sup>8</sup>
5.2	0.35	3.99 x 10 <sup>8</sup>
7.5	0.43	3.43 x 10 <sup>8</sup>

**Table A4 Calculated density of NCAs.**

NCA type	Ligand	Diameter (nm)	Density (kg/m <sup>3</sup> )
CdSe	Tetradecylphosphonic acid (TDPA)	3.5	2200
		4.1	2380
	Octylphosphonic acid (N <sub>2</sub> H <sub>5</sub> ) <sub>2</sub> In <sub>2</sub> Se <sub>4</sub>	5.2	2720
		4.8	5630
PbS	Oleic acid (OA)	3.5	2600
		4.5	3000
		5.2	3190
		7.5	3770
	Nonanoic acid (NA)	7.5	3780
	Na <sub>3</sub> AsS <sub>3</sub>	7.5	5220
	N <sub>2</sub> H <sub>4</sub>	7.5	3840
PbSe	Oleic acid	7.5	4030
PbTe	Oleic acid	7.5	4040
Fe <sub>3</sub> O <sub>4</sub>	Oleic acid	4.5	2260
		8	2830
Au	Dodecanethiol	4.5	6610

## **Appendix B**

### **I Inter- and Intra-molecular Potentials**

### **II Gold Thermal Conductivity from Molecular Dynamics**

### **III Dodecanethiol Solid Thermal Conductivity from Molecular Dynamics**

### **IV Molecular Dynamics Prediction of SAM Interfacial Thermal Conductance**

### **V Uncertainty Analysis**

### **I Inter- and Intra-molecular Potentials**

The dodecanethiol ligands are modeled using the Hautman-Klein united atom model [65]. Bond stretching, bending, and torsional potentials govern the bonded interactions within a ligand. The light hydrogen atoms in the ligand backbone are treated implicitly with their masses lumped into the corresponding carbon atoms. Such a simplification reduces computational cost as less atoms and a bigger molecular dynamics (MD) timestep can be used without compromising the MD accuracy for geometrical packing [65,91,92] and thermal conductivity [66,89,133] studies at room temperature. The high vibrational activation temperature of the stiff C-H bond justifies

this simplification. Notwithstanding, these lumped hydrogen atoms are spatially accounted for in the potentials, mimicking the steric effect of the hydrogen atoms [65]. A Morse potential dictates the interaction between the S atoms and the Au cores [134,135]. Lennard-Jones (LJ) potentials and the Lorentz–Berthelot mixing rules [136] are used to model long-range inter- and intra-(CH<sub>2</sub>, CH<sub>3</sub>, and S sites in the same ligand that are at least four bonds away) molecular interactions. The cut-off distance for the Morse and LJ potentials is set at 10 Å. An embedded atom model (EAM) potential [67] is used for the Au atoms as it matches the experimental bulk phonon density of states better than a simple Au Morse potential [137]. The potentials and parameters [66,67,92] used are provided in Table B1.

**Table B1 Potentials and their parameters.**

Potential	Type	Parameters
Bond Stretching [92] $E_s = \frac{1}{2} k_s (r - r_o)^2$	S-C C-C	$k_s = 9.627 \text{ eV/Å}^2, r_o = 1.815 \text{ Å}$ $k_s = 11.27 \text{ eV/Å}^2, r_o = 1.54 \text{ Å}$
Bond Bending [66] $E_\theta = \frac{1}{2} k_\theta (\theta - \theta_o)^2$	S-C-C C-C-C	$k_\theta = 5.388 \text{ eV/rad}^2, \theta_o = 114.4^\circ$ $k_\theta = 5.388 \text{ eV/rad}^2, \theta_o = 109.5^\circ$



Dihedral [66]  Ryckaert–Bellemans  $E_D = \sum_{i=0}^5 a_i \cos^i \phi$	C-C-C-C  S-C-C-C  (same for  both)	$a_0 = 0.09617 \text{ eV},$  $a_1 = -0.125988 \text{ eV},$  $a_2 = -0.13598 \text{ eV},$  $a_3 = 0.0317 \text{ eV},$  $a_4 = 0.27196 \text{ eV},$  $a_5 = 0.32642 \text{ eV}$
Lennard-Jones [66] with  Lorentz–Berthelot mixing rules  $E_{LJ} = 4\epsilon_{ij} \left[ \left( \frac{\sigma_{ij}}{r_{ij}} \right)^{12} - \left( \frac{\sigma_{ij}}{r_{ij}} \right)^6 \right],$  where $i$ and $j$ refer to different atom types.	Au  CH <sub>3</sub>  CH <sub>2</sub>  S (with CH <sub>3</sub> and CH <sub>2</sub> )  S (with other S)	$\epsilon = 0.00169 \text{ eV}, \sigma = 2.935 \text{ \AA}$  $\epsilon = 0.00759 \text{ eV}, \sigma = 3.905 \text{ \AA}$  $\epsilon = 0.00512 \text{ eV}, \sigma = 3.905 \text{ \AA}$  $\epsilon = 0.01086 \text{ eV}, \sigma = 3.55 \text{ \AA}$  $\epsilon = 0.01724 \text{ eV}, \sigma = 4.25 \text{ \AA}$
Morse [66]  $E_{\text{morse}} = D_e \left[ \left( 1 - e^{-a(r-r_m)} \right)^2 - 1 \right]$	Au-S	$D_e = 0.38 \text{ eV}$  $a = 1.47 \text{ \AA}^{-1}$  $r_m = 2.65 \text{ \AA}$
EAM potentials [67]	Au-Au	

## II Gold Thermal Conductivity from Molecular Dynamics

The gold bulk thermal conductivity was predicted using the NEMD technique by my co-author Shubhaditya Majumdar. A block of gold with dimensions 26 x 25 x 174 Å<sup>3</sup> (corresponding to 6750 atoms) was used for the simulations. Periodic boundary conditions were imposed in the  $x$ - and  $y$ -directions. Fixed boundary conditions were imposed in the  $z$ -direction, which is the [111] direction for the FCC gold crystal structure and the direction for simulating the heat flow. The two layers adjacent to each fixed boundary were used as the heat source and heat sink. The interatomic gold potential used is referenced in Table B1. The system was first relaxed in the canonical ensemble at a temperature of 300 K for 1.5 ns. After this equilibration, the NEMD algorithm was started in the microcanonical ensemble with a heat flow of 0.0001 eV/fs. The temperature of the gold atoms was collected after an initialization period of 2.5 ns for a period of 7 ns. This time period was determined to be adequate for reaching steady state. The gold atoms were divided into 22 temperature regions (each region consisting of 3 layers of gold with 270 atoms). The slope of the temperature profile was calculated and used in the Fourier law to predict the gold bulk thermal conductivity. Table B2 gives the predicted values with respect to the mass,  $M$ , of the gold atoms, which was varied for use in the core mass series. We note that, as expected, the thermal conductivity scales according to  $\frac{1}{\sqrt{M}}$  [138].

**Table B2 Thermal conductivity of bulk gold with different mass multiples from molecular dynamics.**

$M/M_{Au}$	$k$ (W/m <sup>2</sup> -K)
0.01	17.4
0.05	7.86
0.3	3.08
1	1.84
2	1.27
4	0.94
8	0.67
16	0.47

### III Dodecanethiol Solid Thermal Conductivity from Molecular Dynamics

The thermal conductivity of a dodecanethiol solid is obtained using the NEMD technique in LAMMPS and the appropriate potentials as defined in Table B1. A block of randomly arranged dodecanethiol ligands (23933 atoms using the united atom approach) was first thermalized at a temperature of 300 K for 1 ns using velocity rescaling and equilibrated for a further 1 ns under the microcanonical ensemble with periodic boundary conditions. This block of ligands was then subjected to an isothermal-isobaric ensemble at an average temperature of 300 K and pressure of 0 Pa for 1 ns to obtain an equilibrium liquid. This resulting liquid has a density of 0.85 g/cm<sup>3</sup>, which agrees well with the experimental value of 0.84 g/cm<sup>3</sup> [139]. To obtain a

well-ordered solid near to room temperature, the liquid is first cooled at a rate of 1 K/ns to an average system temperature of 150 K before reheating and thermalizing to 300 K under the canonical ensemble for 1 ns followed by microcanonical ensemble for another 1 ns. The NEMD method was implemented at this temperature by fixing the two ends of the solid and dividing the solid into five regions, each of thickness 3 nm. Two of these regions were used to source and sink heat (0.08 eV/fs) through the remaining regions to achieve a target  $\Delta T$  of approximately 10 % of the average temperature. The steady state temperature profile was obtained by averaging blocks for 1 ns for a total duration of 10 ns and was used in the Fourier's law to obtain the ligand thermal conductivity. The ligand solid thermal conductivity at an average temperature of 300 K is  $0.15 \pm 0.01$  W/m-K.

## IV Molecular Dynamics Prediction of SAM Interfacial Thermal Conductance

The  $h_{SAM/gold}$  value was predicted by implementing NEMD on a gold-SAM-gold junction (Figure B1) by my co-author Shubhaditya Majumdar. To setup the system, decanedithiol ( $C_{10}H_{21}SH$ ) molecules were first placed on the (111) face of a gold block having dimensions of  $25 \times 24 \times 60 \text{ \AA}^3$  (2160 atoms). The alkanethiol SAMs were populated on the gold surface with a coverage density of  $21.6 \text{ \AA}^2$  per molecule and placed close to the surface FCC sites in the experimentally observed  $(\sqrt{3} \times \sqrt{3})R30^\circ$  configuration [104]. The potentials used are found in Table B1. This system was first equilibrated in the canonical ensemble for 1.5 ns. After this equilibration, a second gold

block (identical in dimensions to the first gold block) was placed on the other side of the SAM. This entire junction was then equilibrated for a further 1.5 ns. After this, a heat flow of 0.0001 eV/fs was added/removed for the heat source/sink (consisting of 180 atoms each) located next to the fixed ends (90 atoms each) of either gold block. Steady-state temperature data was collected for all the atoms after 2.5 ns for a period of 20 ns. The temperature gradient in each of the two gold blocks was obtained by fitting a line through eight successive temperature points - each the average temperature of three layers of atoms (270 atoms). Since a strong non-linearity in the temperature profile could be seen at the edge of a SAM/gold interface, the temperature difference was determined at the point where the profile in each gold block became linear. On average, this location was three to five layers of gold atoms away from the physical SAM/gold interface. The number of temperature points considered in the fit was varied from five to seven. Using more points captures the non-linear sections of the temperature profile near the gold-SAM interface. The interfacial thermal conductance of gold/SAM/gold was predicted by dividing the imposed heat flow by the average of the three temperature differences. The predicted value for the gold/SAM/gold junction is  $110 \pm 10 \text{ MW/m}^2\text{-K}$ . By assuming a negligible thermal resistance contribution from the molecules and that the individual interfacial thermal conductances of the two interfaces are non-interacting and in series, a single SAM/gold interface will have an interfacial thermal conductance value of  $220 \pm 20 \text{ MW/m}^2\text{-K}$ . Although this value is obtained using decanedithiol instead of dodecanedithiol molecules, the SAM interfacial thermal conductance has been found to be invariant with the molecule length [27,66,137].

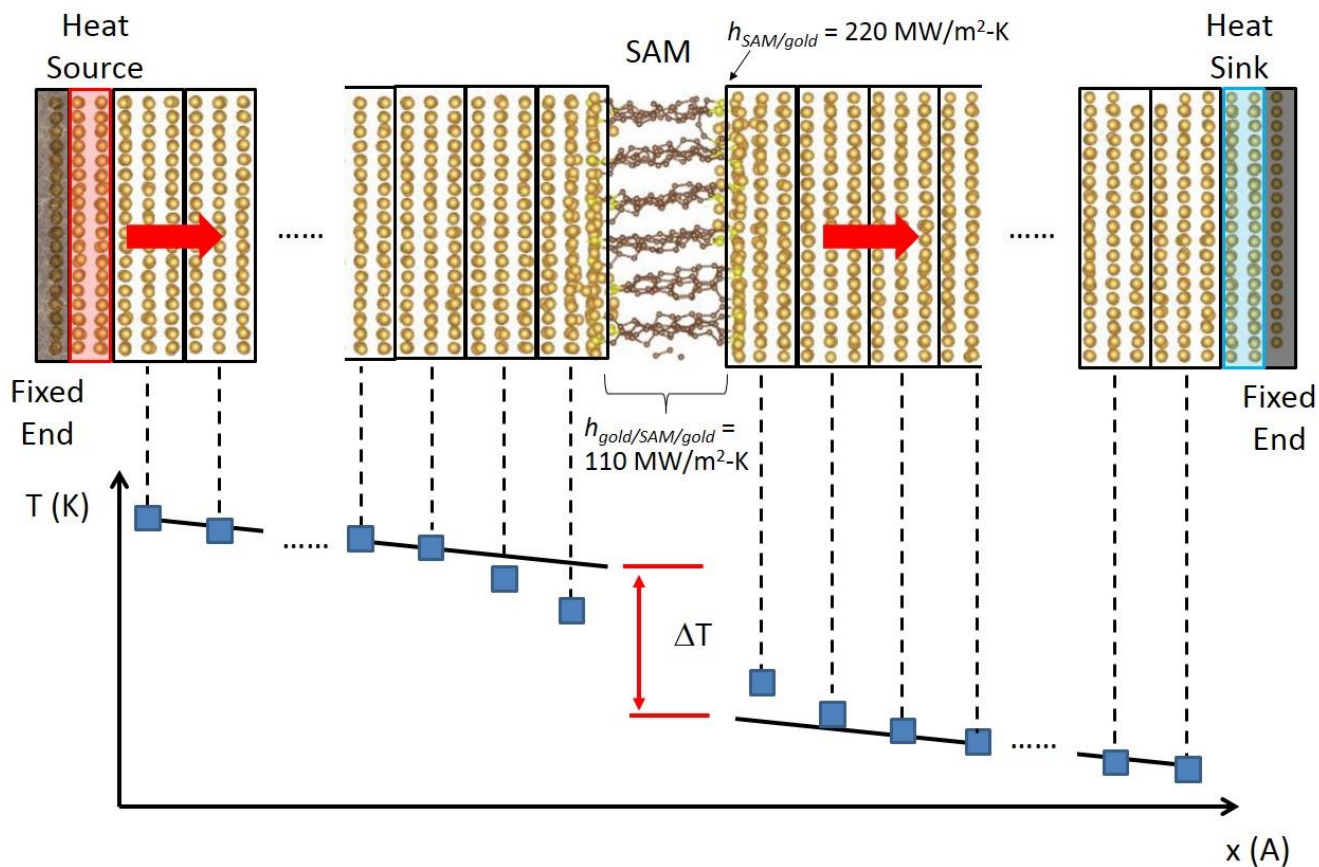


**Figure B1 SAM junction used for predicting the interfacial thermal conductance.** A representative temperature profile and the fits are shown below.

## V Uncertainty Analysis

In Figure 3.3, the error bar comes from standard deviation of repeated measurements of the core diameters. In Figures 3.4 and 3.5, the error bar on individual data point is the standard deviation from the five consecutive average of blocks of 1 ns simulation after steady state was reached. In Figure 3.4a, the uncertainty in  $h_{SAM/gold}$  is twice the standard deviation obtained from the thermal conductance prediction of the gold/SAM/gold junction.

The uncertainty for predictions made using equation 3.3 comes purely from the uncertainty of  $h_{SAM/gold}$ . In Figure 3.4b, the uncertainty associated for values calculated from equation 3.2 comes from the uncertainties in three of the individual inputs (i.e.,  $k_m$ ,  $k_p$ , and  $h$ ), which are combined using a root-sum of difference-square method [61].

## **Appendix C**

### **I Steady-state temperature rise in LUMCs**

### **II DFT calculation of heat capacity**

#### **I Steady-state temperature rise in LUMCs**

The power input to the FDTR technique was optimized with the signal-to-noise ratio throughout the scanned frequencies from 50 kHz to 5 MHz. In this frequency range, the thermal penetration depth is between 1.5  $\mu\text{m}$  to 70 nm, giving sufficient sensitivity to the LUMCs which are typically 100  $\mu\text{m}$  thick. The combined power absorbed at the surface of the gold coated LUMCs (gold thickness 60 – 100 nm) is about 1 mW, a value separately determined using a power meter. With this measured absorbed power, the analytical solution to the heat diffusion equation [24] used for fitting the FDTR data gives a steady-state temperature rise of approximately 40 – 55 K depending on the LUMCs thermal conductivity.

#### **II DFT calculation of heat capacity**

To get the full heat capacity value of a solid using DFT, the calculated heat capacity value is tested for convergence with respect to the number of frequencies needed throughout the full Brillouin zone. Due to the large number of atoms in each molecular



crystal (e.g., more than 100 atoms) and the lack of suitable computational facility, only gamma point frequencies are calculated. I started with the Quantum Espresso software to calculate the vibrational spectra of these molecules. However, several issues were encountered. First, the package for calculating vibrational spectrum (i.e., ph.x and phcg.x) can only accept certain type of pseudopotential implementations [e.g. Local-density approximations (LDA)]. In these molecular crystals, the Perdew–Burke–Ernzerhof (PBE) parametrized GGA will be more suitable due to the discreteness of these non-metallic crystals. Second, calculations are slow (when compared to VASP) but it has a desirable built-in capability of restarting vibrational calculation if a calculation is stopped before completion (e.g., reached the stipulated time-limit set for each running job). The switch to VASP as VASP is generally faster and allows the use of PBE-GGA pseudopotentials. The downside, however, is that VASP does not restart vibrational jobs if they are terminated prematurely.

The gamma point vibrational calculation is performed on an isolated superatom placed in a simulation cell surrounded with vacuum space. A five angstrom of vacuum space surrounding the superatom is found to be sufficient for the calculated total energy per atom to converge within 2 meV with successive larger simulation cells. The minimum planewave energy cutoff and size of the Monkhorst-Pack electronic k-mesh needed for calculations to converge to 2 meV are tabulated below (for VASP calculation only). The isolated superatom was relaxed before the vibrational calculation. The relaxation is stopped when the forces on each ion are converged to less than 0.1 meV/Å. The vibrational calculation is performed using the density functional perturbation theory (DFPT) implemented in VASP (i.e., ibrion = 8). For the case of C<sub>60</sub>, the same set of

vibrational calculation was done using a relaxed FCC structure with dispersion forces active between the different C<sub>60</sub> cages (i.e., DFT+D implementation).

**Table C1 The convergent parameters used in the DFT calculations.**

<b>LUMCs</b>	<b>Number of Atoms</b>	<b>Energy Cutoff (eV)</b>	<b>Electronic k-mesh</b>
C <sub>60</sub>	60	500	1x1x1
C <sub>70</sub>	70	500	1x1x1
CoS	146	450	1x1x1
CoSe	146	450	1x1x1
CoTe	146	450	1x1x1

I have also performed preliminary spin-polarised calculations on CoTe LUMC but these calculations did not indicate that the material is ferromagnetic/anti-ferromagnetic. Hence, the less expensive non-spin polarized calculations were subsequently used for CoS, CoSe, and CoTe.

## **Appendix D**

### **I Calibration**

### **II Error analysis**

### **III Software for Performing Steady State Measurements**

#### **I Calibration**

Calibration of the steady-state measurement setup was done using two different samples – epoxy (Stycast 2850FT–catalyst 9) and Pyrex (0.45 mm thick, similar to our sample). The epoxy was mixed, applied, and cured between the top and bottom parts of the jig for more than 24 hours as according to the manufacturer recommendation. The measured thermal conductivity using the setup gives a value of  $1.23 \pm 0.18$  W/m-K at 300 K which agrees with the value published in the manufacturer datasheet (*i.e.*, 1.25 W/m-K).

A Pyrex slab with a cross-sectional area of  $6 \times 6$  mm<sup>2</sup> was epoxied to the setup with Stycast 2850FT. Its temperature-dependent thermal conductivity was measured from 215 to 300 K. The measured values and trend, shown in Figure D1, agree with published results [140].

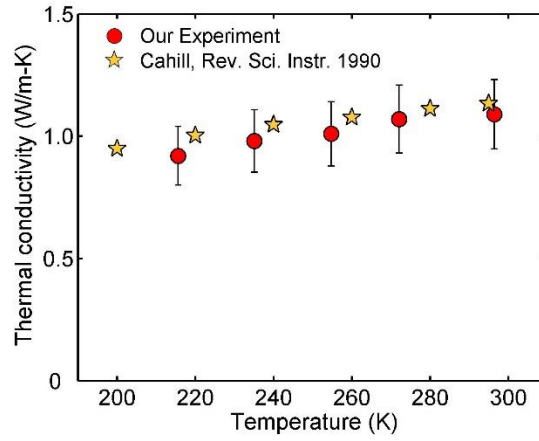


**Figure D1 Temperature-dependent thermal conductivity of Pyrex.**

## II Error analysis

Major sources of uncertainty are i) thickness of sample ( $\pm 10\%$ ) ii) thickness ( $\pm 10\%$ ) and thermal conductivity ( $\pm 20\%$ ) of epoxy used to attach the sample to the setup, iii) dimensions of the jig ( $\pm 10\%$ ). The overall uncertainty in the measured thermal conductivity indicated in Figure 5.3 was calculated based on the root-sum-square method [61].

## III Software for Performing Steady State Measurements

A control and acquisition software was written in matlab to communicate with the temperature controller (Oxford ITC 503S) to control the temperature of the setup in a cryostat, multimeter (Keithley 2700) to read the voltage across each platinum RTD, and current sourcemeter (Keithley 6221) to change the heating current. The matlab

program consists of the following files

1. steadyState.fig is the graphical user interface (GUI)
2. steadyState.m is the matlab code behind the GUI
3. findobj.m is a matlab-generated file when a GUI is created

The most current version of this program is under the folder “Control\_v5”. Running the program from steadyState.m.

The GUI with four visible panels and one hidden panel is shown in Figure D2.

The hidden panel appears after the option of “what do you want to do” is chosen.

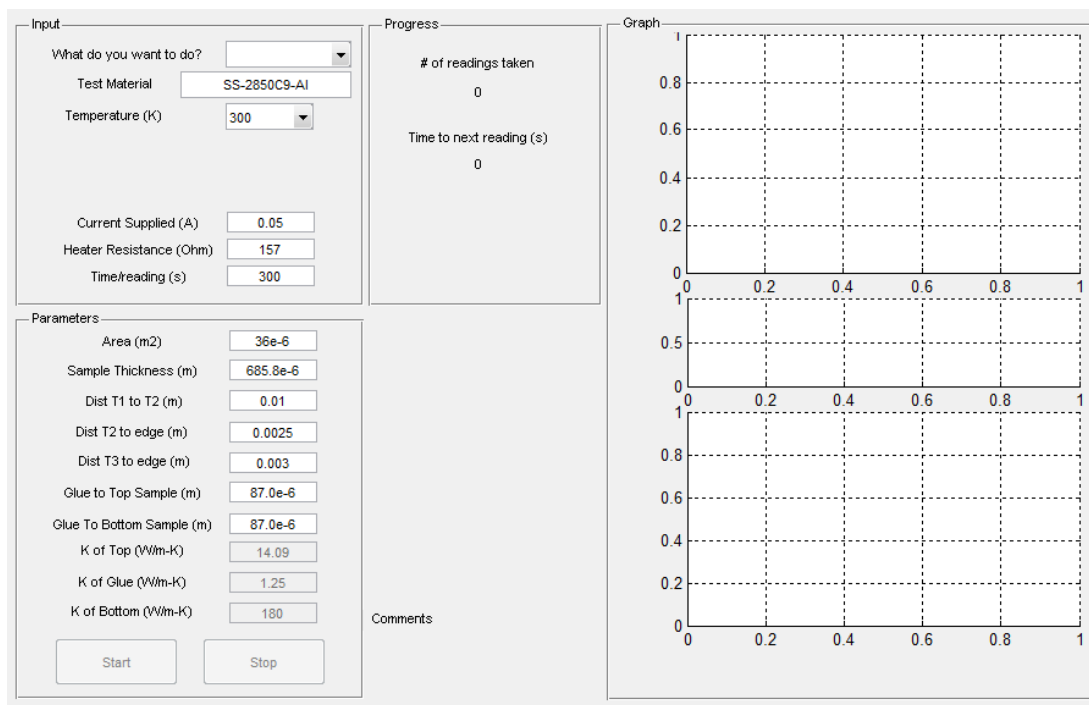


**Figure D2** GUI for controlling instruments and displaying the readings.

As there is already data available, it is easier to explain and familiarize with the program by looking with the current dataset. The following steps are used to review the data.

## Review the data

1. Select “Review Data” in “What do you want to do?” listbox.

The screenshot displays a software interface with three main sections: Input, Progress, and Graph.

**Input Section:**

- What do you want to do?:** A dropdown menu with 'Run Expt' and 'Review Data' options. 'Review Data' is currently selected.
- Test Material:** A text input field.
- Temperature (K):** A text input field.
- Current Supplied (A):** A text input field with the value '0.05'.
- Heater Resistance (Ohm):** A text input field with the value '157'.
- Time/reading (s):** A text input field with the value '300'.

**Parameters Section:**

- Area (m2):** 36e-6
- Sample Thickness (m):** 685.8e-6
- Dist T1 to T2 (m):** 0.01
- Dist T2 to edge (m):** 0.0025
- Dist T3 to edge (m):** 0.003
- Glue to Top Sample (m):** 87.0e-6
- Glue To Bottom Sample (m):** 87.0e-6
- K of Top (W/m-K):** 14.09
- K of Glue (W/m-K):** 1.25
- K of Bottom (W/m-K):** 180

**Progress Section:**

- # of readings taken:** 0
- Time to next reading (s):** 0

**Graph Section:**

Three empty coordinate systems are shown, each with x and y axes ranging from 0 to 1.0. The top graph has a y-axis from 0 to 1.0. The middle graph has a y-axis from 0 to 1.0. The bottom graph has a y-axis from 0 to 1.0.

**Buttons:** 'Start' and 'Stop' buttons are located at the bottom left.

**Comments:** A text area for user comments is located at the bottom right.

**Figure D3** GUI with options for “What to do you want to do” shown.

2. A dialog box will pop up to select the dataset to review by pressing on the “Start” button.

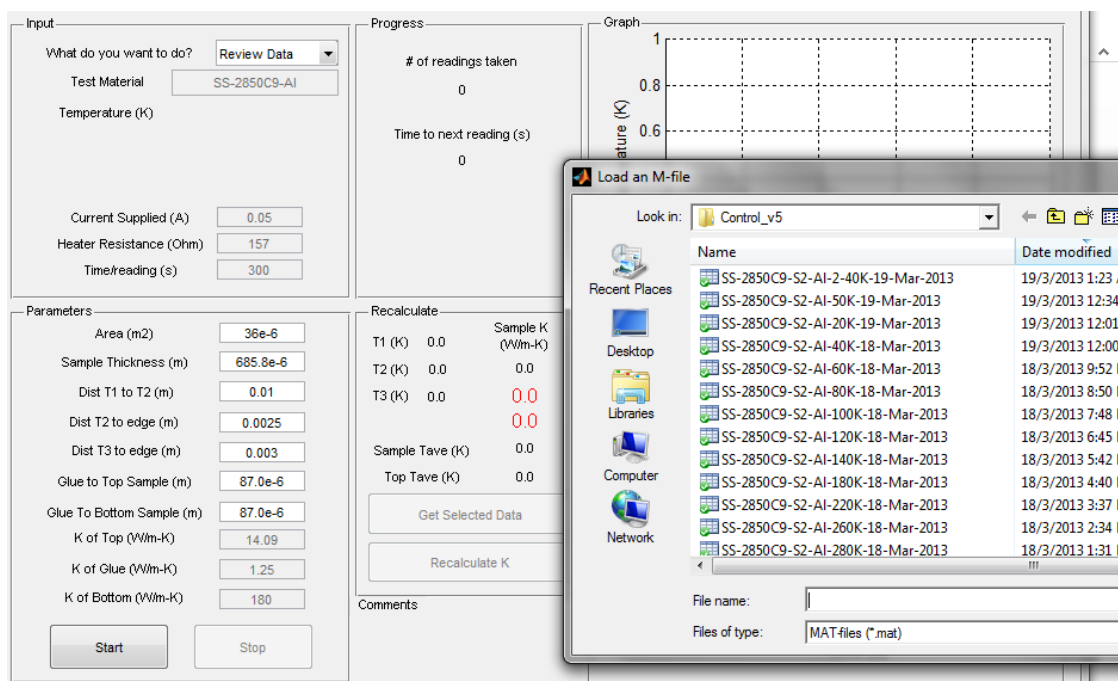


**Figure D4** Select the dataset for reviewing.

3. After the dataset is selected, the appropriate text-fields (graphs) will be populated based on the data input (recorded) during the experiments. The hidden panel “Recalculate” will appear.

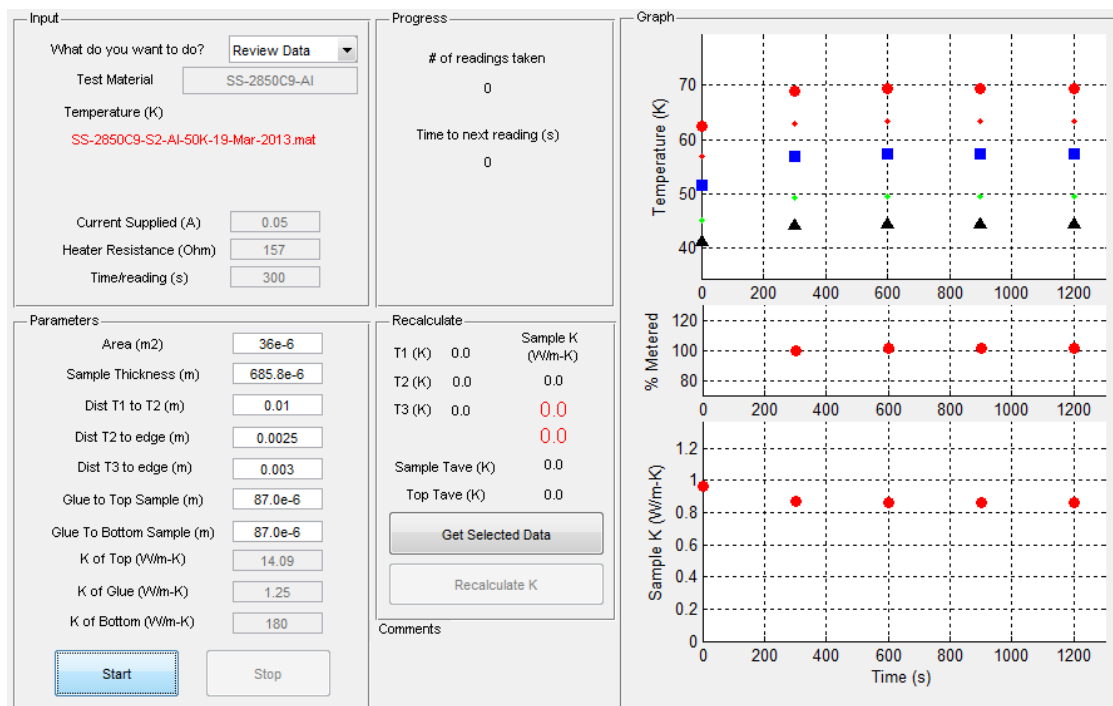


**Figure D5** Textboxes, labels, and graphs are populated with data.

4. Selecting a data-point on the graph by clicking on that point and then clicking on the “Get Selected Data” button in the “Recalculate” panel will populate the panel.



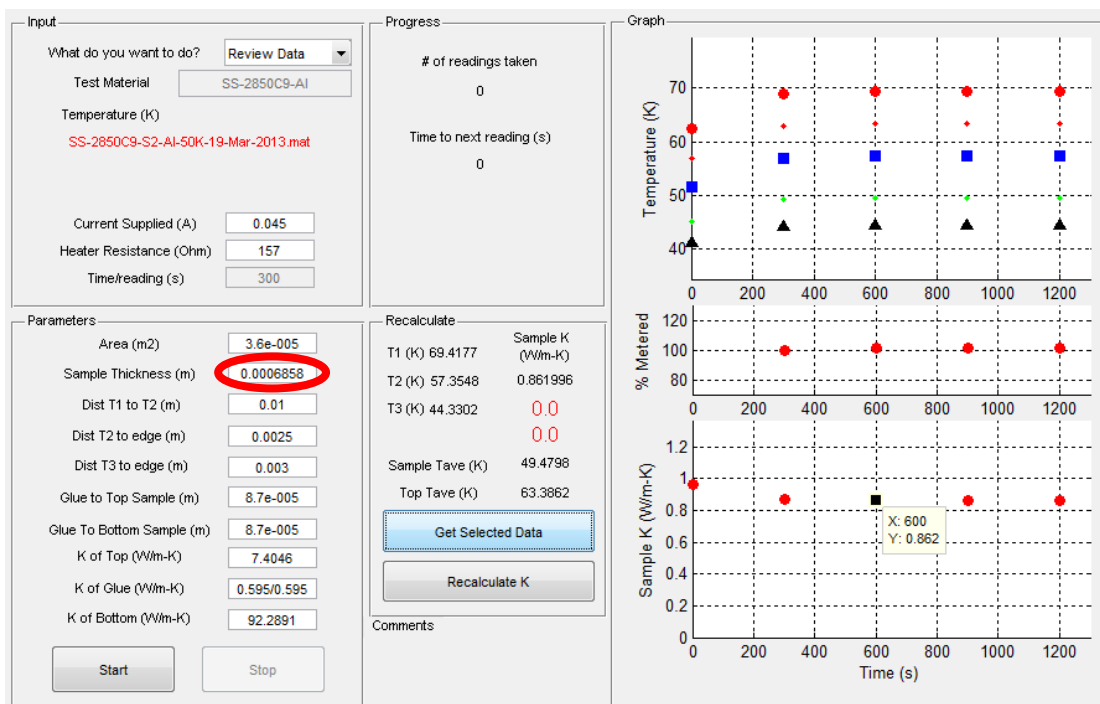


**Figure D6** The relevant temperatures and  $k$  are populated after clicking on the graph and “Get Selected Data” button.

5. Changing the values in the textboxes and clicking the “Recalculate K” button will change the displayed thermal conductivity ( $k$ ). The modified values in the textboxes will not, however, be saved.

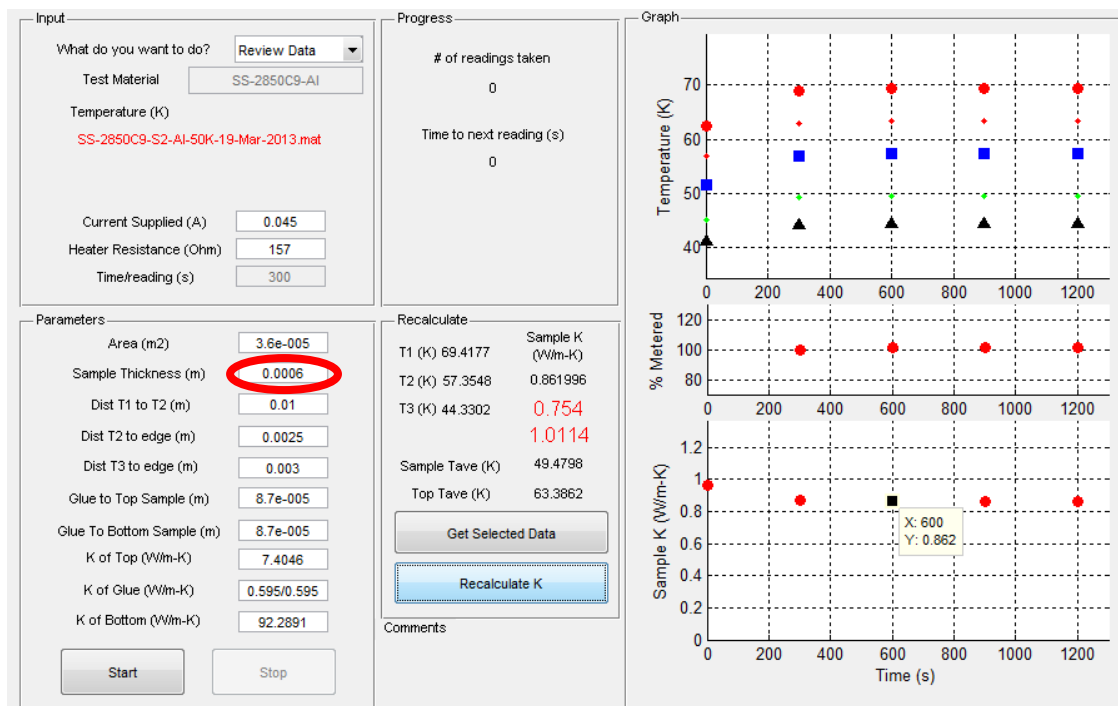


**Figure D7** The  $k$  is recalculated based on new inputs to the textboxes. The new input in this figure is in the red circle (compare with Figure D6).

6. Changing the values in the textboxes and clicking the “Recalculate K” button will change the displayed thermal conductivity. The modified values in the textboxed will not, however, be saved.

## Run the experiment

1. Select the “Run Expt” in the “What do you want to do?” listbox. Make the necessary changes to the nominal values in the textboxes that are set in the steadyState.fig. This setup is applicable only for a four-point measurement of a sample sandwiched between two jigs by adhesives.

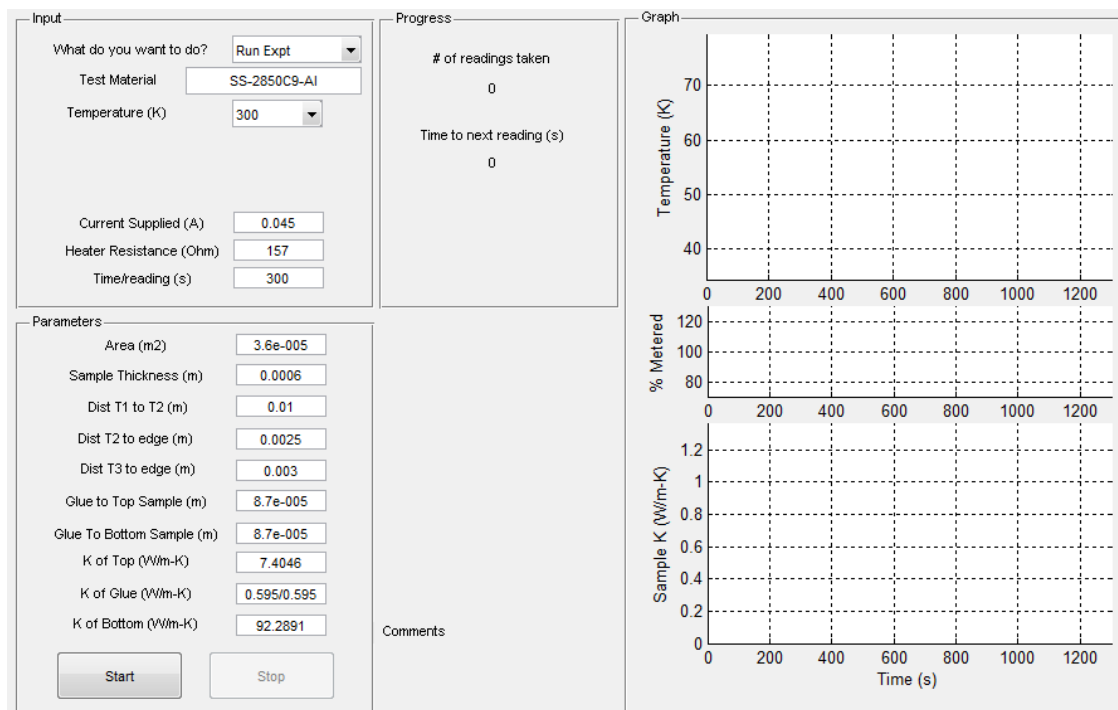


**Figure D8** The “Run Expt” option is selected. The nominal values in the textboxes are set in the steadyState.m.

2. Pressing the “Start” button will pop up the file dialog box with a pre-generated filename based the input, date, and temperature selected from the listbox. Press “Save” and the experiment will start. Please ensure that all the equipments are connected and switched on.

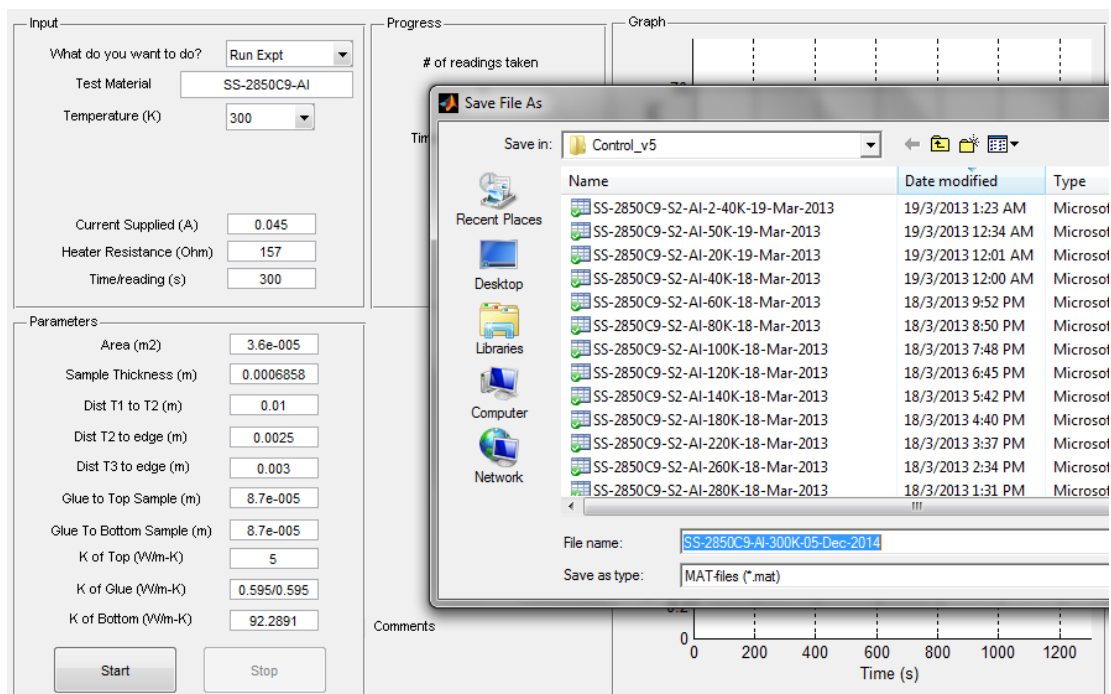


**Figure D9** Saving the filename will start the experiment.

The subroutines in the steadyState.m are commented in each routines for reprogramming needs.

## References

- [1] Claridge, S. A., Castleman, A. W., Khanna, S. N., Murray, C. B., Sen, A., and Weiss, P. S., 2009, "Cluster-assembled materials.," ACS Nano, **3**(2), pp. 244–55.
- [2] Talapin, D. V, Lee, J.-S., Kovalenko, M. V, and Shevchenko, E. V, 2010, "Prospects of colloidal nanocrystals for electronic and optoelectronic applications.," Chem. Rev., **110**(1), pp. 389–458.
- [3] Talapin, D. V, 2008, "LEGO Materials.," ACS Nano, **2**(6), pp. 1097–100.
- [4] Roy, X., Lee, C.-H., Crowther, A. C., Schenck, C. L., Besara, T., Lalancette, R. A., Siegrist, T., Stephens, P. W., Brus, L. E., Kim, P., Steigerwald, M. L., and Nuckolls, C., 2013, "Nanoscale atoms in solid-state chemistry.," Science, **341**(6142), pp. 157–60.
- [5] Murray, C. B., Kagan, C. R., and Bawendi, M. G., 1995, "Self-Organization of CdSe Nanocrystallites into Three-Dimensional Quantum Dot Superlattices.," Science, **270**(5240), pp. 1335–1338.
- [6] Lin, X. M., Jaeger, H. M., Sorensen, C. M., and Klabunde, K. J., 2001, "Formation of Long-Range-Ordered Nanocrystal Superlattices on Silicon Nitride Substrates.," J. Phys. Chem. B, **105**(17), pp. 3353–3357.
- [7] Talapin, D. V, and Murray, C. B., 2005, "PbSe nanocrystal solids for n- and p-channel thin film field-effect transistors.," Science, **310**(5745), pp. 86–89.
- [8] Sun, S., and Murray, C. B., 1999, "Synthesis of monodisperse cobalt nanocrystals and their assembly into magnetic superlattices.," J. Appl. Phys., **85**(8), p. 4325.
- [9] Colvin, V. L., Schlamp, M. C., and Alivisatos, A. P., 1994, "Light-emitting diodes made from cadmium selenide nanocrystals and a semiconducting polymer.," Nature, **370**(6488), pp. 354–357.
- [10] McDonald, S. A., Konstantatos, G., Zhang, S., Cyr, P. W., Klem, E. J. D., Levina, L., and Sargent, E. H., 2005, "Solution-processed PbS quantum dot infrared photodetectors and photovoltaics.," Nat. Mater., **4**(2), pp. 138–42.

- [11] Leatherdale, C., Kagan, C., Morgan, N., Empedocles, S., Kastner, M., and Bawendi, M., 2000, "Photoconductivity in CdSe quantum dot solids," *Phys. Rev. B*, **62**(4), pp. 2669–2680.
- [12] Tang, J., Kemp, K. W., Hoogland, S., Jeong, K. S., Liu, H., Levina, L., Furukawa, M., Wang, X., Debnath, R., Cha, D., Chou, K. W., Fischer, A., Amassian, A., Asbury, J. B., and Sargent, E. H., 2011, "Colloidal-quantum-dot photovoltaics using atomic-ligand passivation," *Nat. Mater.*, **10**(10), pp. 765–771.
- [13] Gur, I., Fromer, N. A., Geier, M. L., and Alivisatos, A. P., 2005, "Air-stable all-inorganic nanocrystal solar cells processed from solution," *Science*, **310**(5747), pp. 462–465.
- [14] Ehrler, B., Walker, B. J., Böhm, M. L., Wilson, M. W. B., Vaynzof, Y., Friend, R. H., and Greenham, N. C., 2012, "In situ measurement of exciton energy in hybrid singlet-fission solar cells," *Nat. Commun.*, **3**(May), p. 1019.
- [15] Kovalenko, M. V, Spokoyny, B., Lee, J.-S., Scheele, M., Weber, A., Perera, S., Landry, D., and Talapin, D. V, 2010, "Semiconductor nanocrystals functionalized with antimony telluride zintl ions for nanostructured thermoelectrics," *J. Am. Chem. Soc.*, **132**(19), pp. 6686–95.
- [16] Wang, R. Y., Feser, J. P., Lee, J.-S., Talapin, D. V, Segalman, R., and Majumdar, A., 2008, "Enhanced thermopower in PbSe nanocrystal quantum dot superlattices," *Nano Lett.*, **8**(8), pp. 2283–8.
- [17] Ko, D.-K., and Murray, C. B., 2011, "Probing the Fermi energy level and the density of states distribution in PbTe nanocrystal (quantum dot) solids by temperature-dependent thermopower measurements," *ACS Nano*, **5**(6), pp. 4810–7.
- [18] Lin, X. M., Jaeger, H. M., Sorensen, C. M., and Klabunde, K. J., 2001, "Formation of Long-Range-Ordered Nanocrystal Superlattices on Silicon Nitride Substrates," *J. Phys. Chem. B*, **105**(17), pp. 3353–3357.
- [19] Han, N., Cuong, T. V., Han, M., Ryu, B. D., Chandramohan, S., Park, J. B., Kang, J. H., Park, Y.-J., Ko, K. B., Kim, H. Y., Kim, H. K., Ryu, J. H., Katharria, Y. S., Choi, C.-J., and Hong, C.-H., 2013, "Improved heat dissipation in gallium nitride light-emitting diodes with embedded graphene oxide pattern," *Nat. Commun.*, **4**, p. 1452.
- [20] Kuribara, K., Wang, H., Uchiyama, N., Fukuda, K., Yokota, T., Zschieschang, U., Jaye, C., Fischer, D., Klauk, H., Yamamoto, T., Takimiya, K., Ikeda, M., Kuwabara, H., Sekitani, T., Loo, Y.-L., and Someya, T., 2012, "Organic

transistors with high thermal stability for medical applications.,” *Nat. Commun.*, **3**, p. 723.

- [21] Porter, M. D., Bright, T. B., Allara, D. L., and Chidsey, C. E. D., 1987, “Spontaneously organized molecular assemblies. 4. Structural characterization of n-alkyl thiol monolayers on gold by optical ellipsometry, infrared spectroscopy, and electrochemistry,” *J. Am. Chem. Soc.*, **109**(12), pp. 3559–3568.
- [22] Love, J. C., Estroff, L. A., Kriebel, J. K., Nuzzo, R. G., and Whitesides, G. M., 2005, “Self-assembled monolayers of thiolates on metals as a form of nanotechnology.,” *Chem. Rev.*, **105**(4), pp. 1103–69.
- [23] Segal, D., Nitzan, A., and Hänggi, P., 2003, “Thermal conductance through molecular wires,” *J. Chem. Phys.*, **119**(13), p. 6840.
- [24] Cahill, D. G., 2004, “Analysis of heat flow in layered structures for time-domain thermoreflectance,” *Rev. Sci. Instrum.*, **75**(12), p. 5119.
- [25] Schmidt, A. J., Cheaito, R., and Chiesa, M., 2009, “A frequency-domain thermoreflectance method for the characterization of thermal properties,” *Rev. Sci. Instrum.*, **094901**, pp. 1–6.
- [26] Wang, Z., Carter, J. A., Lagutchev, A., Koh, Y. K., Seong, N.-H., Cahill, D. G., and Dlott, D. D., 2007, “Ultrafast flash thermal conductance of molecular chains.,” *Science*, **317**(5839), pp. 787–90.
- [27] Wang, R. Y., Segalman, R. A., and Majumdar, A., 2006, “Room temperature thermal conductance of alkanedithiol self-assembled monolayers,” *Appl. Phys. Lett.*, **89**(17), p. 173113.
- [28] Duda, J. C., Saltonstall, C. B., Norris, P. M., and Hopkins, P. E., 2011, “Assessment and prediction of thermal transport at solid-self-assembled monolayer junctions.,” *J. Chem. Phys.*, **134**(9), p. 094704.
- [29] Meier, T., Menges, F., Nirmalraj, P., Hölscher, H., Riel, H., and Gotsmann, B., 2014, “Length-Dependent Thermal Transport along Molecular Chains,” *Phys. Rev. Lett.*, **113**(6), p. 060801.
- [30] Losego, M. D., Grady, M. E., Sottos, N. R., Cahill, D. G., and Braun, P. V., 2012, “Effects of chemical bonding on heat transport across interfaces,” *Nat. Mater.*, **11**(6), pp. 502–506.

- [31] Hu, L., Zhang, L., Hu, M., Wang, J.-S., Li, B., and Keblinski, P., 2010, “Phonon interference at self-assembled monolayer interfaces: Molecular dynamics simulations,” *Phys. Rev. B*, **81**(235427), pp. 1–5.
- [32] O’Brien, P. J., Shenogin, S., Liu, J., Chow, P. K., Laurencin, D., Mutin, P. H., Yamaguchi, M., Keblinski, P., and Ramanath, G., 2012, “Bonding-induced thermal conductance enhancement at inorganic heterointerfaces using nanomolecular monolayers,” *Nat. Mater.*, **12**(2), pp. 118–22.
- [33] Weaver, J. H., and Poirier, D. M., 1994, “Solid State Properties of Fullerenes and Fullerene-Based Materials,” *Solid State Physics*, H. Ehrenreich, and F. Spaepen, eds., Academic Press, Boston, pp. 1–108.
- [34] Haddon, R. C., 1992, “Electronic structure, conductivity and superconductivity of alkali metal doped (C<sub>60</sub>),” *Acc. Chem. Res.*, **25**(3), pp. 127–133.
- [35] Lieber, C. M., and Chen, C.-C., 1994, “Preparation of Fullerenes and Fullerene-Based Materials,” *Solid State Physics*, H. Ehrenreich, and F. Spaepen, eds., Academic Press, Boston, pp. 109–149.
- [36] Qian, M., Ong, S., Khanna, S., and Knickelbein, M., 2007, “Magnetic endohedral metallofullerenes with floppy interiors,” *Phys. Rev. B*, **75**(10), p. 104424.
- [37] Rosseinsky, M. J., 1998, “Recent Developments in the Chemistry and Physics of Metal Fullerenes,” *Chem. Mater.*, **10**(10), pp. 2665–2685.
- [38] Rosseinsky, M., Ramirez, A., Glarum, S., Murphy, D., Haddon, R., Hebard, A., Palstra, T., Kortan, A., Zahurak, S., and Makhija, A., 1991, “Superconductivity at 28 K in Rb<sub>x</sub>C<sub>60</sub>,” *Phys. Rev. Lett.*, **66**(21), pp. 2830–2832.
- [39] Ganin, A. Y., Takabayashi, Y., Khimyak, Y. Z., Margadonna, S., Tamai, A., Rosseinsky, M. J., and Prassides, K., 2008, “Bulk superconductivity at 38 K in a molecular system,” *Nat. Mater.*, **7**(5), pp. 367–71.
- [40] Hebard, A. F., Rosseinsky, M. J., Haddon, R. C., Murphy, D. W., Glarum, S. H., Palstra, T. T. M., Ramirez, A. P., and Kortan, A. R., 1991, “Superconductivity at 18 K in potassium-doped C<sub>60</sub>,” *Nature*, **350**(6319), pp. 600–601.
- [41] Segura, J. L., Martin, N., and Guldi, D. M., 2005, “Materials for organic solar cells: the C<sub>60</sub>/pi-conjugated oligomer approach,” *Chem. Soc. Rev.*, **34**(1), pp. 31–47.



- [42] Günes, S., Neugebauer, H., and Sariciftci, N. S., 2007, “Conjugated polymer-based organic solar cells,” *Chem. Rev.*, **107**(4), pp. 1324–38.
- [43] Yu, R., Tea, N., Salamon, M., Lorents, D., and Malhotra, R., 1992, “Thermal conductivity of single crystal C<sub>60</sub>,” *Phys. Rev. Lett.*, **68**(13), pp. 2050–2053.
- [44] Tea, N. H., Yu, R.-C., Salamon, M. B., Lorents, D. C., Malhotra, R., and Ruoff, R. S., 1993, “Thermal conductivity of C<sub>60</sub> and C<sub>70</sub> crystals,” *Appl. Phys. A*, **56**(3), pp. 219–225.
- [45] Kittel, C., 2005, *Introduction to Solid State Physics*, John Wiley & Sons, Ltd, Hoboken, NJ.
- [46] Neumann, D., Copley, J., Cappelletti, R., Kamitakahara, W., Lindstrom, R., Creegan, K., Cox, D., Romanow, W., Coustel, N., McCauley, J., Maliszewskyj, N., Fischer, J., and Smith, A., 1991, “Coherent quasielastic neutron scattering study of the rotational dynamics of C<sub>60</sub> in the orientationally disordered phase,” *Phys. Rev. Lett.*, **67**(27), pp. 3808–3811.
- [47] Tycko, R., Dabbagh, G., Fleming, R., Haddon, R., Makhija, A., and Zahurak, S., 1991, “Molecular dynamics and the phase transition in solid C<sub>60</sub>,” *Phys. Rev. Lett.*, **67**(14), pp. 1886–1889.
- [48] Olson, J. R., Topp, K. A., and Pohl, R. O., 1993, “Specific heat and thermal conductivity of solid fullerenes,” *Science*, **259**(5098), pp. 1145–8.
- [49] Batail, P., 2013, “Chemistry. Tuning molecular solids,” *Science*, **341**(6142), pp. 135–6.
- [50] Baudron, S. A., Batail, P., Coulon, C., Clérac, R., Canadell, E., Laukhin, V., Melzi, R., Wzietek, P., Jérôme, D., Auban-Senzier, P., and Ravy, S., 2005, “(EDT-TTF-CONH<sub>2</sub>)<sub>6</sub>[Re<sub>6</sub>Se<sub>8</sub>(CN)<sub>6</sub>], a metallic Kagome-type organic-inorganic hybrid compound: electronic instability, molecular motion, and charge localization,” *J. Am. Chem. Soc.*, **127**(33), pp. 11785–97.
- [51] Batail, P., Livage, C., Parkin, S. S. P., Coulon, C., Martin, J. D., and Canadell, E., 1991, “Antiperovskite Structure with Ternary Tetrathiafulvalenium Salts: Construction, Distortion, and Antiferromagnetic Ordering,” *Angew. Chem.*, **30**(11), pp. 1498–1500.
- [52] Duda, J. C., Hopkins, P. E., Shen, Y., and Gupta, M. C., 2013, “Exceptionally Low Thermal Conductivities of Films of the Fullerene Derivative PCBM,” *Phys. Rev. Lett.*, **110**(1), p. 015902.

- [53] Briseno, A. L., and Yang, P., 2009, “Combining chemical worlds,” *Nat. Mater.*, **8**(1), pp. 7–8.
- [54] Coe, S., Woo, W.-K., Bawendi, M., and Bulović, V., 2002, “Electroluminescence from single monolayers of nanocrystals in molecular organic devices,” *Nature*, **420**(6917), pp. 800–3.
- [55] Ong, W.-L., Rupich, S. M., Talapin, D. V., McGaughey, A. J. H., and Malen, J. A., 2013, “Surface chemistry mediates thermal transport in three-dimensional nanocrystal arrays,” *Nat. Mater.*, **12**(5), pp. 410–5.
- [56] Lee, J.-S., Kovalenko, M. V, Huang, J., Chung, D. S., and Talapin, D. V, 2011, “Band-like transport, high electron mobility and high photoconductivity in all-inorganic nanocrystal arrays,” *Nat. Nanotech.*, **6**(6), pp. 348–352.
- [57] Burda, C., Chen, X., Narayanan, R., and El-Sayed, M. A., 2005, “Chemistry and properties of nanocrystals of different shapes,” *Chem. Rev.*, **105**(4), pp. 1025–1102.
- [58] Losego, M. D., Grady, M. E., Sottos, N. R., Cahill, D. G., and Braun, P. V., 2012, “Effects of chemical bonding on heat transport across interfaces,” *Nat. Mater.*, **11**(6), pp. 502–6.
- [59] Pei, Y.-L., and Liu, Y., 2012, “Electrical and thermal transport properties of Pb-based chalcogenides: PbTe, PbSe, and PbS,” *J. Alloy. Compd*, **514**, pp. 40–44.
- [60] Harikrishnan, S., and Kalaiselvam, S., 2012, “Preparation and thermal characteristics of CuO–oleic acid nanofluids as a phase change material,” *Thermochim. Acta*, **533**, pp. 46–55.
- [61] Malen, J. A., Baheti, K., Tong, T., Zhao, Y., Hudgings, J. A., and Majumdar, A., 2011, “Optical Measurement of Thermal Conductivity Using Fiber Aligned Frequency Domain Thermoreflectance,” *J. Heat Transf.*, **133**(8), p. 081601.
- [62] Plimpton, S., 1995, “Fast Parallel Algorithms for Short-Range Molecular Dynamics,” *J. Comp. Phys.*, **117**(1), pp. 1–19.
- [63] Landry, E., Hussein, M., and McGaughey, A., 2008, “Complex superlattice unit cell designs for reduced thermal conductivity,” *Phys. Rev. B*, **77**(18), p. 184302.
- [64] Di Bucchianico, A., 2008, *Encyclopedia of Statistics in Quality and Reliability*, John Wiley & Sons, Ltd, Chichester, UK.
- [65] Hautman, J., and Klein, M. L., 1989, “Simulation of a monolayer of alkyl thiol chains,” *J. Chem. Phys.*, **91**(8), p. 4994.

- [66] Luo, T., and Lloyd, J. R., 2010, "Equilibrium Molecular Dynamics Study of Lattice Thermal Conductivity/Conductance of Au-SAM-Au Junctions," *J. Heat Transf.*, **132**(3), p. 032401.
- [67] Grochola, G., Russo, S. P., and Snook, I. K., 2005, "On fitting a gold embedded atom method potential using the force matching method," *J. Chem. Phys.*, **123**(20), p. 204719.
- [68] Lynn, J., Smith, H., and Nicklow, R., 1973, "Lattice Dynamics of Gold," *Phys. Rev. B*, **8**(8), pp. 3493–3499.
- [69] Turney, J., Landry, E., McGaughey, A., and Amon, C., 2009, "Predicting phonon properties and thermal conductivity from anharmonic lattice dynamics calculations and molecular dynamics simulations," *Phys. Rev. B*, **79**(6), pp. 1–12.
- [70] Gale, J. D., 1997, "GULP: A computer program for the symmetry-adapted simulation of solids," *J. Chem. Soc., Faraday Trans.*, **93**(4), pp. 629–637.
- [71] Höhne, G. W. H., Hemminger, W. F., and Flammersheim, H.-J., 2003, *Differential Scanning Calorimetry*, Springer, Berlin, Heidelberg.
- [72] Terrill, R. H., Postlethwaite, T. A., Chen, C., Poon, C.-D., Terzis, A., Chen, A., Hutchison, J. E., Clark, M. R., and Wignall, G., 1995, "Monolayers in Three Dimensions: NMR, SAXS, Thermal, and Electron Hopping Studies of Alkanethiol Stabilized Gold Clusters," *J. Am. Chem. Soc.*, **117**(50), pp. 12537–12548.
- [73] Wang, J., Carson, J. K., North, M. F., and Cleland, D. J., 2006, "A new approach to modelling the effective thermal conductivity of heterogeneous materials," *Int. J. Heat Mass Transf.*, **49**(17-18), pp. 3075–3083.
- [74] Hashin, Z., 1968, "Assessment of the Self Consistent Scheme Approximation: Conductivity of Particulate Composites," *J. Compos. Mater.*, **2**(3), pp. 284–300.
- [75] Minnich, A., and Chen, G., 2007, "Modified effective medium formulation for the thermal conductivity of nanocomposites," *Appl. Phys. Lett.*, **91**(7), p. 073105.
- [76] Baroncini, C., Filippo, P., Latini, G., and Pacetti, M., 1981, "Organic liquid thermal conductivity: A prediction method in the reduced temperature range 0.3 to 0.8," *Int. J. Thermophys.*, **2**(1), pp. 21–38.

- [77] Hasselman, D. P. H., and Johnson, L. F., 1987, "Effective Thermal Conductivity of Composites with Interfacial Thermal Barrier Resistance," *J. Compos. Mater.*, **21**(6), pp. 508–515.
- [78] Zebarjadi, M., Esfarjani, K., Dresselhaus, M. S., Ren, Z. F., and Chen, G., 2012, "Perspectives on thermoelectrics: from fundamentals to device applications," *Energy Environ. Sci.*, **5**(1), p. 5147.
- [79] Cline, C. F., Dunegan, H. L., and Henderson, G. W., 1967, "Elastic Constants of Hexagonal BeO, ZnS, and CdSe," *J. Appl. Phys.*, **38**(4), pp. 1944–1948.
- [80] Parkinson, D. H., and Quarrington, J. E., 1954, "The Molar Heats of Lead Sulphide, Selenide and Telluride in the Temperature Range 20 K to 260 K," *Proc. Phys. Soc. A*, **67**, pp. 569–579.
- [81] Kouvel, J., 1956, "Specific Heat of a Magnetite Crystal at Liquid Helium Temperatures," *Phys. Rev.*, **102**(6), pp. 1489–1490.
- [82] Hopkins, P. E., Norris, P. M., and Stevens, R. J., 2008, "Influence of Inelastic Scattering at Metal-Dielectric Interfaces," *J. Heat Transf.*, **130**(2), p. 022401.
- [83] Segal, D., and Nitzan, A., 2005, "Heat rectification in molecular junctions," *J. Chem. Phys.*, **122**(19), p. 194704.
- [84] Coe, S., Woo, W.-K., Bawendi, M., and Bulović, V., 2002, "Electroluminescence from single monolayers of nanocrystals in molecular organic devices," *Nature*, **420**(6917), pp. 800–3.
- [85] Safarov, M. M., and Zaripova, M. A., 1996, "Density dependence of heat conductivity of aqueous hydrazine solutions within wide ranges of temperature and pressure," *J. Engg Phys Thermophys*, **68**(3), pp. 390–394.
- [86] Ong, W., Majumdar, S., Malen, J. A., and McGaughey, A. J. H., 2014, "Coupling of Organic and Inorganic Vibrational States and Their Thermal Transport in Nanocrystal Arrays," *J. Phys. Chem. C*, **118**(14), pp. 7288–7295.
- [87] Wang, Z., Cahill, D. G., Carter, J. A., Koh, Y. K., Lagutchev, A., Seong, N.-H., and Dlott, D. D., 2008, "Ultrafast dynamics of heat flow across molecules," *Chem. Phys.*, **350**(1-3), pp. 31–44.
- [88] Ge, Z., Cahill, D., and Braun, P., 2006, "Thermal Conductance of Hydrophilic and Hydrophobic Interfaces," *Phys. Rev. Lett.*, **96**(18), p. 186101.

- [89] Luo, T., and Lloyd, J. R., 2010, “Non-equilibrium molecular dynamics study of thermal energy transport in Au–SAM–Au junctions,” *Int. J. Heat Mass Transf.*, **53**(1-3), pp. 1–11.
- [90] Zhang, Y., Barnes, G. L., Yan, T., and Hase, W. L., 2010, “Model non-equilibrium molecular dynamics simulations of heat transfer from a hot gold surface to an alkylthiolate self-assembled monolayer,” *Phys. Chem. Chem. Phys.*, **12**(17), pp. 4435–45.
- [91] Kaushik, A. P., and Clancy, P., 2013, “Solvent-driven symmetry of self-assembled nanocrystal superlattices--a computational study,” *J. Comp. Chem.*, **34**(7), pp. 523–32.
- [92] Ghorai, P. K., and Glotzer, S. C., 2007, “Molecular Dynamics Simulation Study of Self-Assembled Monolayers of Alkanethiol Surfactants on Spherical Gold Nanoparticles,” *J. Phys. Chem. C*, **111**(43), pp. 15857–15862.
- [93] Yang, A.-C., and Weng, C.-I., 2010, “Structural and Dynamic Properties of Water near Monolayer-Protected Gold Clusters with Various Alkanethiol Tail Groups,” *J. Phys. Chem. C*, **114**(19), pp. 8697–8709.
- [94] Lane, J. M. D., and Grest, G. S., 2010, “Spontaneous Asymmetry of Coated Spherical Nanoparticles in Solution and at Liquid-Vapor Interfaces,” *Phys. Rev. Lett.*, **104**(23), p. 235501.
- [95] Luedtke, W. D., and Landman, U., 1996, “Structure, Dynamics, and Thermodynamics of Passivated Gold Nanocrystallites and Their Assemblies,” *J. Phys. Chem.*, **100**(32), pp. 13323–13329.
- [96] Schapotschnikow, P., Pool, R., and Vlugt, T. J. H., 2008, “Molecular simulations of interacting nanocrystals,” *Nano Lett.*, **8**(9), pp. 2930–4.
- [97] Zanjani, M. B., and Lukes, J. R., 2013, “Size dependent elastic moduli of CdSe nanocrystal superlattices predicted from atomistic and coarse grained models,” *J. Chem. Phys.*, **139**(14), p. 144702.
- [98] Zanjani, M. B., and Lukes, J. R., 2014, “Phonon dispersion and thermal conductivity of nanocrystal superlattices using three-dimensional atomistic models,” *J. Appl. Phys.*, **115**(14), p. 143515.
- [99] Krüger, D., Fuchs, H., Rousseau, R., Marx, D., and Parrinello, M., 2001, “Interaction of short-chain alkane thiols and thiolates with small gold clusters: Adsorption structures and energetics,” *J. Chem. Phys.*, **115**(10), p. 4776.

- [100] Jadzinsky, P. D., Calero, G., Ackerson, C. J., Bushnell, D. A., and Kornberg, R. D., 2007, "Structure of a thiol monolayer-protected gold nanoparticle at 1.1 Å resolution," *Science*, **318**(5849), pp. 430–3.
- [101] Schelling, P. K., Phillpot, S. R., and Keblinski, P., 2002, "Comparison of atomic-level simulation methods for computing thermal conductivity," *Phys. Rev. B*, **65**(14), p. 144306.
- [102] Jiménez, A., Sarsa, A., Blázquez, M., and Pineda, T., 2010, "A Molecular Dynamics Study of the Surfactant Surface Density of Alkanethiol Self-Assembled Monolayers on Gold Nanoparticles as a Function of the Radius," *J. Phys. Chem. C*, **114**(49), pp. 21309–21314.
- [103] Mar, W., and Klein, M. L., 1994, "Molecular dynamics study of the self-assembled monolayer composed of S(CH<sub>2</sub>)<sub>14</sub>CH<sub>3</sub> molecules using an all-atoms model," *Langmuir*, **10**(1), pp. 188–196.
- [104] Strong, L., and Whitesides, G. M., 1988, "Structures of self-assembled monolayer films of organosulfur compounds adsorbed on gold single crystals: electron diffraction studies," *Langmuir*, **4**(3), pp. 546–558.
- [105] Hill, H. D., Millstone, J. E., Banholzer, M. J., and Mirkin, C. A., 2009, "The role radius of curvature plays in thiolated oligonucleotide loading on gold nanoparticles," *ACS Nano*, **3**(2), pp. 418–24.
- [106] Nan, C.-W., Birringer, R., Clarke, D. R., and Gleiter, H., 1997, "Effective thermal conductivity of particulate composites with interfacial thermal resistance," *J. Appl. Phys.*, **81**(10), p. 6692.
- [107] Henry, A., and Chen, G., 2009, "Anomalous heat conduction in polyethylene chains: Theory and molecular dynamics simulations," *Phys. Rev. B*, **79**, p. 144305.
- [108] Freeman, J., Morgan, G., and Cullen, C., 1987, "Thermal conductivity of a single polymer chain," *Phys. Rev. B*, **35**(14), pp. 7627–7635.
- [109] Losego, M. D., and Cahill, D. G., 2013, "Thermal transport: Breaking through barriers," *Nat. Mater.*, **12**(5), pp. 382–4.
- [110] Turney, J., Landry, E., McGaughey, A., and Amon, C., 2009, "Predicting phonon properties and thermal conductivity from anharmonic lattice dynamics calculations and molecular dynamics simulations," *Phys. Rev. B*, **79**(6), p. 064301.

- [111] Diky, V. V, and Kabo, G. J., 2000, “Thermodynamic properties of C 60 and C 70 fullerenes,” *Russ. Chem. Rev.*, **69**(2), pp. 95–104.
- [112] Chiritescu, C., Cahill, D. G., Nguyen, N., Johnson, D., Bodapati, A., Keblinski, P., and Zschack, P., 2007, “Ultralow thermal conductivity in disordered, layered WSe2 crystals,” *Science*, **315**(5810), pp. 351–3.
- [113] Jagannathan, A., Orbach, R., and Entin-Wohlman, O., 1989, “Thermal conductivity of amorphous materials above the plateau,” *Phys. Rev. B*, **39**(18), pp. 13465–13477.
- [114] Cahill, D., Watson, S., and Pohl, R., 1992, “Lower limit to the thermal conductivity of disordered crystals,” *Phys. Rev. B*, **46**(10), pp. 6131–6140.
- [115] Banerjee, A., Fauqué, B., Izawa, K., Miyake, A., Sheikin, I., Flouquet, J., Lenoir, B., and Behnia, K., 2008, “Transport anomalies across the quantum limit in semimetallic Bi<sub>0.96</sub>Sb<sub>0.04</sub>,” *Phys. Rev. B*, **78**(16), p. 161103.
- [116] Rabina, O., Lin, Y.-M., and Dresselhaus, M. S., 2001, “Anomalous high thermoelectric figure of merit in Bi<sub>[sub 1-x]</sub>Sb<sub>[sub x]</sub> nanowires by carrier pocket alignment,” *Appl. Phys. Lett.*, **79**(1), p. 81.
- [117] Lukas, K. C., Joshi, G., Modic, K., Ren, Z. F., and Opeil, C. P., 2012, “Thermoelectric properties of Ho-doped Bi<sub>0.88</sub>Sb<sub>0.12</sub>,” *J. Mater. Sci.*, **47**(15), pp. 5729–5734.
- [118] Lin, Y.-M., Cronin, S. B., Rabin, O., Ying, J. Y., and Dresselhaus, M. S., 2001, “Transport properties of Bi<sub>[sub 1-x]</sub>Sb<sub>[sub x]</sub> alloy nanowires synthesized by pressure injection,” *Appl. Phys. Lett.*, **79**(5), p. 677.
- [119] Zhang, H., Son, J. S., Jang, J., Lee, J.-S., Ong, W.-L., Malen, J. A., and Talapin, D. V, 2013, “Bi(1)-(x)Sb(x) alloy nanocrystals: colloidal synthesis, charge transport, and thermoelectric properties,” *ACS Nano*, **7**(11), pp. 10296–306.
- [120] Lenoir, B., Dauscher, A., Cassart, M., Ravich, Y. I., and Scherrer, H., 1998, “Effect of antimony content on the thermoelectric figure of merit of Bi<sub>1-x</sub>Sb<sub>x</sub> alloys,” *J. Phys. Chem. Solids*, **59**(1), pp. 129–134.
- [121] Poudel, B., Hao, Q., Ma, Y., Lan, Y., Minnich, A., Yu, B., Yan, X., Wang, D., Muto, A., Vashaee, D., Chen, X., Liu, J., Dresselhaus, M. S., Chen, G., and Ren, Z., 2008, “High-thermoelectric performance of nanostructured bismuth antimony telluride bulk alloys,” *Science*, **320**(5876), pp. 634–8.

- [122] Lenoir, B., Cassart, M., Michenaud, J.-P., Scherrer, H., and Scherrer, S., 1996, "Transport properties of Bi-RICH Bi-Sb alloys," *J. Phys. Chem. Solids*, **57**(1), pp. 89–99.
- [123] Ho, H., Sharma, A. A., Ong, W.-L., Malen, J. A., Bain, J. A., and Zhu, J.-G., 2013, "Experimental estimates of in-plane thermal conductivity in FePt-C granular thin film heat assisted magnetic recording media using a model layered system," *Appl. Phys. Lett.*, **103**(13), p. 131907.
- [124] Chia Tan, C., Shi, L., Zhao, R., Guo, Q., Li, Y., Yang, Y., Chong Chong, T., Malen, J. A., Ong, W.-L., Schlesinger, T. E., and Bain, J. A., 2013, "Compositionally matched nitrogen-doped Ge<sub>2</sub>Sb<sub>2</sub>Te<sub>5</sub>/Ge<sub>2</sub>Sb<sub>2</sub>Te<sub>5</sub> superlattice-like structures for phase change random access memory," *Appl. Phys. Lett.*, **103**(13), p. 133507.
- [125] Lai, S., 2003, "Current status of the phase change memory and its future," *IEEE Int. Electron Dev. Meeting*, IEEE, pp. 10.1.1–10.1.4.
- [126] Pirovano, A., Lacaita, A. L., Benvenuti, A., Pellizzer, F., and Bez, R., 2004, "Electronic Switching in Phase-Change Memories," *IEEE Trans. Electron Dev.*, **51**(3), pp. 452–459.
- [127] Simpson, R. E., Fons, P., Kolobov, a V, Fukaya, T., Krbal, M., Yagi, T., and Tominaga, J., 2011, "Interfacial phase-change memory.," *Nat. Nanotech.*, **6**(8), pp. 501–5.
- [128] Goodson, K. E., Flik, M. I., Su, L. T., and Antoniadis, D. A., 1994, "Prediction and Measurement of the Thermal Conductivity of Amorphous Dielectric Layers," *J. Heat Transf.*, **116**(2), p. 317.
- [129] Lee, S.-M., and Cahill, D. G., 1997, "Heat transport in thin dielectric films," *J. Appl. Phys.*, **81**(6), p. 2590.
- [130] Tan, C. C., Zhao, R., Shi, L., Chong, T. C., Bain, J. A., Schlesinger, T. E., Malen, J. A., and Ong, W. L., 2011, "Thermal conductivity measurements of nitrogen-doped Ge<sub>2</sub>Sb<sub>2</sub>Te<sub>5</sub>," *11th Ann. Non-Vol. Mem. Tech. Sym. Proc.*, IEEE, pp. 1–4.
- [131] Furukawa, G. T., Saba, W. G., and Reilly, M. L., 1968, Critical analysis of the heat-capacity data of the literature and evaluation of thermodynamic properties of copper, silver, and gold, from 0 to 300 K, U.S. Dept. of Commerce, National Bureau of Standards, Washington, D.C.
- [132] Desai, P. D., 1986, "Thermodynamic Properties of Iron and Silicon," *J. Physi. Chem. Ref. Data*, **15**(3), p. 967.



- [133] Babaei, H., Keblinski, P., and Khodadadi, J. M., 2013, "Thermal conductivity enhancement of paraffins by increasing the alignment of molecules through adding CNT/graphene," *Int. J. Heat Mass Transf.*, **58**(1-2), pp. 209–216.
- [134] Sung, I.-H., and Kim, D.-E., 2004, "Molecular dynamics simulation study of the nano-wear characteristics of alkanethiol self-assembled monolayers," *Appl. Phys. A*, **81**(1), pp. 109–114.
- [135] Mahaffy, R., Bhatia, R., and Garrison, B. J., 1997, "Diffusion of a Butanethiolate Molecule on a Au{111} Surface," *J. Phys. Chem. B*, **101**(5), pp. 771–773.
- [136] Allen, M. P., and Tildesley, D. J., 1987, *Computer Simulation of Liquids*, Clarendon Press, Oxford.
- [137] Duda, J. C., Saltonstall, C. B., Norris, P. M., and Hopkins, P. E., 2011, "Assessment and prediction of thermal transport at solid-self-assembled monolayer junctions.," *J. Chem. Phys.*, **134**(9), p. 094704.
- [138] McGaughey, a., Hussein, M., Landry, E., Kaviani, M., and Hulbert, G., 2006, "Phonon band structure and thermal transport correlation in a layered diatomic crystal," *Phys. Rev. B*, **74**(10), pp. 1–12.
- [139] Lide, D. R., and Milne, G. W. A., eds., 1994, *Handbook of Data on Organic Compounds*, CRC Press, Inc, Boca Raton ,FL.
- [140] Cahill, D. G., 1990, "Thermal conductivity measurement from 30 to 750 K: the 3 $\omega$  method," *Rev. Sci. Instr.*, **61**(2), p. 802.